Universidade do Minho
Escola de Engenharia

Alessandro Pucci

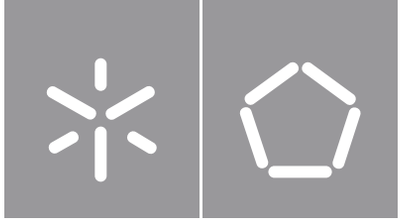
Bridge Network Collapse due to Floods

January 2024

Bridge Network Collapse due to Floods

Alessandro Pucci

UMinho | 2024



Universidade do Minho
Escola de Engenharia

Alessandro Pucci

Bridge Network Collapse due to Floods

Dotoral thesis
Civil engineering

Work performed under the supervision of
Professor José C. Matos
Professor Linda Giresini
Dr. Hélder S. Sousa

January 2024

Acknowledgements

First and above all, I would like to express my gratitude to my Supervisors, alphabetically ordered: Prof. Linda Giresini, Prof. José C. Matos and Dr. Hélder S. Sousa. Your efforts guiding me along the Ph.D. path have been inestimably precious. In addition, I would double-acknowledge each of them for specific reasons: Linda Giresini and Hélder S. Sousa for accepting me as student in first place, helping me improving my scientific writing skills, oral presentation and actively contributing to the development of the framework of this Thesis. Finally, I would like to thank José C. Matos because he gradually introduced me to acquiring also project management skills, by delivering to me more responsibilities and duties over the years. Thank you for believing in me and in my capabilities.

I would like to thank also those who contributed to my Ph.D. through mentoring; namely, Prof. Fabio Castelli, Prof. Mauro Sassu and Referatsleiter Dipl.-Ing. Ralph Holst. In addition, I would like to acknowledge the Director of the Doctoral Programme, Prof. Joaquim Barros, for his attention to the students' needs during the period I was part of the Student Committee. Then, I would address my gratitude also to the ISISE Institute and to Prof. Paulo B. Lourenço. Finally, I would like to acknowledge the members of ISISE that have been of great support, by organising social events before and after the Pandemic period. Then, I would like to acknowledge Reza, with whom I shared the membership of the Doctoral Programme's Student Committee and many adventures outside University. Then, I acknowledge also those friends that have been closely linked to me within this Ph.D. period:, Ali, Amin, Ana, Andrea, Behzad, Célia, Chonsy, Daniel E., Deborah, Marta, Nuno, Peter, Serena, Sofia, Sonja, Stefan K. and Stefan S. Then, I would like to thank the person without whom my life would just be painted black and white: my wife Consuelo.

Statement of Integrity

I hereby declare having conducted this academic work with integrity. I confirm that I have not used plagiarism or any form of undue use of information or falsification of results along the process leading to its elaboration.

I further declare that I have fully acknowledged the Code of Ethical Conduct of the University of Minho.

Financial Support

The Author acknowledges that, this work was partly financed by FCT / MCTES through national funds (PIDDAC) under the R&D Unit Institute for Sustainability and Innovation in Structural Engineering (ISISE), under reference UIDB/04029/2020, and under the Associate Laboratory Advanced Production and Intelligent Systems ARISE under reference LA/P/0112/2020.

This work is financed by national funds through FCT – Foundation for Science and Technology, under Grant agreement SFRH/BD/145478/2019 attributed to the Author.





Index

Acknowledgements ii

Statement of Integrity iii

Financial Support iv

Index v

Abstract ix

List of Figures xi

List of Tables xv

Glossary xvi

Abbreviation List xxiv

List of Equation Symbols xxvii

1. Introduction 1

1.1. Problem Identification 1

1.2. Motivation 3

1.2.1. Hydrologic and Hydraulic Overview 4

1.2.2. Bridge Failure Mechanisms during Floods 5

1.2.3. Bridge Failure Consequences and Network Performance Indicators 6

1.3. Aim and Objectives 8

1.4. Thesis Outline 9

2. Literature Review 12

2.1. Problem Identification 16

2.1.1. River Flow Computation 18

2.1.2. Hydrodynamic Forces Comparison. Focus on Drag Coefficient 19

2.1.3. Analysis of Flood Fragility 31

2.1.4. Large Wood Clogging Challenges at Modelling Stage 33
2.1.5. Simulations using River Analysis Software (RAS) 34
2.2. Empirical Fragility Analyses 35
2.3. Network Disruption Analysis 36
3. Bridges affected by the 2021 Flood in Germany 38
3.1. The Flooding event of July 14th–15th in Germany 38
3.1.1. Rainfall Distribution 39
3.2. Database of Damaged Bridges 42
3.2.1. Overtopping and Scouring Mechanisms 43
3.2.2. Classification of Damage according to DIN 1076 46
3.2.3. Population Statistics 49
3.3. Fragility Curves Generation 50
3.4. Results 53
4. Bridge Deck Vulnerability 59
4.1. Assumptions of the Proposed Method 59
4.1.1. General Assumptions 59
4.1.2. Description of Hydrodynamic Coefficients 60
4.1.3. Description of the Driftwood Clogging Probability 62
4.2. A Novel Approach to Bridge Deck Fragility Analysis 64
4.2.1. General Overview of the Novel Approach 66
4.2.2. Computation of Limit States (LS) 67
4.2.3. Fragility Analysis 70
4.3. Automating HEC–RAS 72
5. Bridge Deck Fragility Analysis Application 76
5.1. Description of the Region 76
5.2. Description of the Hydraulic Model and the Bridge 78

5.3. Application and Results 80
6. Network Analysis 86
6.1. The Detour-Impact Index 86
6.2. Analysis of the Study Area 90
6.3. Analysis of Traffic Data 91
6.4. Obtaining the Traffic through the Traffic Script 92
6.5. More Insights into the Traffic Script 94
6.6. Traffic Data Transformation: Qualitative to Quantitative 103
6.7. Bridge Collapse Scenario 104
7. Road Network Analysis and DII Application 108
7.1. Computation of DII 109
7.2. Validation of the Framework 111
8. Main Findings 113
8.1. Findings on Empirical Fragility Curves 113
8.2. Findings on Bridge Deck Vulnerability 116
8.3. Findings on DII Metric and Framework 117
8.4. Discussion on Interdisciplinary Themes 118
8.4.1 Discussion on the Drag Coefficient Comparison 120
8.4.2 Discussion on Hydraulic Forcing and Driftwood Clogging 121
8.4.3 Discussion on Modelling Features 122
8.4.4 Discussion on Road Network Disruption 123
9. Conclusions 124
9.1. Main Outcomes 124
9.2. Research Innovations 126
9.2.1. Empirical Fragility Curves for Riverine Bridges in Europe 127
9.2.2. Hydrodynamic Actions and Driftwood Clogging at Bridge Decks 127

9.2.3. Network-level Disruption Assessment Framework....128
9.3. Impact of the Research....129
9.4. Future Research....131
References....133

Resumo

No contexto das alterações climáticas, os eventos climáticos extremos tornaram-se mais frequentes e intensos, com impacto significativo e inesperado nas estruturas. As inundações causaram a maior parte dos prejuízos entre os desastres naturais, sendo também responsáveis por mais de metade dos colapsos de pontes. Estas questões revelaram a importância das pontes para a funcionalidade rodoviária, devido a possíveis perturbações para os passageiros e veículos de emergência. Surgiram questões sociais e económicas significativas nas zonas rurais devido à falta de opções de backup, resultando no isolamento de comunidades inteiras. A avaliação da resiliência das estradas rurais depende atualmente do acesso a conjuntos de dados específicos, o que limita a sua utilização prática. Este desafio está normalmente associado à disponibilidade de dados de tráfego. Esta investigação visa propor uma abordagem dupla, avaliando a vulnerabilidade da rede rodoviária nas zonas rurais com base numa nova métrica de perturbação, bem como obtendo a contabilização da fragilidade ao nível dos ativos para modos de falha recorrentes observados em dados de colapsos anteriores. Para este fim, este estudo elucida sobre as vulnerabilidades existentes das pontes às inundações dos rios, discutindo também áreas específicas em que os dados da literatura são contraditórios. Uma característica importante deste quadro é a sua adaptabilidade, uma vez que foi concebido para ser integrado com abordagens existentes. O método, tanto ao nível dos ativos como da rede, foi aplicado num estudo de caso de uma rede rodoviária rural na Toscana (Itália).

Palavras chaves: Força Hidráulica; Madeira Flutuante; HEC-RAS; Perturbação Rede Rodoviária.

Abstract

In the context of climate change, extreme weather events have become more frequent and intense, with significant and unexpected impacts on structures. Floods triggered most expenses among natural disasters, being also responsible for more than half of bridge collapses. These issues unravelled bridges' importance for the road functionality, due to possible disruptions to commuters and emergency vehicles. Significant social and economic issues emerged in rural areas due to a lack of backup options, resulting in the isolation of entire communities. Evaluating the resilience of rural roads currently depends on having access to specific datasets, which limits their practical use. This challenge is commonly associated with the availability of traffic data. This research aims at proposing a double folded approach, by assessing the road network's vulnerability in rural areas based on a new disruption metric as well as obtaining asset-level fragility accounting for recurrent failure modes observed in past collapse data. To this end, this study sheds light on existing vulnerabilities of bridges to river floods, also discussing specific areas in which literature data are contradictory. An important feature of this framework is its adaptability, as it was designed to be integrated with existing approaches. The method at both asset and network level was applied on a case study of a rural road network in Tuscany (Italy).

Keywords: Hydraulic Forcing; Driftwood; HEC-RAS; Road Network Disruption.

List of Figures

Figure 1. Structure of Thesis Objectives 9
Figure 2. Outline of the Thesis. Paragraphs' titles have been modified to improve understanding 11
Figure 3. Bridge Deck schematic cross-section and geometric parameters 20
Figure 4. Drag Coefficient (C_D) as a function of Inundation Ratio (h*) for different experiments 22
Figure 5. Proximity Ratio (PR) as a function of Inundation Ratio (h*) limited to h* = 3 24
Figure 6. Drag coefficient (CD) as a function of Proximity Ratio (PR) for the setups of Kerenyi et al. (2009) 25
Figure 7. Blockage Ratio (BR) as a function of Inundation Ratio (h*) and Proximity Ratio (PR) and the plane BR = 0.14 26
Figure 8. Influence domain of BR on CD. Each point in the graph represents a possible deck's position, given by PR, and maximum water elevation through hu within h*. For points under the curve, it is known that BR has a great influence on CD, and therefore higher drag values are expected when compared to situations above the domain's lines 27
Figure 9. Variation of Drag Coefficient (CD) as a function of Blockage Ratio (BR) for h* = 2 and Proximity Ratio PR = 2.3. Adapted from Malavasi and Guadagnini, (2007) 28
Figure 10. Daily accumulated precipitation (combined microwave-IR) 0.1 deg. [GPM GPM_3IMERGDF v06], July 14th – 15th , 2021 (Huffman et al., 2019). NUTS250 as basemap (BKG, 2022b), Waterbody-DE as source for the river shapefile (BfG, 2022). The accumulated precipitation is highlighted with different shades: darker (>90 mm/24h), intermediate (50 to 90 mm/24h), lighter (30 to 50 mm/24h) 39
Figure 11. The preliminary data from LfU provides information on how the peak discharge along the Ahr river has evolved over space and time (Landesamt für Umwelt Rheinland-Pfalz, 2022) 41
Figure 12. Debris accumulation in Eichenbach, a tributary of the Ahr river, characterized by: (a) the presence of wood logs, some of which measure up to 15 m in length, and (b) have an average diameter of approximately 17 cm for the carried logs. Photos shot by the Thesis' author 41
Figure 13. A spatial kernel density estimation has been applied to illustrate the distribution of damaged bridges, represented by dots (blue to red). The Ahr valley emerges as the region most severely affected. Additionally, it is evident that the upper segment of the river basin experienced the

highest hydrological stresses, indicated by darker red areas on the rainfall map, where rainfall exceeded 90mm. These conditions led to increased hydraulic forces along the watercourse. Other notable regions are highlighted based on the cumulative daily precipitation, with values falling within the range of 50 to 90mm denoted by red shading, and 30 to 50mm indicated by a lighter red hue. The rainfall dataset is taken from satellite data: (combined microwave-IR) 0.1 deg. [GPM GPM_3IMERGDF v06], July 14th – 15th , 2021 (Huffman et al., 2019). The Germany GIS map is taken from NUTS250 (BKG, 2022b), while the shapefile of Rhine and Ahr from Waterbody-DE (BfG, 2022) 42

Figure 14. Scour mechanisms observed during the survey include: (A) pit scour, (B) pier scour, (C) approach fill scour, and (D) channel flanking scour. These images were shot by the Thesis' author 44

Figure 15. Examined overtopping mechanisms include: (A) dragging of a wooden deck; (B) dragging of a steel deck; (C) railing damage resulting from overtopping; and (D) a combination of overtopping and scour, with the latter being the primary factor leading to structural failure. These images were shot by the Thesis' author 46

Figure 16. The proportions of arch bridges, beam bridges, heavy and lightweight decks concerning the two damage mechanisms 50

Figure 17. The definition of h** as IM for the fragility model 51

Figure 18. Confidence intervals for the damage states categorized as moderate and severe, specifically focusing on velocity data for Arch bridges. The 95% confidence intervals are prominently displayed along with the mean value derived from the fitted distribution 53

Figure 19. Fragility curves illustrating the susceptibility of heavy (HVY) and lightweight (LWY) bridge decks to severe damage under scour and hydraulic forcing (Hydr.) scenarios. The D4 designation corresponds to the damage level as defined in Table 5 54

Figure 20. Fragility curves depicting heavy bridges (HVY) under both scour and hydraulic forcing (Hydr.) scenarios, encompassing all damage levels including D2, D3, and D4 as per Table 5 55

Figure 21. Fragility curves illustrating the susceptibility of beam bridges to damage under the influence of scour and hydraulic forcing (Hydr.) mechanisms are presented. The damage levels, denoted as D2 and D4, are in accordance with the classifications outlined in Table 5 57

Figure 22. Fragility curves depicting the vulnerability of arch bridges to damage under scour and hydraulic forcing (Hydr.) scenarios are displayed. The damage levels, specifically denoted as D2, D3, and D4, align with the categorizations outlined in Table 5 57

Figure 23. On the left side are the elements of the Bridge Deck, and on the right side is a schematic representation of the forces in a cross-section (XS) view. For clarity, it is omitted the depiction of river embankments, wing walls, and approach ramps, which are meant to be located adjacent to the bridge abutments. The Inundation Ratio is indicated as h*. Water discharges are represented by Q1 and Q2, while hu and hb symbolize the water and deck elevation, respectively. The deck thickness is denoted as s, the width as w, and the bearing distance as d 61
Figure 24. Method's workflow to obtain fragility curves from a HEC-RAS bridge model 65
Figure 25. Scheme of the BrHyD program's functioning 72
Figure 26. Content of the files needed for the BrHyD execution 73
Figure 27. BrHyD GUI 74
Figure 28. Carrione river, with the location of the six locations of the upper basin that sustained major damages in the 2003 flood. The location of the case-study bridge is also indicated 77
Figure 29. The bridge over the Carrione river taken as case-study. It was built in 2007 and demolished in 2021 79
Figure 30. Slippage, Uplift and Overturning LS without driftwood clogging effect 82
Figure 31. Interpolated Fragility Curves for Various Scenarios with Driftwood Blockage: the Influence of Increased driftwood clogging can be noticed in the "Blockage Ratio" axis, where the blockage ratio 0.20 corresponds to the case of absent clogged wood logs, while higher values characterise added driftwood 83
Figure 32. Representation of FC at various clogging scenarios, indicated as a % of deck's thickness increment (Δs). The results are shown for slippage LS, where Δs = 0% corresponds to the Slippage curve of Figure 30. For each 10%, it results in Δs = 9.1cm increment of deck thickness; i.e., at Δs = 10%, the total deck thickness is: 0.91m + 0.1*0.91m = 1.00m 84
Figure 33. Effect of the recalibration of hydrologic model on the probability of failure, for slippage LS. The dashed line is employed for the first model (Tr1), while the continuous line displays the FC after the recalibration of the model (Tr2). As a result, P[SL | Tri] represents the conditional probability of failure for the slippage limit state (SL) given the original hydrologic model (Tr1) and the recalibrated hydrologic model (Tr2) 84
Figure 34. The DII (Detour–Impact Index) Method Flowchart 87
Figure 35. Failure scenario and example of alternative path. The network on the right side shows i=1 as the j-th path. The path considered as alternative is displayed on the left. In the specific case, i = 2 88

Figure 36. The flowchart of the Traffic Script, described in detail in § 6.4 92
Figure 37. The process of image assembling. In the specific case, images are retrieved from Google Maps© 93
Figure 38. The Level Of Service (LOS) comparison with the qualitative classification of Google Traffic . 93
Figure 39. Traffic Script GUI: input variables 95
Figure 40. Traffic Script GUI: output intermediate variables 100
Figure 41. The flowchart for quantitative traffic assessment 103
Figure 42. Bridge locations are at the intersections of road links with river 106
Figure 43. Identified paths between the Civil Protection Headquarter in Massa to the village of Avenza 110
Figure 44. The DII Matrix for the paths highlighted in Figure 43 110
Figure 45. Identified paths between the Civil Protection Headquarter in Massa to the villages of Forno on the right and Antona on the left 111
Figure 46. Bridges in series and bridges in parallel. With numbers 1 and 2 representing the bridges 119
Figure 47. Impact of the research and involved actors 130
Figure 48. Rupture faults at watersheds: (A) located on Steinbach creek, at Floh-Seligenthal, Thuringia (Germany) ; (B) located in a tributary creek of Eichenbach at Frohnhofen, RLP (Germany). Pictures taken by the author 132

List of Tables

Table 1. Multi-hazard studies including flood fragility.....17
Table 2. w/s comparison among the investigated studies.....30
Table 3. Works on fragility curves for flood.....32
Table 4. DIN 1076 definition of condition ratings for bridges (Haardt, 1999).....47
Table 5. Mapping bridge condition ratings to a qualitative damage level, determined by equivalence with the structural safety parameter 48
Table 6. Historical floods in Carrara, concerning the Carrione river.....78
Table 7. The incidence of concrete and steelwork for composite bridges spanning up to 20 80
Table 8. Fragility curves parameters without the driftwood effect.....81
Table 9. Parameters for the network displayed in Figure 42.....106
Table 10. Results, in terms of DII, according to the parameters of Table 9 and the network of Figure 42. Two assignments are included, for comparison purpose.....107
Table 11. ETAs for the present framework and the ETAs based on the web maps.....112
Table 12. Hydraulic forcing vulnerability levels in qualitative terms for lightweight (LWY), heavy (HVY) beam bridges and arch bridges. Symbols (+) to (++++) represent increasing vulnerability to hydraulic forcing. The damage levels D2 (slight), D3 (moderate), D4 (severe) are defined according to § 3.2.2 and h** according to § 3.3.....115
Table 13. Scour vulnerability levels in qualitative terms for lightweight (LWY), heavy (HVY) beam bridges and arch bridges. Symbols (+) to (++++) represent increasing vulnerability to scour. The damage levels D2 (slight), D3 (moderate), D4 (severe) are defined according to § 3.2.2 and h** according to § 3.3.....115

Glossary

Vocabulary	Definition
Backwater	The effect caused by a reduction in flow velocity due to the presence of an obstacle. It may result in increased water elevations upstream of the obstacle; in such cases it is called “backwater rise”
Basin	See Catchment
Bridge condition rating	Score associated to a bridge or/and a bridge element, given by qualified personnel after an inspection. Guidelines exist on how to justify the reduction in structural safety, durability and/or traffic safety
Bridge Deck	The bridge element that spans between supports, such as abutments and piers
Bridge failure	The partial or total collapse of a bridge
Bridge management system	A tool designed to manage, maintain and monitor a bridge stock
Buoyancy	The upward force exerted by water on an object partially or fully submerged in it. The mathematical model of buoyancy is the Archimedes’ principle
Catchment	The river catchment, known also as watershed or drainage basin, is the portion of territory delimited by higher terrain, in a way that all the runoff water in it, will flow in the same watercourse (or in its tributaries)

Channel flanking scour	A scour process occurring on the river's levee, by eroding soil and transporting it away from the riverbank
Clearance (of a bridge)	The minimum distance between the lowest point of a bridge deck and the water surface (or the terrain surface) underneath
Climate change	According to IPCC, climate change is a multifaceted phenomenon exhibiting a long-term shift from Earth's average climate
Contraction scour	Flow contraction generated by a narrowing of the watercourse which locally increases the water velocity. It usually occurs under a bridge, where the presence of abutments and piers, locally reduces the river flow cross-section area
Coping capacity	The ability of a society to respond and recover from disasters and long-term phenomena such as climate change
Critical scour depth	The maximum depth that a scour hole can reach in the proximity of a structure to ensure the stability and safety of the structure
Damming	The effect caused by accumulation of debris against an inline structure on a river, resulting in a certain degree of blockage to the flow
Delay-cost function	An analytic model employed to quantify the costs associated to an additional travel time experienced by road users
Detour-Impact Index (DII)	The ratio of the increased user costs following a disruption to the pre-event conditions

Digital elevation model	The term is also known with the acronym “DEM”. It provides elevation data where all non-ground features are filtered off. It is distinguished from DTM (Digital Terrain Model), although in some countries the two terms are synonyms. Together with the DEM and DTM, it exists also the DSM (Digital Surface Model), which includes natural and man-made objects elevation
Discharge (of a river)	The volume of water per unit of time; defined in mc/s or cfs/s
Disruption	The term is multidisciplinary; nevertheless it can be generally referred to a disturbance of an activity that causes a significant reduction in operational actions related to that activity
Distributed hydrologic model	A mathematical model used to describe the hydrologic processes related to a certain portion of territory. The area under study is discretised in cells, and equations of hydrologic processes are defined within each cell. The connection between adjacent cells is also accounted for in the model. The model, unlike lumped ones, can better describe the spatial variability of hydrologic processes and water runoff within a river catchment, due to its higher resolution
Dragging	See Slippage
Driftwood	Floating Large Wood. See also: Large Wood
Driftwood clogging	Damming effect due to a build-up of entrapped drifting wood logs
Driver's time cost	Cost for individuals undertaking trips of different purposes (work or non-work), while driving a vehicle of a specified class

Estimated time of arrival	A prediction of trips' duration, by taking the current (or future) road network conditions as inputs. The time of arrival is calculated by adding to the present time (or to the planned time of departure), the predicted trips' duration
Extreme value theory	A statistical theory used in various disciplines. In the context of hydrology, the extreme value theory uses series of historical extreme values of a certain variable, to model the occurrence probability and magnitude of such variable
Flood hazard	A flood event that has the potentiality to cause damages
Flood Directive	The Directive 2007/60/CE is a framework dedicated to enhancing the management of flood risk and minimizing the possible negative impacts of floods in EU member states
Flood Risk	The product of the occurrence probability and consequence estimates of a flood event, for a given hazard magnitude
Fragility curve	Probability of failure of defined structural thresholds for a given magnitude of hazard intensity measure
Freeboard (of a bridge)	Gap between the water surface and the girder soffit considered at the occurrence of the design peak discharge
Gauged river	A river on which one or more hydrometric stations are placed to measure the water elevation
Girder (of a bridge)	The group of load-bearing elements of a bridge deck
Hydraulic forcing	The interaction of static and dynamic component of the flow with the bridge

Hydraulic model (no physical)	An analytic representation of hydraulic processes and water flow that uses mathematical and – often – also informatic tools to reproduce real-world phenomena
Hydrodynamic Action / Thrust	The dynamic component of a mass of fluid in motion. The other component is called hydrostatic action / thrust
Hydrologic model	An analytic representation of hydrologic processes that uses mathematical and – often – also informatic tools to reproduce real-world phenomena
Intensity measure	In fragility analysis, the intensity measure is the variable designated to represent the magnitude of the hazard under study. For flood hazard, the flow velocity, the discharge or the water elevation can assume the role of intensity measures
Inline structure	A structure that is placed as a barrier or span over a watercourse such as weirs, bridges and dams
Kernel density	A non-parametric statistic method used to estimate the probability density function of the input variables. It employs a kernel function that is centred on each data point and subsequently used to calculate the weighted contribution of that point to the overall probability
Large Wood	Wood logs with diameter $\geq$ 10 cm and length $\geq$ 1 m
Level of service	A qualitative measure of the traffic performance and congestion, used to communicate in a standardised format the working conditions of a specific road link, crossing or lane
Lift	See Uplift

Limit State	A function representing the failure domain of a structural element due to a given phenomenon, according to specific performance and safety requirements
Monte Carlo Simulation / Analysis	A method that uses random sampling to generate a set of input variables and execute multiple trials on the same simulation model
Origin-Destination matrix	A matrix used in transportation field, where the columns represent the origins and the rows the destinations. The numbers in the cells represent the vehicles or the trips, the people, the goods, assigned to that origin – destination pair
Overtopping (of a bridge)	The scenario in which the water started to flow on top of the bridge deck
Overturning	Rotation of the bridge deck causing its collapse
Peak discharge	Maximum expected water volume per unit of time. It is the highest value on a Hydrograph
Pit scour	Scour-triggered hole in the riverbed material in the proximity of instream objects such as bridge piers
Reach (of a river)	A specific river segment between two pre-assigned points, as confluences, bridges, gauge stations. It is common in hydraulic engineering to study a specific portion of a river, by defining the upstream and/or downstream boundary conditions, which are defined at the start and end of the reach
Recovery profile (structure)	The process that involves restoring the structure's functionality after a disruption that caused its reduction

Risk aversion	The propension of a person to decide for a lower-gain and lower risky option and lose a higher-gain and higher risky one, to avoid negative consequences
River discharge	See Discharge
Riverbed aggradation	The sedimentation process on a riverbed. It reduces the river slope where it occurs
Riverbed degradation	The erosion process on a riverbed. It increases the river slope where it occurs
Scour	The erosion of soil due to water action from riverbed and riverbanks in the proximity of bridge foundations. It is distinguished from riverbed degradation because it occurs with a local hydraulic interaction between the structure and the riverbed material
Slippage	The failure mechanism that results in deck movement in the direction parallel to the water flow. It is mainly but not entirely due to the pressure component acting parallel to the direction of the river flow. The other component (uplift) contributes to the failure mode through an upthrust
Soil shrinkage	When the soil is exposed to drought periods, it reduces its water content and this phenomenon may result in cracks produced by the excessive tensile stress within the soil, as the particles come closer
Tributary (of a river)	A smaller river reach, eventually flowing into a main river
Ungauged river	A river on which no hydrometric stations are placed to measure the water elevation

Uplift	A failure mechanism that results in deck raise from its position. It is caused by the algebraic sum of the buoyancy and the dynamic lift, which is the dynamic pressure component acting normal to the direction of the flow.
Vehicle operative cost	The sum of costs occurring during vehicles' operation, including and not limited to: fuel, maintenance, wear, insurance, taxes.
Water stage	The height of the water above the riverbed

Abbreviation List

Acronym	Extended Name
AASHTO	American Association of State Highway and Transportation Officials
ADT	Average Daily Traffic
AI	Artificial Intelligence
AMC	Antecedent Moisture Condition
ANN	Artificial Neural Network
ANOVA	Analysis Of Variance
API	Application Programming Interface
AR&R	Australian Rainfall and Runoff
AS	Australian Standards
ATC	Applied Technology Council
BASt	Bundesanstalt für Straßenwesen (Federal Highway Research Institute)
BfG	Bundesanstalt für Gewässerkunde (Federal Institute of Hydrology)
BKG	Bundesamt für Kartographie und Geodäsie (Federal Agency for Cartography and Geodesy)
BrHyD	Bridge Hydraulics and Driftwood software
CAT	Catastrophe
CEN	European Committee for Standardization
CFD	Computational Fluid Dynamics
CIRIA	Construction Industry Research and Information Association
CLE	Condizione Limite per l'Emergenza (Emergency Limit Condition)
DEM	Digital Elevation Model
DII	Detour – Impact Index
DIN	Deutsches Institut für Normung (German Institute for Standardization)
DMS	Degrees Minutes Seconds
DOT	Department Of Transportation
DTC	Driver's Time Cost
EEA	European Environment Agency

EN	European Norm
ETA	Estimated Time of Arrival
EUR	Euro – currency with symbol: €
FC	Fragility Curve
FEH	Flood Estimation Handbook
FEMA	Federal Emergency Management Agency
FFS	Free – Flow Speed
FHWA	Federal Highway Administration
Fr	Froude Number
GCM	General Circulation Model
GIS	Geographic Information System
GPM	NASA's Global Precipitation Measurement Mission
GUI	Graphical User Interface
HCM	Highway Capacity Manual
HEC	Hydrologic Engineering Center
HEC–RAS	River Analysis System software of the Hydrologic Engineering Center
HVY	Heavy Bridge Decks
Hydr.	Hydraulic Forcing
IJ1	Code Language of ImageJ Software
IM	Intensity Measure
K–S	Kolmogorov–Smirnov Test
K–W	Kruskal–Wallis Test
LAT	Latitude
LFRD	Load and Resistance Factor Design
LfU	Landesamt für Umwelt (State office for Environment)
LON	Longitude
LOS	Level of Service
LS	Limit State
LVermGeo	Landesamt für Vermessung und Geobasisinformation (State office for Measurement and Geographic Information)
LW	Large Wood
LWY	Lightweight Bridge Decks

MDOF	Multi Degrees Of Freedom
MOBIDIC	Modello Bilancio Idrologico Distributo e Continuo
NBI	National Bridge Inventory
NRI	Network Robustness Index
NRW	Nordrhein-Westfalen (North Rhine-Westphalia)
NTR	Network Trip Robustness
NWC	North – West Corner (of a georeferenced image)
O–D	Origin – Destination
OSM	Openstreet Map
OTM	Open Transport Map
RFF	Regional Flood Frequency
RLP	Rheinland-Pfalz (Rhineland-Palatinate)
RM	Rational Method
SDOF	Single Degree Of Freedom
URL	Uniform Resource Locator
USGS	United States Geological Survey
UTM	Universal Transverse Mercator
VBA	Visual Basic for Application
VOC	Vehicle's Operative Cost
XS	Cross – Section
WGS84	World Geodetic System 1984

List of Equation Symbols

Symbol	Name
ADT_{ik}	Average Daily Traffic of the k–th road link of the i–th path
ADT_j	Average Daily Traffic of the j–th path (traffic to be detoured)
B	Bridge Deck Span Length (used only to compute Driftwood's characteristics)
B_R	Blockage Ratio
B_{RF}	Rectangular Portion of the Buoyancy Force
B_T	Triangular Portion of the Buoyancy Force
$\beta_1, \dots, \beta_7$	Regression Coefficients to determine the Clogging Probability of Logs
β_d	Standard deviation value of the Lognormal Cumulative Distribution Function, at *d*
β_k	Standard deviation value of the Lognormal Cumulative Distribution Function, at *k*
C_1, C_2	Constants to be calibrated for the relationship $T_r(Q)$
$\mathrm{C_D}$	Drag Coefficient
$\mathrm{C_L}$	Lift (or Uplift) Coefficient
C_m	Moment Coefficient
c	Capacity of a road link in vehicles/hour
D	Driftwood set of dimensions (to be used for conciseness in the clogging scenario)
DC_k	Daily Delay Costs in the k–th road link in the post-hazard scenario
D_i	Log Diameter (used only to compute Driftwood's characteristics)
DII	Detour–Impact Index
DS^*	Damage State in the clogging scenario
DS, ds_k	Respectively, the generic and the k–th Damage State
DTC_{ir}	Cost per unit of time associated with the user's trip purpose on vechile of class *r*
d	Distance between bearings measured on the same abutment
ΔH_i	Increment of Costs associated to the post-hazard scenario in the i–th path
ETA_m	Estimated Time of Arrival (ETA) calculated using the proposed method
ETA_w	Estimated Time of Arrival (ETA) calculated using web-based services
F_1	Asset (bridge) number one
F_2	Asset (bridge) number two

F_D	Drag Force
$F_d(r)$	Lognormal Cumulative Distribution Function for intensity *r* and damage state *d*
F_L	Lift (or Uplift) Force
F_{ser}	Failure of the Assets as a series system
F_{par}	Failure of the Assets as a parallel system
F_Z	Deck's Weight
G_{sqm}	Steelwork tonnage for the Deck
g	Acceleration of Gravity
$g(x)$	Generic Limit State Function
H	Bridge Clearance (used only to compute Driftwood's Blocking Probability)
H_{ij}	Deck's horizontal capacity against Dislodging
h	Upstream Water Elevation (used only to compute Driftwood's Blocking Probability)
h^*	Inundation Ratio
h^{**}	Ratio between h_u and h_b
h_b	Bridge Clearance
h_{cg}	Distance from the rotation point to the deck's centre of gravity
h_u	Upstream Water Elevation (Upstream the Bridge)
IM, im_i	Respectively, the generic and the i–th Intensity Measure
J	HCM calibration parameter
L_L	Log Length (used only to compute Driftwood's characteristics)
L	Link length (only for network analysis)
L_{cg}	Distance from the rotation point to the rightmost bearing
L_d	Bridge Deck Span Length
L_{ik}	Length of the k–th road link of the i–th path
M_{cg}	Overturning Moment evaluated with respect to the deck's centre of gravity
μ	Friction Coefficient at the interface of the girder and the bearings
μ_d	Mean value of the Lognormal Cumulative Distribution Function, at damage state *d*
μ_k	Mean value of the Lognormal Cumulative Distribution Function, at damage state *k*
N_c	The c–th simulation in the Monte Carlo Analysis for a given h^*
NC_{jk}	Daily Delay Costs in the k–th road link in the pre-hazard scenario in the j–th path
NC_k	Daily Delay Costs in the k–th road link in the pre-hazard scenario

NH_j	Costs in the pre-hazard condition evaluated in the j–th path (to be closed afterwards)
N_{tot}	The total number of simulations in the Monte Carlo Analysis for a given h^*
$NVOC_{jk}$	Vehicle's Operative Costs in the k–th road link in pre-hazard scenario and j–th path
$NVOC_k$	Vehicle's Operative Costs in the k–th road link in the pre-hazard scenario
n_d	Number of elements or specimens of empirical data
n_{MC}	Number of iterations in the Monte Carlo analysis
n_Q	Number of flow profiles set on HEC–RAS
O_V	Overturning Mechanism Limit State Equation
P	Clogging Probability of Logs
P_f	Bridge Deck Probability of Failure
P_{LM}	Maximum Clogging Probability
P_M	Clogging Probability for a single wood Log
P_R	Proximity Ratio
p_{ir}	Percentage of r class of vehicle within the i–th path
Q, q_i	Respectively, the generic and the i–th River Discharge
Q^*	Pseudo-Discharge (Intensity Measure in the clogging scenario)
R_0	Link Traversal Time under Free-Flow speed conditions
R_c	Link Traversal Time under post-hazard conditions
R_t	Link Traversal Time
r_i	i–th value of intensity measure r
ρ_{cls}	Concrete density
ρ_w	Water Density
S_{aik}	Average reduced speed of the k–th road link of the i–th path
S_L	Slippage Mechanism Limit State Equation
S_{LOS}	Mean Value of Level Of Service (LOS) speed range
S_{nk}	Average speed of the k–th road link in the pre-hazard scenario
s	Bridge Deck Thickness
s_{cls}	Volume of concrete per square meter of Deck Surface
s_{wet}	Wetted portion of the Deck Thickness
T	Reference time period for the computation of v
T_{aik}	Traversal Time of the k–th road link of the i–th path

T_r	Return Period, in years
U_P	Uplift Mechanism Limit State Equation
VOC_k	Vehicle's Operative Costs in the k–th road link in the post-hazard scenario
V_u	Upstream Water Velocity
v	Volume of vehicles per hour crossing a road link
v_{upd}	Volume of vehicles per hour crossing a road link, updated for the post-hazard scenario
$wetDN$	Wetted Downstream portion of the Deck Thickness
$wetUP$	Wetted Upstream portion of the Deck Thickness
w, w_d	Bridge Deck Width
$x_1, \dots, x_7$	Predictor Variables of the Regression to determine the Clogging Probability of Logs

1. Introduction

Bridges are key elements in a road network, ensuring robustness during and in the aftermath of a disruption (Argyroudis *et al.*, 2020). Literature works recognise that probabilistic methods are necessary to estimate the performance of infrastructures, especially in a continuously changing climate scenario, which induces unexpected loads on structural elements (Loli *et al.*, 2022). This issue is particularly noticeable for floods, being it the first cause for bridge failures worldwide (Proske, 2018).

Therefore, innovative models and tools need to be developed to analyse the impact of floods on bridges in a more holistic perspective, in light of increasingly frequent extreme events. Chapter 2 discusses relevant literature works linked to the river flow, hydrodynamic forces and driftwood clogging computation. In addition, it is presented a state of the art concerning fragility curves for bridges subjected to floods, as well as the road network disruption metrics as a consequence of a bridge collapse. In Chapter 3 are identified recurrent bridge failures using large sample of collapsed structures, drawing fragility curves for a bridge portfolio based on the typology and deck's material, by using a case-study located in Germany. Chapter 4 focuses on a new approach to assess hydrodynamic actions and driftwood clogging on single-span decks, while an application of it is given in Chapter 5. Chapter 6 takes the issue at a wider scale, identifying key variables to measure the disruption on road users due to a bridge collapse. Within Chapter 7 the methodology presented in Chapter 6 is demonstrated on a case-study located in Italy. The present Chapter, focuses on the motivation that led to the development of this research, discussing issues on the behaviour of bridges at high water stages, as well as the consequences of a bridge damage/failure at network level. Indeed, social and economic challenges at community levels originate from local structural and hydraulic phenomena, which may trigger cascading effects on road network at various scale, i.e., municipal, regional, national.

1.1. Problem Identification

The rate of emergency situations related to extreme weather events is strongly increasing, stressing infrastructures and economy (Chen *et al.*, 2015). Transportation networks play a vital role both

in the management of crisis and in the recovery phase, since evacuations and economic activities rely on the connections provided by roads and railways (Palin *et al.*, 2021).

In such perspective, a known problem affecting Europe is the generalised absence of an organised strategy to comply with the Flood Directive, issued in 2007, with the aim of reducing flood-related risks (European Court of Auditors, 2018).

Specifically, Austria, Czech Republic, Italy, Portugal, Romania and Spain failed to quantify the totality of costs and/or the sources of funds to enact the interventions highlighted in the Flood Directive plans (European Court of Auditors, 2018). In Italy, just in the hydrographic district of eastern Alps the costs of planned works to meet the Flood Directive's recommendations are of 1.1 billion EUR higher than the available funds. In addition, expenses due to hydrogeologic-triggered disasters in the period 1947-2012 in Italy are estimated to be approximately 213 billion EUR, while only 40 billion EUR would be needed to repair and strengthen the existing infrastructure stock (Bini *et al.*, 2012).

The frequency of secondary road bridge failures is quantified to represent the majority of such occurrences, as 70% of the Italian bridge stock is located on this road typology (Giresini, Puppio and Sassu, 2016; Sassu, Giresini and Puppio, 2017). Despite the high number of collapsed bridges, such failures did not mobilize the society disapproval, and only after the collapse of a major infrastructure (i.e. the Polcevera Viaduct in Genoa) the Italian Government issued a law (130/2018) in which, among other measures, a national census database of infrastructures was established (Ministero Infrastrutture e Trasporti, 2018).

In Italy, as in other countries, society is impressed more by one big event than by several smaller and recurrent ones. Examples of this premise are the measures introduced after some major bridge failures. In 1940, the collapse of Tacoma Narrow bridge significantly changed the design of suspension bridges (Washington DOT, 2020). After the 1967 Silver bridge collapse, the National Bridge Inventory (NBI) was established and was mandatory to report in the database each (federal) bridge above 6 m [meters] (Dekelbab, Al-Wazeer and Harris, 2008). Another major infrastructure collapse in 2007, namely the I-35W bridge, stressed the attention on the indirect consequences of such failures. In that case, several studies were performed to also understand the users' behaviour during emergencies, highlighting the differences in the short-term and long-term effects on society and economy (Xie and Levinson, 2011). Furthermore, another factor that still nowadays negatively influences the response of a society and leads to deaths and damages is the low risk perception leading to claim the right to freely move even during heavy weather events, despite alerts issued by the Civil Protection Department (Ciullo *et al.*, 2017).

It is notable that among natural hazards, flood is the one that it can be forecasted the most, but still the collapse of a bridge is rarely seen as predictable (Rania *et al.*, 2019). Hence, there is the need of practical tools aimed to increase preparedness actions rather than mitigation measures.

The research world has undertaken this challenge by developing innovative frameworks by accounting for all the mentioned issues. Nevertheless, due to existing distance between academia and industry, it is of paramount importance to bring research approaches closer to current engineering practice. To appropriately address this issue, the analysis of past events can reveal important gaps in current management schemes and unforeseen failure mechanisms leading to disasters. Therefore, in Chapter 3, the 2021 Ahr valley flood in Germany serves then as an exemplary case to emphasise the significance of certain failure mechanisms. In Chapter 4 an analytical framework is presented to evaluate these failure mechanisms, and demonstrated in Chapter 5 in a specific case study conducted in Italy by using current engineering practice computer programs and in-house developed Python-based software.

Then, a road network analysis is conducted to measure the overall impact of a bridge collapse on the road users by developing a new metric, presented in Chapter 6, that can be used with open source technology and transportation engineering knowledge.

1.2. Motivation

In the last few decades, all studies confirmed that floods are the leading cause of failures for bridges (Wardhana and Hadipriono, 2003; Proske, 2018; Xiong *et al.*, 2023). Interestingly, statistical techniques applied to a collapsed portfolio of bridges in the USA revealed that neither the period of construction nor the bridge design improvements and maintenance regulations had significantly reduced the failure rates (Cook and Barr, 2017). Concerning this point, the worldwide perspective is rather fragmented. Despite scour-related Limit States are indicated in current standards, hydraulic forcing is often neglected or partially included, as explained hereafter.

Hydraulic forcing meant as the interaction of static and dynamic component of the flow with the bridge. The phenomenon is usually accounted for instream piers in existing codes, while the inclusion of this effect on decks is vague, which represents a significant gap.

Several countries, such as the USA and Australia, specifically account for water actions on bridge decks, while there is a lack of an exhaustive formulation in most of the European countries.

In Australia, hydrodynamic actions are included in standards since 2004 with a major update in 2017 (Committee BD-090, 2017). In the USA, the AASHTO LRFD Bridge Design Specifications explicitly consider such actions with well-defined Limit States and design equations. In addition, practitioners are provided with a set of manuals and software to model the rainfall-runoff processes as well as river hydraulics (AASTHO, 2012).

Concerning Europe, the EN1997 (CEN, 2005b) provides some Limit States but mostly referred to geotechnical aspects, while hydraulic forcing loads are considered just during construction (CEN, 2005a). Although EN 1991-1-6:2005 gives few indications, the main issue is that it covers only the building phase, leaving to the designer the burden of establishing a proper safety level against water forcing. Few countries have explicitly accounted for water actions in their National Annexes. This is mainly due to local hazards attributable to geographical locations, as the Annexes of Finland and Norway explicitly consider hydrodynamic forces and ice impacts (CEN, 2005).

1.2.1. Hydrologic and Hydraulic Overview

To determine the impact of flood actions on bridges it is commonly considered that at least two models would be needed: (i) hydraulic and (ii) hydrologic ones. Indeed, the prediction of the runoff volume is affected by the selected hydraulic and hydrologic model.

Within the European context, besides the gaps highlighted in § 1.2, the absence of a common European approach for discharge predictions allowed for different levels of uncertainty concerning for example the peak discharge computation. Other countries, such as Australia, periodically release a guideline for flood estimation (Jacobs and Ryan, 2021). The procedures described in the Australian Rainfall and Runoff (AR&R) document, which in 2019 arrived at its 4th edition, is implemented in a software, to provide engineers with an end-user tool to quickly estimate the expected flood magnitude in specific sites. The simplest methods in the guideline mainly comprise event-based approaches, as the Rational Method (RM). However, in its 2019 version, the AR&R guideline limited the use of RM in favour of regional methods. In the USA, the USGS periodically updates its Regional Flood Frequency (RFF) equations, developed within a National Flood Frequency Program (Ries III *et al.*, 2007). In Europe the situation is rather fragmented, with some countries that adopted an official rainfall to runoff management such as the UK (Kellagher, 2013), but have also independent national-level initiative as the Flood Estimation Handbook (FEH) and software developed by the UK Centre for Ecology and Hydrology (Kjeldsen, Jones and Morris, 2014). In Italy, the pluviometry is handled by the Regions, and each local

agency applies its own method to derive the rainfall parameters. Furthermore, the runoff models are often developed differently in each region. As an example, in Tuscany there is not an RFF set of equations, and the only official distributed hydrological model (Yang, Castelli and Chen, 2014) is applied to only portions of territory (Castelli *et al.*, 2014). In such cases, the absence of a guideline may result in a different accuracy of the discharge rate. Thus, the bridges built in the same region may have different safety levels to floods, given by the different accuracy of the runoff method used to predict the peak discharge or the hydrograph. This aspect has political and juridical implications, which are relevant to discuss, but out of the scope of the present Thesis.

1.2.2. Bridge Failure Mechanisms during Floods

Collapses of bridges can be used as basis for code improvement, as they reveal insights on real failure mechanisms. Past collapses highlighted recurrent failures in different contexts. Concerning flood-related failures, a first subdivision can be made on the triggering mechanism. From the hazard point of view a bridge can be damaged by hydraulic-forcing or by scour.

Referring to existing structures, in case of scour, the main issue concerns the time and tests needed for a proper characterization of the bridge substructure and soil foundation type. This task is usually performed on a limited number of assets, due to economic constraints (Wang *et al.*, 2019). Hence, it can be appropriate to divide the condition assessment in different levels of growing accuracy, by using more accurate analyses only on the most vulnerable assets. A first step may involve evaluating the probability of failure with simplified procedures. Indeed, there are different methods to assess the scour depth based on limited site data (Holnbeck and Parrett, 1997; Pearson, Jones and Stein, 2000; Govindasamy *et al.*, 2012).

These probabilities of failures are useful for a first screening of the bridge stock, while more refined models can be applied on specific assets. Examples of probabilistic failure modes under scour are exhaustively discussed in the work of Dong and Frangopol (2016). Challenges in this regard are mainly related to the applicability of such methods to a large-scale portfolio of structures. The main issue concerns the availability of data needed for the application of accurate models.

The other triggering mechanism, namely hydraulic forcing is usually considered in offshore structures due to wave actions. To this end, hurricanes are known to cause damage to coastline bridges also, due to the ocean surge (Robertson *et al.*, 2007; Padgett, Spiller and Arnold, 2012).

For riverine floods, although scour is the leading cause of collapse, hydrodynamic actions are increasingly reported to cause damage (Loli *et al.*, 2022). Specifically, hydraulic forcing is a major threat to bridge decks, especially to the simply supported ones, due to three reasons:

i) the increased frequency of extreme rainfalls (Wasko *et al.*, 2021);

ii) the lack of maintenance at catchment's level causing driftwood and debris mobilisation (Guimarães *et al.*, 2021);

iii) the absence in structural codes of hydraulic-related limit states.

The first issue can be tackled by linking the variation in hydrologic model parameters to the structural safety. To assess these effects, new structural Limit States are required (this is linked to (iii)). However, the definition of new LS must include an assessment of expected driftwood and debris actions (ii).

Therefore, the safety of bridges against hydraulic forcing is a multidisciplinary problem to be tackled at various levels of detail. Within this perspective, past collapses reveal how the aforementioned aspects interact.

1.2.3. Bridge Failure Consequences and Network Performance Indicators

The consequences of such collapses have also transportation wise impacts, given a sudden reduction of network functionality (Mackie and Stojadinović, 2006). This loss is usually associated to restrictions imposed to vehicle's weight, speed and may even include detours. The overall network performance can be assessed through indicators such as users' travel time (Capacci, Biondini and Titi, 2020). The Network Robustness Index (NRI) allows to assess the effects that a local disruption causes to the whole network, by relating the performance of road links to the travel time cost (Scott *et al.*, 2006).

The concept was further developed by several authors, including accessibility measures (Kermanshah and Derrible, 2017) and applicability to other networks such as the Internet (Nagurney and Qiang, 2007). Despite improvements, algorithms to evaluate infrastructure networks performances are in great demand (Ghosn M. *et al.*, 2016). Challenges concern the availability of traffic data and tailored solutions to iteratively simulate link closures.

The network functionality can be only evaluated after establishing the recovery profile of the single asset, which depends on the failure mechanism that caused the road disruption and its damage level. In

this case, the system is the road network where the bridges are located. Capacci *et al.* (2020) proposed a method to assess the system functionality after certain limit states are reached with respect to a specific seismic hazard. The total travel time is assumed as a measure of the network performance. The resilience is then a function of the network shape and consequently hazard independent.

Furthermore, through the analysis of past collapses it can be recognised that natural factors are key-elements having an influence on the recovery profile of the asset, as also the structure's surroundings must be resilient (Wang *et al.*, 2014). This implies that the survey of the structure itself is not sufficient, or not anymore sufficient, as the increasing frequency of storms, combined with a scarce maintenance of the smaller mountainous creeks, are causing faster changes in the rivers' equilibrium (Wang, Yu and Liang, 2017).

Although more complex approaches exist that incorporate both traffic, hazard and structural simulation methods (Green *et al.*, 2017), this study aims to demonstrate a potential strategy to address the aforementioned needs by innovations within each subject.

Specifically, this study adopts a systematic approach to address the issues presented in § 1.1 and 1.2, by developing a multidisciplinary framework that examines failure mechanisms (i.e., hydraulic forcing and driftwood clogging on bridge decks) not properly addressed in current codes and the dynamic correlation between these local failure mechanisms and the impact of resulting disruption on transportation networks. It explores the impact of severe flood events on bridges, including hydrodynamic forces. To shed light on recurrent failure mechanisms, the bridges located along the Ahr River in Rheinland-Pfalz, Germany, served as case study due to the 2021 flood that affected the area, causing damages to more than 250 bridges within 12 hours. The case-study is used to develop empirical fragility curves for recurrent failure modes.

Conversely, the analytic part of the framework is tested on the Municipalities of Massa and Carrara, located in Tuscany, Italy. Both municipalities experienced floods in the past decades, making them an ideal representation of a heavily human-influenced area where river reaches have been diverted or modified to accommodate urban needs. These towns serve as the primary focus of this research. The significance of this case study is further amplified by the availability of data and strong collaborations with the Tuscany Region Hydrogeological Asset Department.

1.3. Aim and Objectives

This work aims to develop a series of tools to assess impacts of hydraulic forcing and driftwood clogging at bridges and the effects of a bridge failure on the road network, including climate change scenarios.

The work aims to achieve the following objectives:

Objective 1. Understanding recurrent failure modes of bridges at high water stages by using past floods as evidence to review the adequacy of current standards facing climate change. This objective highlights the need to shift current engineering practice towards novel approaches in the design and assessment of water forcing on bridges.

Objective 2. Develop a new framework to assess water forcing on bridge decks under current and future climatic conditions. The framework aims at being used with currently available programs, but including new limit states and a probabilistic approach.

Objective 3. Apply the framework to a case-study, quantifying the changes in safety levels according to varying flow discharge and driftwood clogging levels. The application of the novel approach demonstrates how to assess the vulnerability of bridge decks within changing climate scenarios by adding new limit states and using a distributed hydrologic model.

Objective 4. Assess the network impact of a bridge collapse from the user's point of view. The method aims to fill gaps in existing approaches by assessing the performance of a road network by comparing user's costs following a bridge collapse to the stationary pre-event conditions. The framework also addresses traffic data availability issues in rural areas.

Objective 5. Assess the network-level performance on a case-study, to demonstrate the feasibility and applicability of the proposed framework, which is so validated.

The main outcome of this work is to provide ready tools to improve the safety design and assessment of bridge decks during floods and improve the coping capacity of stakeholders and

communities by analysing disruption scenarios at system level, identifying vulnerabilities at both asset and network scale, under current and future climate scenarios.

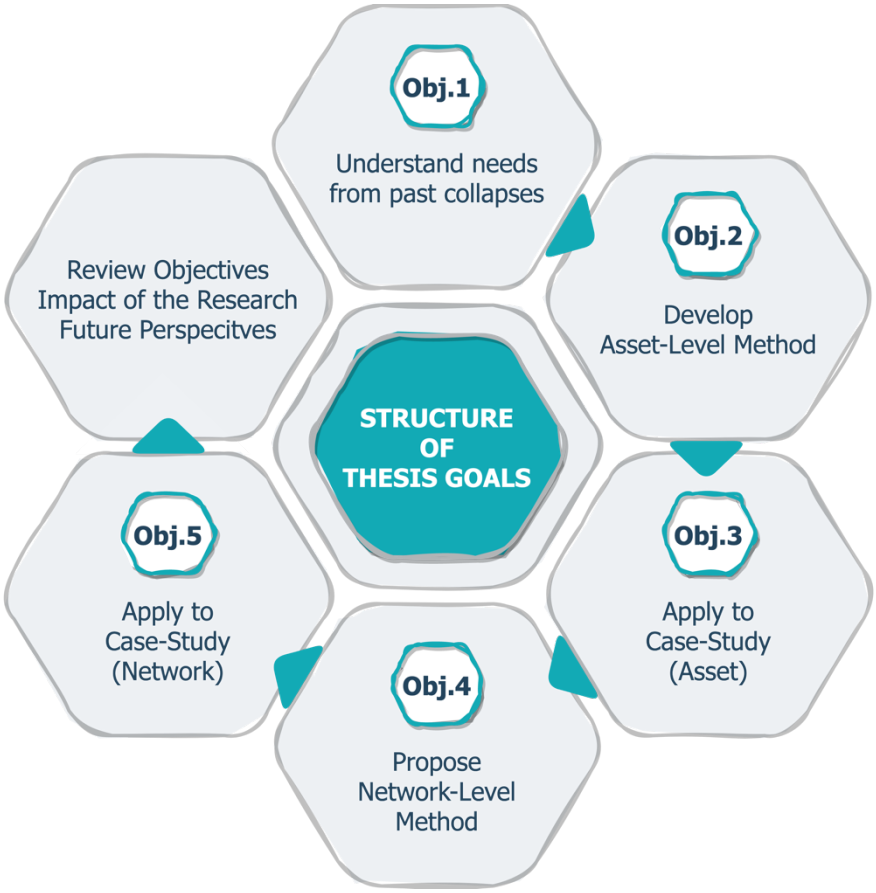


Figure 1. Structure of Thesis Objectives

1.4. Thesis Outline

The thesis overview is highlighted in Figure 2.

This Ph.D. thesis integrates material from three published articles on peer-reviewed Science Citation Index Expanded (SCIE) journals as original contribution from the work of the Author (Pucci *et al.*, 2021; Pucci *et al.*, 2023a; Pucci *et al.*, 2023b).

Chapter 2 outlines the literature related to the present work, highlighting current gaps to be filled as well as providing an overview of topics covered in the following chapters.

Specifically, Chapter 3 describes the analysis of collapsed bridges during the 2021 flood in the Ahr valley (Germany), including surveys, data collection from local authorities and the reconstructed event from hydraulic simulations. The data is used to derive fragility curves grouped by deck's material and mode of failure. Results stressed the need for updating current standards due to the relevance of

unaccounted limit states such as those produced by hydraulic forcing and driftwood clogging on bridge decks.

Chapter 4 introduces the novel approach to determine bridge decks vulnerability to water forcing and driftwood clogging by using current software and in-house developed scripts. The Chapter also discusses the proposed shift in bridge design. In particular, it is suggested a change in the paradigm of fixing the maximum water stage without considering future climatic scenarios, towards a more flexible approach, which includes peak discharge values obtained from various recalibrations of hydrologic models. The application of the method is illustrated in Chapter 5.

Chapter 6 is dedicated to the road network analysis in case of bridge collapse. The work also discusses traffic data availability issues, by presenting a method to derive it starting from qualitative data. The case-study is presented in Chapter 7.

Chapter 8 summarises the main findings and discusses interdisciplinary themes, while Chapter 9 is focused on explaining what are the research innovations as well as implications for policy makers, practitioners and stakeholders in the management of a bridge portfolio. Then, the work concludes by reviewing the accomplishment of the objectives as well as introducing possible improvements in the method.

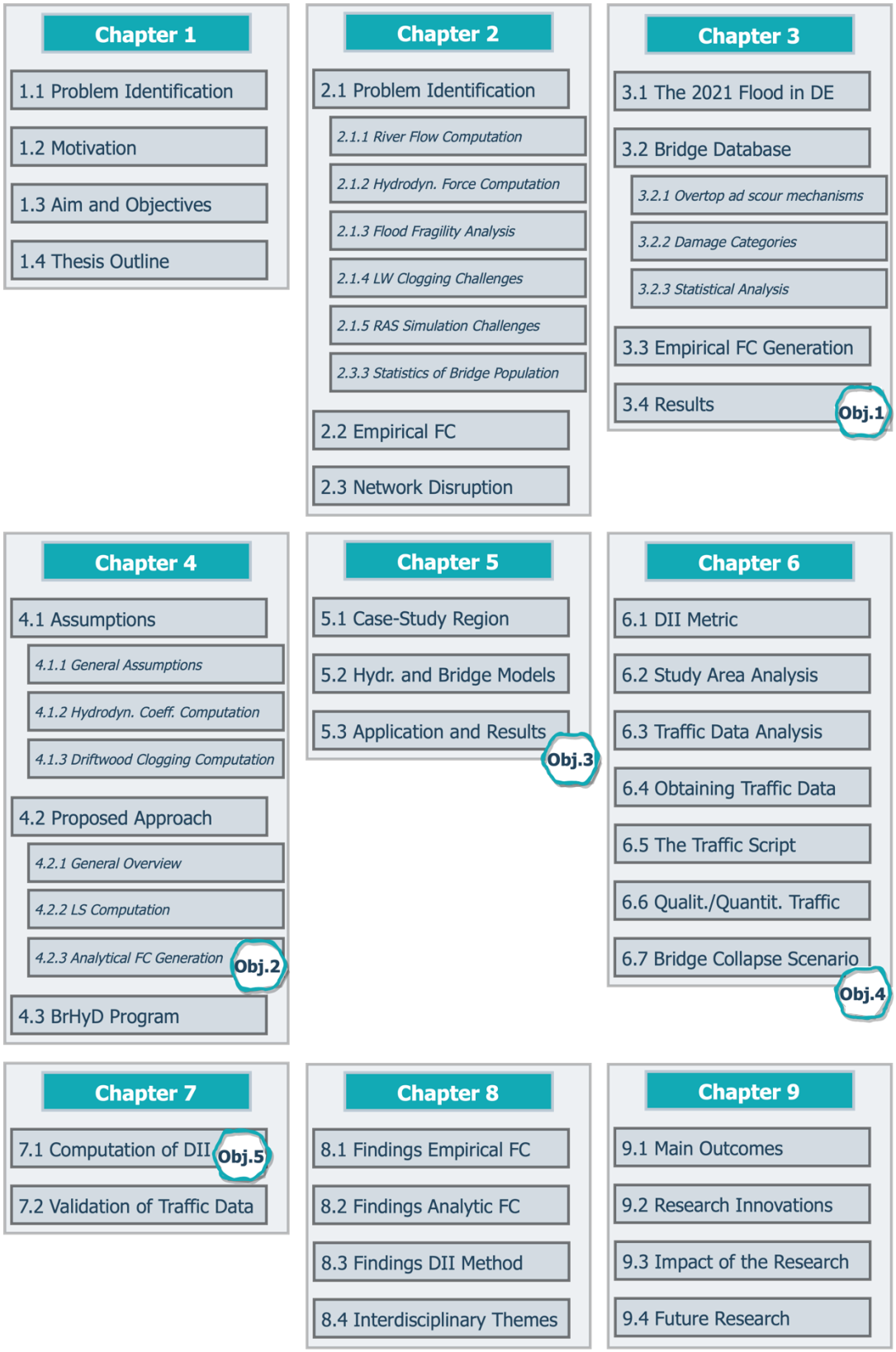


Figure 2. Outline of the Thesis. Paragraphs' titles have been modified to improve understanding

2. Literature Review

Civil infrastructure plays a crucial role both in crisis management and facilitating daily commuting for individuals (Wisetjindawat, Derrible and Kermanshah, 2018). Bridges serve as vital gateways for people and goods, even in the face of natural hazard events such as floods, earthquakes, and wildfires. Therefore, it is crucial to have a resilient and robust bridge network at the infrastructure level to prevent the isolation of communities in the event of disruptions (Han and Frangopol, 2022). Extensive research has been conducted on the vulnerability of bridges to hazardous events (Capacci, Biondini and Titi, 2020). The collapse of infrastructure not only affects businesses but also hampers rescue operations. Of particular concern is the connectivity between strategic buildings (e.g., hospitals, collective shelters) and rural settlements (Porta, Crucitti and Latora, 2006). In such areas, a failure in a road link can lead to the isolation of entire communities. This problem primarily arises from two factors: (i) inadequate maintenance of secondary infrastructure and (ii) a lack of network redundancy (Inkoom and Sobanjo, 2019). Consequently, the quantification of the vulnerability of secondary infrastructure becomes a significant challenge. As a result, bridge collapses, particularly those related to floods, have received considerable attention in research studies (Wardhana and Hadipriono, 2003; Proske, 2018; Zhang *et al.*, 2022). Furthermore, human-induced alterations in watersheds covered the effects of climate change, posing additional challenges in forecasting flood scenarios (Hodgkins *et al.*, 2017; Blöschl *et al.*, 2019; Bruno Merz *et al.*, 2022). While catastrophic floods often prompt risk-averse actions, leading to the adoption of prudent management strategies (Miao, 2019), these measures come at a substantial societal and economic cost (Merz *et al.*, 2021). Douben (2006) estimated that over 120 million people worldwide are impacted by floods annually, making it the most life-threatening natural hazard. The susceptibility of society to floods is significantly influenced by its ability to cope, closely tied to indicators of wealth. Global research on flood vulnerability has underscored that, at the current rate of climate change, disparities between low and high-income nations will grow (Duan *et al.*, 2022).

Regarding the European situation, according to data from Risklayer CATDAT, approximately 80% of economic losses resulting from natural hazards in Europe are attributed to climate-related events (EC, EEA, 2022). The regions with the highest economic damage per square kilometer are Switzerland (around 400 000 EUR/km^2), Germany, and Italy (around 300 000 EUR/km^2). Notably, Germany and Switzerland have insurance coverage for 37% of their losses, while Italy has insurance coverage for only 6%.

Transferring economic risk to insurance can prove cost-effective for accelerating the recovery phase (Wing *et al.*, 2020). Therefore, it is crucial to evaluate the economic risk faced by infrastructure owners when dealing with extreme events (Merz *et al.*, 2010).

Among infrastructure assets, bridges stand out as one of the most susceptible elements (Argyroudis *et al.*, 2019). Research efforts have focused on studying and systematizing failure scenarios for small bridges during extreme events like floods (Sassu, Giresini, and Puppio, 2017). However, the performance of bridges under varying flood scenarios is often unknown, as designs are typically based on deterministic approaches (Benedict and Knight, 2021). In contrast, fragility curves establish a connection between expected damage and a range of hazard intensities. Subsequently, through damage-loss equations, the financial aspect can be linked to the intensity of the hazard (Elmer *et al.*, 2010). Consequently, fragility curves represent a crucial tool for assessing the financial risk associated with structures (Li and Chen, 2023).

At asset level, fragility approaches characterise probabilities of failure of defined structural thresholds for a given magnitude of hazard intensity measure (Porter, 2007). The methods to develop such functions can be grouped in four categories: (i) analytical methods; (ii) empirical approaches; (iii) expert's judgement approaches; (iv) hybrid methods. Analytical methods employ mathematical design to replicate the behaviour of structures under hydraulic forcing, whereas empirical approaches profit inputs from past collapse events, such as damaged bridges in the aftermath of a floods. Subsequently, an expert judges the statistical significance of such data. Furthermore, engineers and analysts can derive fragility curves on the basis of existing information and process it through their judgement. In particular, weighted opinions from surveys can impact the conditional probability of damage relying on agreed pre-established questions intended to guarantee stability of the model (Eidsvig, 2021). Combining two or more of the described method is often employed to offset the absence of information; such approaches are called hybrid methods (Allen et al., 2021), i.e. one may employ an analytical method and subsequently refining the output through expert judgement. Usually, fragility analysis for floods implements an analytical method, as information consistency and the amount of participants in surveys hinders other approaches.

Current literature works on bridges' fragility curves for floods mainly employ analytical methods, which are often presented together with earthquake hazard (Sfahani, Guan and Loo, 2015; Guo, Badroddin and Chen, 2019; Argyroudis and Mitoulis, 2021). Vulnerability studies on bridges are developed for heritage structures to shade lights on flood risk mapping (Arrighi, Ballio and Simonelli, 2023). However, the availability of empirical fragilities is primarily confined to hurricane events due to the substantial number of damaged bridges and the resultant financial losses, which catch the interest of

stakeholders (Leal *et al.*, 2019; Webb and Cleary, 2019). Notably, studies that have examined flood fragility curves based on empirical data have predominantly focused on hurricane-related events (Padgett, Spiller, and Arnold, 2012; Anderson *et al.*, 2017; Balomenos, Kameshwar, and Padgett, 2020; Bruijn *et al.*, 2022). Hence, there is a lack on flood fragility curves based on actual failures for riverine bridges in mainland Europe. The necessity for empirical relationships stems from the accumulation of evidence derived from damaged bridges.

Furthermore, these findings can serve the purpose of validating and enhancing existing analytical models. Bridge owner records and post-disaster surveys enhance the quality of available data, especially when a flood event results in numerous damaged bridges, ensuring statistical robustness (Montalvo, Cook, and Keeney, 2020). Consequently, the database containing information about damaged bridges is systematically analysed to identify correlations between bridge characteristics and the type of damage. Nonetheless, mitigating the rate of bridge collapses presents a challenge to practitioners, as the causes and mechanisms often exhibit unique features associated with each structure and its location (Choudhury and Hasnat, 2015). Remarkably, statistical methods applied to a portfolio of collapsed bridges have indicated that factors such as age, design enhancements, and maintenance practices have not succeeded in reducing collapse rates during floods (Cook and Barr, 2017). Therefore, further research is needed to explain bridge failure mechanisms, including less-considered phenomena like hydraulic forcing and scenarios involving the blockage of bridges by driftwood (Pucci *et al.*, 2023a).

By examining hydrodynamic forces on the design of bridges, it is emphasized the chance for the deck clearance to be fully filled by flow discharges. This occurrence may be magnified by the accumulation of debris and floating logs, resulting in driftwood clogging. Examples of designing accounting for overtopping events can be found in Australia, where the Australian Standard 5100 prescribes checks against such occurrences (Committee BD-090, 2017).

More often, especially in Europe, bridges are not designed to sustain water thrust against decks, while it is only advised the designer to provide an adequate freeboard as for the design peak discharge (CEN, 2005a). This gap between the water surface and the girder soffit acts as a safety factor relatively to the uncertainty affecting the discharge. In the last decades, due to a combination of climatic changes and lack of maintenance, failures due to overtopping/dragging are increasingly reported (Oudenbroek *et al.*, 2018). This highlighted the need for further investigations to assess and prevent these failure mechanisms. Up to date, only the Australian Bridge Design Code AS5100 considers variable hydrodynamic coefficients, while Eurocode 1 and AASHTO use a constant value and only for drag, neglecting both uplift and overturning limit states (CEN, 2005a; AASTHO, 2012). In the case of Eurocode

1, such limit state is to be considered only during the construction phase. Despite such differences, all the mentioned standards define the action in a similar way, i.e. using coefficients to reproduce the effect of a dynamic action within a static framework. This is mainly due to the complexity behind hydrodynamic coefficients. Indeed, despite a clear theoretical background, hydrodynamic coefficients are not easy to determine, even with numerical simulations, due to the deck-flow interaction. Conversely, flume experiments allow to segregate variables and identify the influence of each parameter on pressure coefficients (Kerenyi, Sofu and Guo, 2009). Therefore, in this work results of experimental campaigns are employed to determine hydrodynamic coefficients at each water stage.

The other aspect to consider is the driftwood clogging. Large Wood (LW) normally indicates logs of wood with diameter ≥ 10 cm and length ≥ 1 m (Schalko and Weitbrecht, 2022). Floating LW, identified as driftwood is a crucial component for the ecosystem preservation of rivers. Furthermore, LW may threaten inline structures as weirs, bridges and dams. Hence, engineering and administrative actions are essential to mitigate the risk on constructions, though preserving a sustainable ecosystem of rivers. Within administrative actions, the subdivision of river's catchments into several hazard levels can be a cost-effective solution to implement early-warning systems (Schmocker and Weitbrecht, 2013). Recent approaches combine satellite imagery to quantify the clogging risk due to LW at bridges, including mitigation strategies (Panici and Kripakaran, 2023). Conventional engineering-based actions employ racks and nets to hold LW. However, also casings and movable bridges are efficient answers (Schalko *et al.*, 2020). A comprehensive discussion on LW impacts and mitigation measures on the ecosystem of rivers is included within the work of Schalko and Weitbrecht (2022). At structural level, LW accumulation at piers is significantly predominant for backwater rise and scour (Schalko *et al.*, 2019). On single span bridges, the build-up of LW happens at deck level; to this end, in laboratory studies, researchers usually attach to the setup a spanwise log carpet, or leave the chance for an arbitrary clogging (Gschnitzer *et al.*, 2017; Oudenbroek *et al.*, 2018). The first approach is employed to define the amplified hydraulic forcing on the deck, while the second is used to compute the likelihood of a log to be blocked. In this work, both approaches are accounted, using outcomes of flume tests to compute the blocking probability (Schmocker and Hager, 2011; Gschnitzer *et al.*, 2017). Then, the amplified hydraulic thrust at the deck is mathematically modelled using log mats as a worst-case scenario, overlooking porosity due to restrictions in the software used. Hence, this study considers forces not entirely described in current standards and displays how those overlooked limit states may influence the single-span bridges' probability of failure. To this end, fragility curves are used to measure the safety level of the bridge. The following Paragraph describes the mentioned aspects providing additional insights on each one.

2.1. Problem Identification

Numerous recent studies – as indicated in Table 1 – combine flood hazard with others as tsunamis, earthquakes and effects of long-term processes such as corrosion (Li *et al.*, 2020). Despite the impact of hydraulic actions damage - for instance - the seismic performance of bridges, latest findings show the significance of a dedicated hydraulic model (Argyroudis *et al.*, 2019). Actually, Argyroudis and Mitoulis, (2021) indicate that a river hydraulic model is still missing within a multi-hazard fragility analysis, despite the attention given to account for hydraulic forcing (Argyroudis and Mitoulis, 2021). The scale of such actions may impact bridges with consequences comparable to those produced by minor earthquakes (Li *et al.*, 2020), but such forces are triggered due to the river-bridge interaction (Dong and Frangopol, 2016). Although basic flood-bridge simulations lower the computational cost, they are not able to reproduce the specific river behaviour upstream and downstream the bridge (Khandel and Soliman, 2021). Therefore, it is required to elaborate impact models accounting the flood-bridge interaction, which is capable to consider a higher level of detail at reasonable costs of computing (D'Angelo *et al.*, 2022).

Table 1. Multi-hazard studies including flood fragility

Authors	Flood Hazard	Number of Flood Discharges	Hydrodynamic Forces	River hydraulic model
(Banerjee and Ganesh Prasad, 2013)	Flood prior to seismic hazard	5	No	No
(Pang *et al.*, 2014)	Flood prior to seismic hazard	3	AASHTO	No
(Yilmaz, Banerjee and Johnson, 2016)	Flood prior to seismic hazard	6 (only 4 with different magnitude)	No	No
(Dong and Frangopol, 2016)	Separately for vulnerability	3	AASHTO	No
(Gehl and D'Ayala, 2018)	Flood prior to seismic hazard	3	No	No
(Yilmaz, Banerjee and Johnson, 2018)	Flood prior to seismic hazard	4 (upper boundary to 20-year return period)	No	No
(Argyroudis *et al.*, 2019)	Flood prior to seismic hazard	–	No	No
(Li *et al.*, 2020)	Floods only theoretically discussed	2 + linear interpolation	AASHTO	No
(Argyroudis and Mitoulis, 2021)	Flood prior to seismic hazard	Multiple values	Eurocode 1991-1-6	No

2.1.1. River Flow Computation

A key problem in the design of structures on rivers is to assess the magnitude of the flow discharge. In situations where rivers are not gauged, rainfall-based methods are widely employed to estimate discharges. Among these approaches, regional ones provide a simple and cost-effective way to determine river flow (Van Campenhout *et al.*, 2020). However, their applicability is limited to those areas and countries – e.g. the US – that adopted this strategy to provide practitioners with such ready tools (Yilmaz, Banerjee and Johnson, 2016). When the discharge return period is assumed to be the same as the rainfall one, it may lead to oversimplification and increased uncertainties in expected discharges (Gehl and D'Ayala, 2018), mainly due to neglecting the AMC (Antecedent Moisture Condition) of the soil at catchment scale. Conversely, gauged rivers present challenges related to the length of available hydrometric time series and the potential influence of a dam or weir near the bridge, which may impose an upper boundary on flow values (Yilmaz, Banerjee and Johnson, 2018). Another factor contributing to potential errors is the likelihood of water overtopping embankments, which can lead to a reduction in the measured peak discharge. Recent approaches aim to establish connections between precipitation and temperature data to a limited number of measured discharges by utilizing Artificial Neural Networks or downscaling General Circulation Models (GCMs) (Khandel and Soliman, 2021).

In addition to these approaches, advancements have been made in the field of hydrological modelling by incorporating remote sensing data, such as satellite imagery and radar data. Remote sensing techniques can provide valuable information for estimating flow discharge, including rainfall distribution, land cover characteristics, and topographic features (Gleason and Durand, 2020; Yoon, Marshall and Sharma, 2023). The integration of remote sensing data with hydrological models has the potential to improve the accuracy of discharge estimation, especially in ungauged or poorly gauged regions.

Furthermore, the use of AI ensemble modelling approaches has gained attention in recent years. The models combine multiple hydrological models or multiple realizations of the same model to account for uncertainties and improve the reliability of predictions (Zounemat-Kermani *et al.*, 2021). By considering different sources of uncertainty, such as model structure, parameterization, and input data, ensemble modelling provides a more comprehensive assessment of discharge estimation.

Commonly, predictions made through ensemble modelling can be categorised into three main groups: (i) statistics-based (including Artificial Neural Network ones); (ii) ensemble flow prediction ; (iii) numerical weather-based prediction. In such context, the availability of historic data poses a major concern to the prediction accuracy of such models (Troin *et al.*, 2021).

In present applications, distributed hydrological models outstand other methods in terms of cost-effectiveness, namely enhanced efficiency and practical usefulness, as numerous local authorities have adopted them for discharge calculations (Spyrou *et al.*, 2020). Certainly, distributed Hydrological Models offer numerous advantages for flood hazard characterization, potentially reducing computational expenses compared to downscaling GCMs or training an Artificial Neural Network (ANN). These benefits include higher spatial resolution in geodata, fewer analyses required for parameters' variability, and the ability to generate prompt and readable GIS maps as outputs (Bizhanimanzar, Leconte and Nuth, 2020).

2.1.2. Hydrodynamic Forces Comparison. Focus on Drag Coefficient

Traditionally, the hydraulic action on a structure can be decomposed into a dynamic and a static component (Hamill, 1998). Due to the geometry of girders, which is typically not streamlined, a bridge deck behaves as a bluff body even if partially submerged. Because of the contact between a fluid and a solid object, usually flow separation arises for certain body geometries, as in the case of bridge decks; this occurrence produces a wake (disturbed flow) and consequently a gradient of pressure occurs between the upstream and downstream side of the girder. The drag force is the pressure component acting parallel to the direction of the river flow, whereas the normal one is termed lift. Both forces change for different girder submersion grades, and therefore an overturning moment appears if the deck's barycentre is taken as reference point within a conventional free-body scheme.

The assessment of hydrodynamic actions on decks is traditionally investigated employing flume-scale tests on bridge models. Especially, the type of girder that is responsible for varying the pressure gradient, affects the magnitude of exerted forces. Furthermore, also the Froude number and the bridge clearance are deemed to influence the hydrodynamic thrust (Oudenbroek *et al.*, 2018). Additionally, in case of multi-span bridges, piers increase the area occupied by structural elements, inducing a localized acceleration of the flow, which generates a higher pressure drop and hence a greater dynamic thrust. Despite the extensive studies on piers (Jempson, 2000), in the two last decades isolated deck behaviour was increasingly investigated. Several research groups studied deck performance under various hydraulic conditions, whose applicability on real-world cases can be directly addressed on single span bridges with minimum contraction and expansion. From these experiments, several key factors have been identified to characterize the partially and fully inundated decks. In particular, the inundation ratio h^* - as per

Equation (1) – was the first parameter reported to have a significant effect on hydrodynamic actions (Malavasi and Guadagnini, 2003).

$$h^* = (h_u - h_b)/s \tag{1}$$

Where h_u is the upstream water height, s the deck thickness and h_b bridge clearance, as shown in Figure 3.

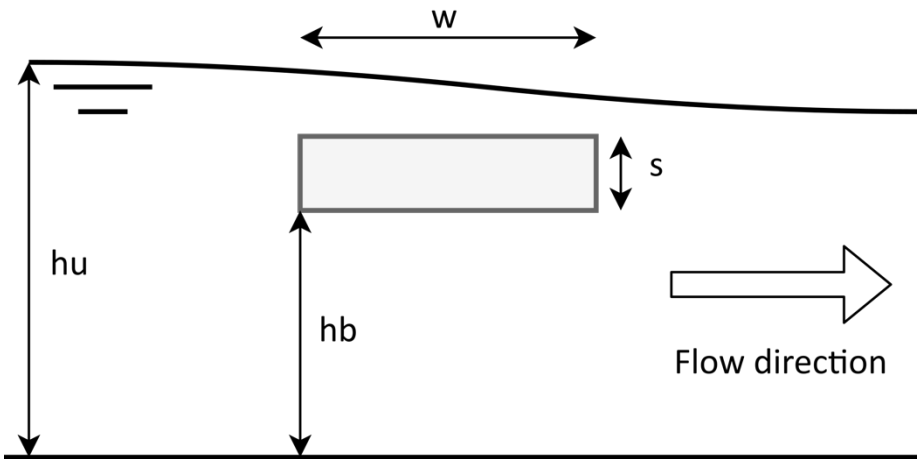


Figure 3. Bridge Deck schematic cross-section and geometric parameters

Indeed, before 2004, none of well-established standards as Eurocode, AASHTO and Australian Standard included the influence of inundation ratio to determine hydrodynamic coefficients. Up to date, only the Australian Bridge Design Code (Committee BD-090, 2017) considers the inundation ratio (among others) to compute hydrodynamic loads, although all the mentioned standards define the action in a similar way, i.e. using coefficients to reproduce the effect of a dynamic action within a static framework. From the theory of bluff bodies in a moving fluid, the drag coefficient C_D can be defined as the ratio of the drag force to the dynamic thrust produced on the projected body area normal to the direction of the flow A, such as:

$$C_D = F_D/0.5\rho_w V_u^2 A \tag{2}$$

Equation (2) provides the numerical representation of this definition, in which ρ is the fluid density, V_u is the approach velocity and F_D is the drag force, which accounts for both pressure and viscous drag. Despite a clear theoretical background, drag coefficients are not easy to determine, even with numerical simulations, due to the complexity of the deck-flow interaction (Basile *et al.*, 2019). Conversely, flume experiments allow to segregate variables and identify the influence of each parameter

on pressure coefficients. In this Chapter, the results of several hydrodynamic tests from literature are analysed to determine practical criteria and boundary conditions for the computation of the drag coefficient. Furthermore, given that a general overview and evaluation of all contributions was missing, this is a comparison of the most important flume experiments of the last two decades, clustered with respect to geometric boundary conditions and to flow regimes. This work focuses on drag coefficient only, as it is intended to demonstrate the most influencing factors on a component of flow's dynamic thrust.

Therefore, the results of seven different experimental campaigns are analysed (Jempson, 2000; Malavasi and Guadagnini, 2003, 2007; Kerenyi, Sofu and Guo, 2009; Oudenbroek *et al.*, 2018; Dráb *et al.*, 2019; Dean, 2020). Bridge models tested included steel and prestressed concrete I-beam girders, spread and adjacent box beam girders, slab deck with and without railings. It should be mentioned that load cell values of drag force are evaluated by using different formulations while the deck was partially submerged. In particular, Malavasi and Guadagnini used the entire deck thickness instead of the actual wetted part for $h^* < 1$ (Malavasi and Guadagnini 2003, 2007). By contrast, all the others research groups considered the deck's wetted area in partial submersion scenario. The slenderness in the direction of the flow, called w/s where w is the deck width and s its overall thickness ranged from 3 to 17.1. In some cases, the railing is included as part of s, especially in case of solid crash barriers, significantly decreasing the w/s ratio. The measured drag coefficient C_D ranged between –0.2 to 3.05, inundation ratio h^* between 0.2 to 4.05, while Froude number Fr ranged between 0.1 to 0.5. In all flume experiments, the Reynolds number was maintained at around 10^4, which corresponds to $10^5 - 10^6$ on real-world situations, to guarantee the turbulent flow condition.

In this study, the effect of the following parameters on the magnitude of C_D was investigated:

1. Inundation Ratio – h^*
2. Proximity Ratio – P_R
3. Blockage Ratio – B_R

In addition, the deck's width to thickness ratio – w/s is summarised for the examined studies.

2.1.2.1. Inundation Ratio

The submergence level of the bridge normalized with respect to the deck thickness is the main parameter on which flume experiments showed the variability of C_D across different hydraulic conditions. All the tests evidenced a prominent role of h^* for the whole range of flow, heights, and velocities. Figure 4 shows the function $C_D = f(h^*)$ for $h^* \leq 4.05$. This maximum value might be unrealistic in actual

floods, because even for h^* around 2 (or even less), the bridge failure can be preceded by a scour-triggered mechanism, as in the case of embankment collapse. Indeed, the maximum value of h^* is chosen to better interpolate the results obtained at lower inundation ratios.

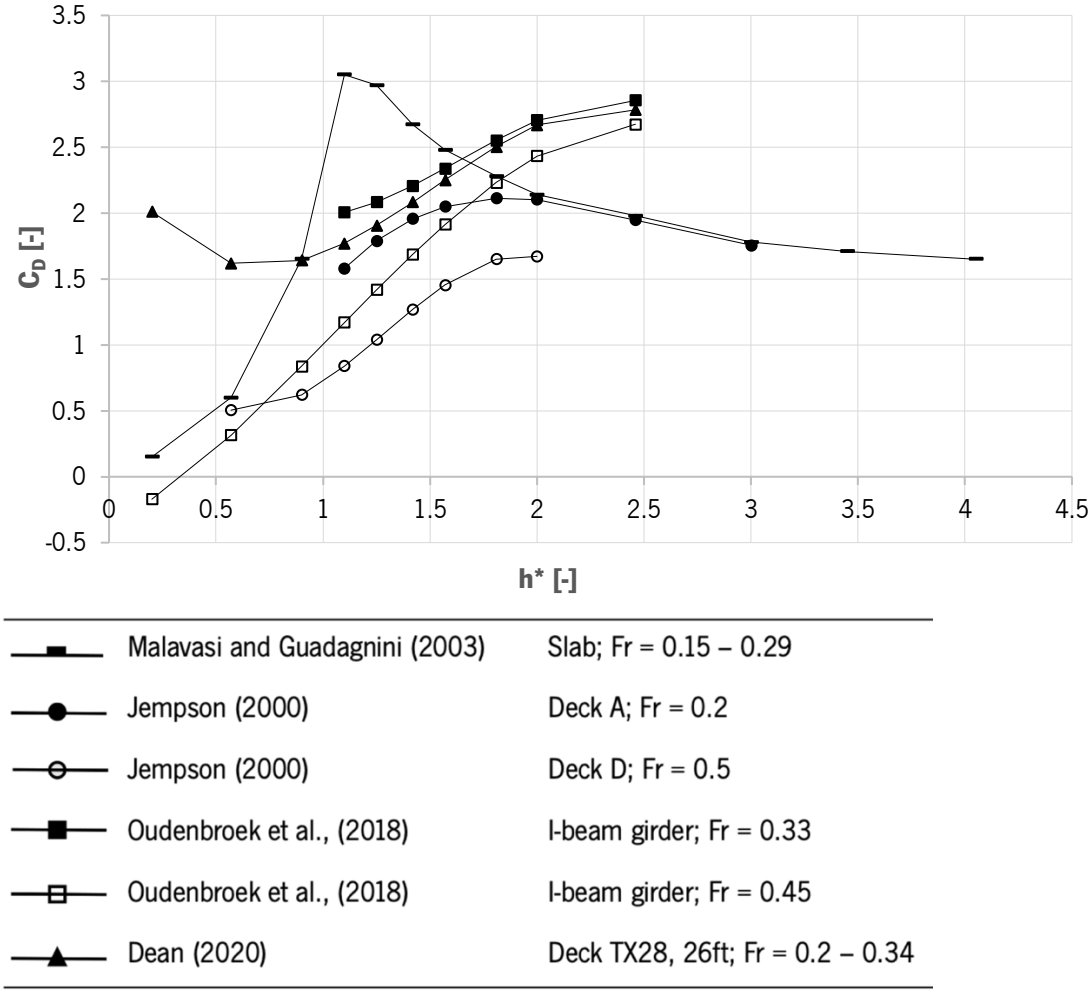


Figure 4. Drag Coefficient (C_D) as a function of Inundation Ratio (h^*) for different experiments

From the graph of Figure 4, irrespective of h^*, several other parameters are influencing the drag coefficient. Comparing the results obtained from each research contribution, like the two series of Oudenbroek *et al.* (2018) in Figure 4, and extending the evaluation between different authors, it is clear the influence of the Froude number on the amount of drag developed by the deck-flow interaction. In particular, for lower Froude numbers, higher C_D values are found. A significantly different behaviour is evidenced at $h^* > 1.5 - 2$, in which only the results of Jempson (2000) and Malavasi and Guadagnini (2007) show a decreasing trend in C_D values. Indeed, the behavior of the deck, in particular the one tested by Malavasi and Guadagnini (2003, 2007), for greater inundation ratios tends to the theoretical result obtained by a rectangular cylinder in an unbounded domain. Indeed, the existence of a free surface and of a channel floor originates asymmetric boundary conditions, causing deviations from the

corresponding unbounded test. The deviations observed in Jempson (2000) and Malavasi and Guadagnini (2003, 2007) at high inundation ratios can be attributed at last to the shape of the railing, as its presence is the cause of profiles' changes on the free surface, observed using PIV techniques by Cheng and Ming-Jer (2014). Hence, the shape and height of the railing might be the cause for an increasing drag force at higher inundation ratios. The asymmetry in the flow behaviour due to the free surface and the channel floor can be investigated using additional dimensionless parameters: the proximity ratio, the blockage ratio and the width/thickness ratio, described in the following Paragraphs.

2.1.2.2. Proximity Ratio

The proximity ratio can be defined as the distance between the riverbed and the girder soffit h_b normalized to the deck's thickness s, as indicated by the following equation:

$$P_R = h_b/s \tag{3}$$

The variability of P_R in the analysed flume tests ranged between 2.3 and 7.2. In Figure 4, two studies (Kerenyi *et al.*, 2009; Dráb *et al.*, 2019) were deliberately omitted, as their $C_D = f(h^*)$ was obtained by varying h_b instead of h_u. For the sake of completeness, the experiment performed by Dráb *et al.* (2019) involved the variation of both h_b and h_u. However, only three levels of proximity were investigated (4.7, 6.5, 7.2). Conversely, the flume tests performed by Kerenyi *et al.* (2009) assessed the variation of h^* by varying only h_b. This is a key-point for the comparability of the research performed by Kerenyi *et al.* (2009) with the others. Indeed, within the existing literature similar comparisons are available, but their interpretation shall be accurately performed, as erroneous conclusions can be drawn. The issue arises because, when the Kerenyi's study is considered, only one point at time can be plotted using the $C_D = f(h^*)$. On the other side, all the other investigations use a constant proximity ratio, whereas in Kerenyi *et al.* (2009), h^* varies with P_R, as shown in Figure 5.

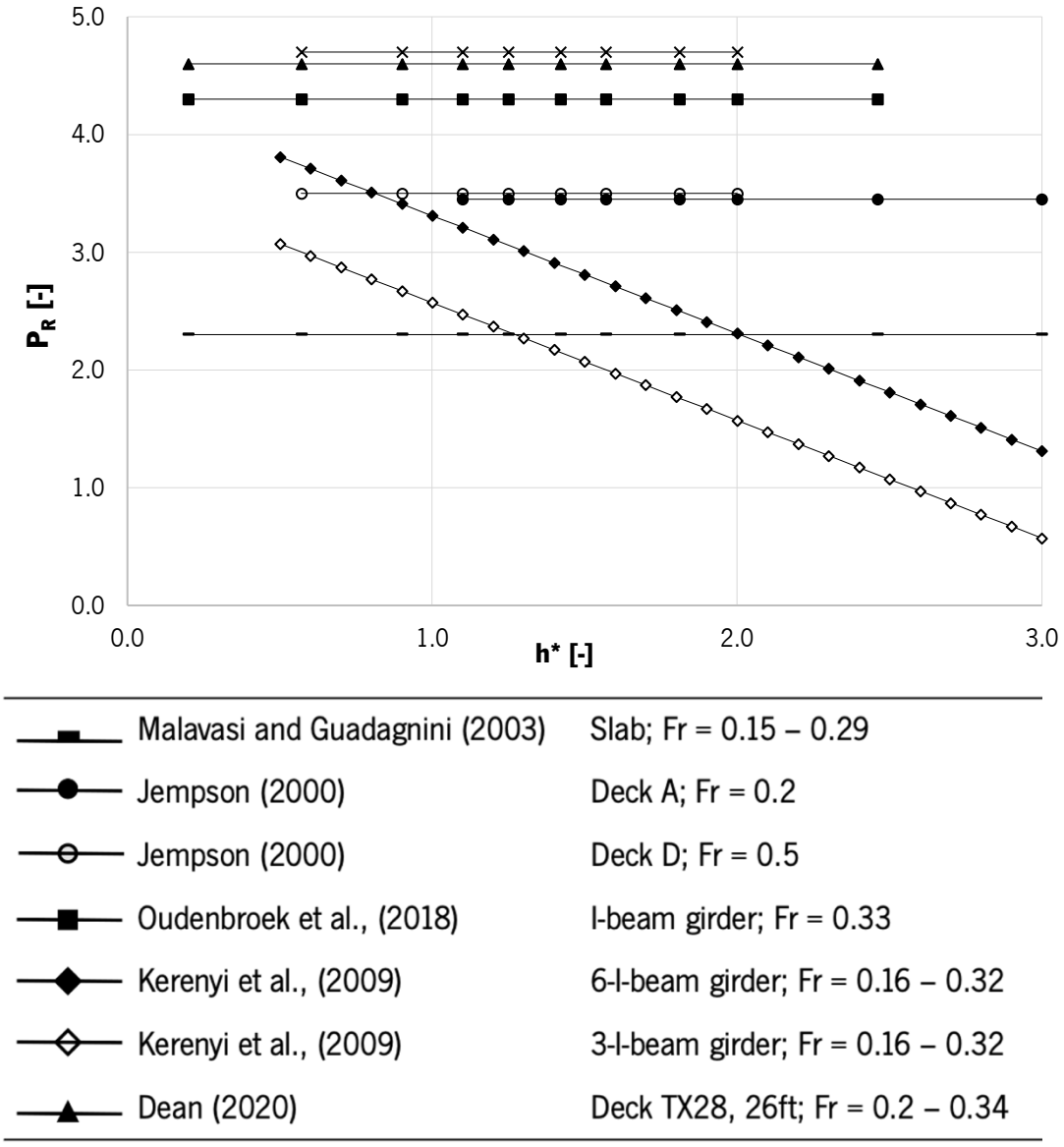


Figure 5. Proximity Ratio (P_R) as a function of Inundation Ratio (h^*) limited to $h^* = 3$

Indeed, this might be the rationale for the interpretation described in Oudenbroek *et al.* (2018), in which the higher values of C_D obtained at low h^* by Kerenyi *et al.* (2009) are wrongly attributed to the influence of P_R. On the contrary, at lower inundation ratios, h_b achieves its maximum for the setup of Kerenyi *et al.* (2009) and hence, the higher drag can be attributed to the interaction with the free surface. Certainly, the graph in Figure 6 shows an increase of C_D for high P_R values and one can think of a correlation between the two phenomena. However, this phenomenon is not evidenced in the other analysed experiments, but only in the flume tests performed by Kerenyi *et al.* (2009). Conversely, the effect of P_R on C_D can be clearly seen looking at the research of Jempson (2000) and confirmed by Malavasi and Guadagnini, (2005), in which C_D is decreasing as P_R increases, for the entire range of inundation ratios (Malavasi and Guadagnini, 2005). Hence, this is an evidence that the drag coefficient

achieves higher values for low proximities due to the interaction with the riverbed. However, this is endorsed also by Oudenbroek *et al.* (2018) and can be additionally justified from a theoretical point of view, by using the Momentum Theorem on a control-volume of fluid, where higher is the friction, greater is the drag. Then, it is straightforward to confirm that care should be taken when comparing the same graph, such as $C_D = f(h^*)$ and $C_D = f(P_R)$ obtained with different experimental approaches.

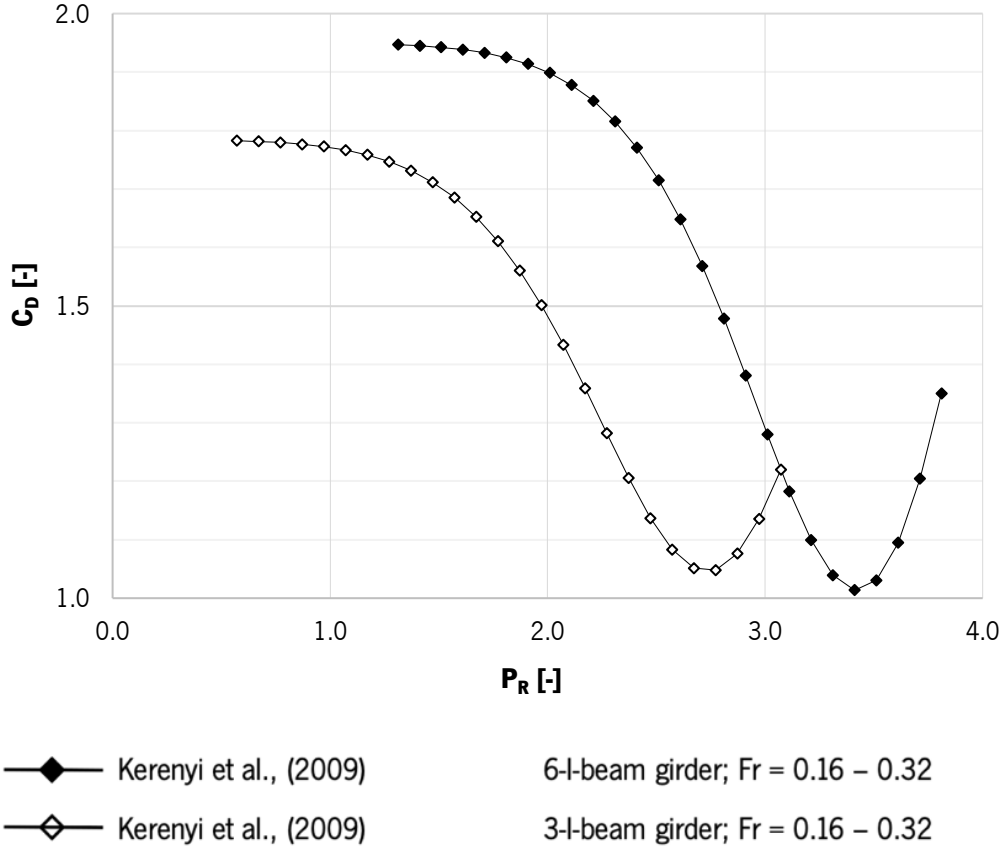


Figure 6. Drag coefficient (C_D) as a function of Proximity Ratio (P_R) for the setups of Kerenyi et al. (2009)

Thus, it can be concluded that P_R has a significant effect on C_D not only for lower inundation ratios, but for the whole range of tested h^*. Therefore, from a designer's point of view, given that C_D is higher for lower P_R, small bridges that are usually closer to riverbeds, might be subjected to a higher drag coefficient than long span ones located on wide and therefore generally deeper rivers. Nevertheless, this is not sufficient to deduce that small bridges are subjected to a higher drag force because of the P_R's influence. Indeed, another parameter should be considered, namely the blockage ratio.

2.1.2.3. Blockage Ratio

The blockage ratio can be defined as the ratio between the wetted depth of the deck s_{wet} to the upstream water height h_u, as indicated by Equation (4).

$$\mathrm{B_R} = s_{wet}/h_u \tag{4}$$

The influence of B_R on C_D observed in the flume experiments pointed out the existence of a strong rise of the drag force with increasing blockage. It has been also highlighted a lower bound for B_R under which C_D does not vary (Malavasi and Guadagnini, 2007; Chu *et al.*, 2016). Below $B_R = 0.14$, C_D approximates to a constant value, which depends just on h^* and P_R. Moving one step further from past works and plotting the relationships between h^*, P_R and B_R two distinguished domains can be highlighted and are shown in Figure 7, in which the function $B_R = f(h^*, P_R)$ is represented together with the $B_R = 0.14$ plane.

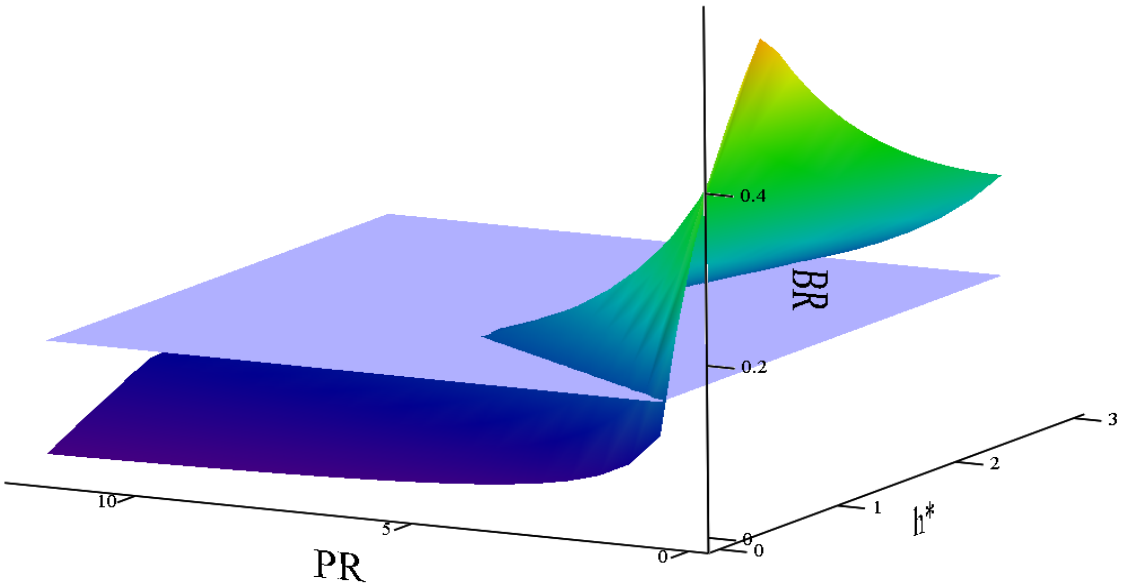


Figure 7. Blockage Ratio (B_R) as a function of Inundation Ratio (h^*) and Proximity Ratio (P_R) and the plane $B_R = 0.14$

Through the observation of the chart in Figure 7, it can be highlighted that only for high P_R values, the influence of B_R on C_D is negligible for the entire range of h^*. This can be understood by recalling the information of a nearly constant value for C_D in the range $B_R \leq 0.14$. Hence, it is desirable to have a bridge located in the part of the domain that is not influenced by B_R. Simple charts as the one in Figure 8, can aid the designer to avoid the B_R influence.

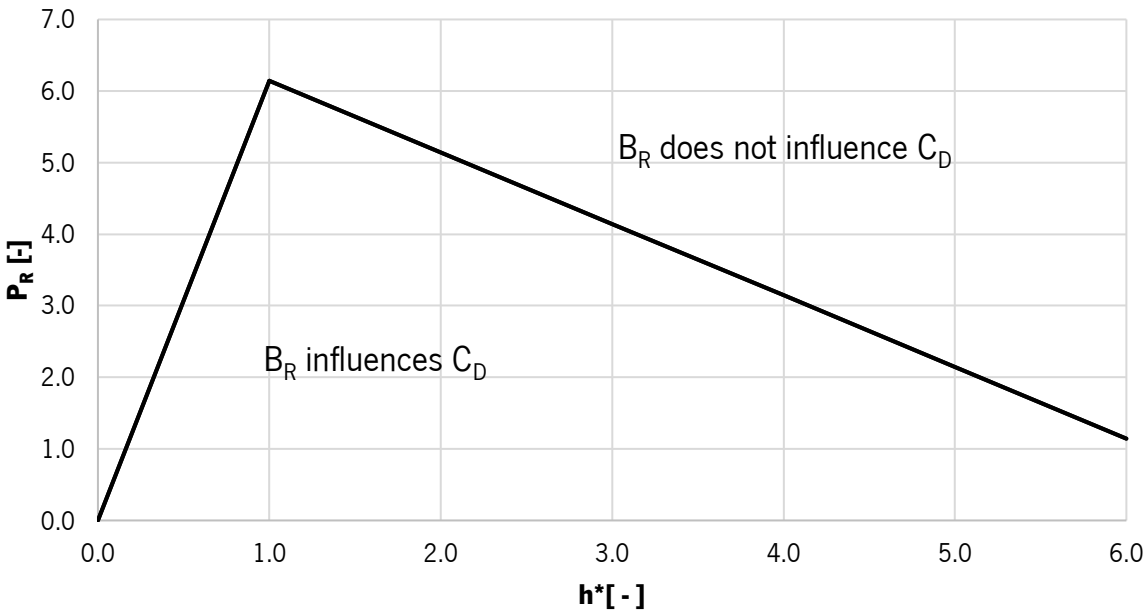


Figure 8. Influence domain of B_R on C_D. Each point in the graph represents a possible deck's position, given by P_R, and maximum water elevation through h_u within h^*. For points under the curve, it is known that B_R has a great influence on C_D, and therefore higher drag values are expected when compared to situations above the domain's lines

In particular, entering in the diagram of Figure 8 on the vertical axis by knowing the bridge clearance to the riverbed, the critical situations under which B_R causes an increase of C_D can be recognized. Then, in the design phase one can think of moving up the deck by entering in the non-influence zone shown in Figure 8. Alternatively, a change in structural system or material can be chosen, reducing the thickness s to shift the deck position on the non-influence zone and thus avoiding greater drag actions. However, by doing so, most probably the deck's weight will be reduced, and the influence of lift actions might become predominant on drag's one. In any case, the stability of the deck must be assessed through analytic approaches, as per Chapter 4.2.2.

Moreover, the proposed chart of Figure 8 can be used with great practical utility during the safety assessment of bridge decks. In such situations, each asset configuration can be placed on the diagram of Figure 8 by knowing only P_R and hypothesizing h^* based on past floods and engineering expertise. Thus, it can be understood if great drag actions are to be expected based on just a few geometric parameters.

The subsequent question concerns the influence of B_R on C_D, in those cases in which it is not negligible. Two different experiments led to the same results: for a constant inundation ratio, moving vertical on the B_R–influenced domain, the growth of C_D is exponential, as can be seen from Figure 9.

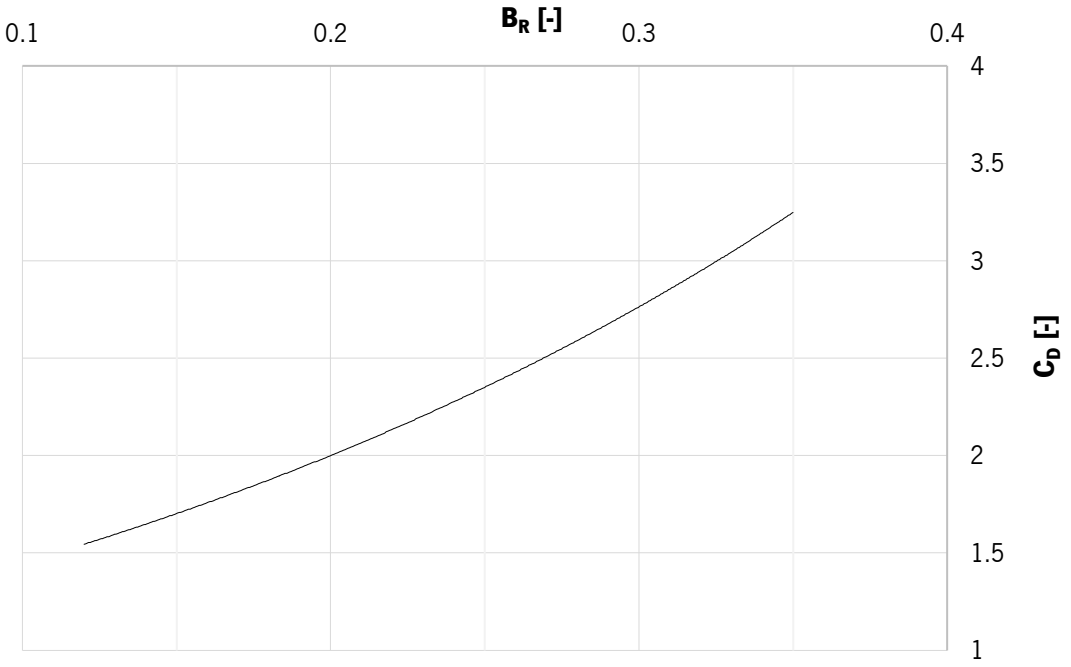


Figure 9. Variation of Drag Coefficient (C_D) as a function of Blockage Ratio (B_R) for h = 2 and Proximity Ratio P_R = 2.3. Adapted from Malavasi and Guadagnini, (2007)*

Through the observation of the chart of Figure 9, it can be also highlighted that for a submerged rectangular cylinder having low values of blockage ratio, C_D approximates to the theoretical value of drag in a symmetric domain. However, this situation is also strongly dependent on the proximity ratio, that accounts for the bottom boundary. In practical applications, $P_R > 1.5$, since a culvert instead of a bridge is usually chosen for smaller openings ($P_R < 1.5$). Nevertheless, the combination of low proximities (< 5) and thick decks, place short span bridges inside the blockage-influenced domain shown in Figure 8. This confirms that a greater C_D caused by low P_R is mainly influenced by B_R. This is principally due to an increased pressure gradient on the two surfaces of the deck normal to the flow. From a theoretical point of view, higher pressure drops lead to higher drag, in accordance with Equation (2). It is noteworthy to underline a slightly different result obtained by Oudenbroek *et al.* (2018); they found much milder C_D in case of increasing blockages if the local upstream velocity is chosen instead of the undisturbed upstream one. A key-issue in the use of the local velocity is that it is strongly influenced by interaction phenomena due to the proximity to the deck, as pointed out by (Picek *et al.*, 2007) and (Chu *et al.*, 2016). Indeed, not only the flow velocity changes, but also the water height, implying a change of both h^* and B_R. Furthermore, it is theoretically justified to consider the velocity of the flow away from the contraction caused by the bridge (Hamill, 1998). On the other side, developments on CFD simulations allow for more refined hydrodynamic analysis (Al-Hashimi, Al-Osmy and Mulahasan, 2020), while more recently, CFD

models have been successfully applied to include driftwood behaviour (Kimura, Kang and Kato, 2021). Then, considering only a CFD without floating logs, it could be possible that B_R measured with local velocities has a milder influence on C_D, but also the measured inundation ratio should be accordingly changed. Hence, two different blockages that account for different phenomena in terms of water height, pressure drop, and free-surface effects are considered, one from CFD and the other from flume experiments. Therefore, attention should be paid when such comparisons are performed, because an experimental validation on the use of local velocities for the computation of drag coefficients is still missing. Moreover, adopting another approach, though more accurate, precludes any comparison with previous works. Hence, this milder influence of B_R on C_D is pointed out as a possible effect, but is not considered here, as this result was obtained only numerically, and this critical literature review focused on flume experiments.

2.1.2.4. Bridge Deck and Shape

The bridge models tested in flume experiments significantly vary in the width to thickness ratio, w/s. The girder types are also rather different in the considered literature papers. Several authors also tested very peculiar girders, as the streamlined one in Kerenyi *et al.* (2009), which is designed to reduce hydrodynamic forces, or the truss bridge (Model E) and box beam (Model F) shown in the work of Jempson (2000). Although these specific shapes provide a valuable contribution to the investigation of complex hydrodynamic interactions, they are disregarded due to the low comparability with other works. A summary of girders type and w/s ratios is shown in Table 2.

From the analysis of flume tests, it is evidenced the greater drag for larger decks. This comparison could be performed only with similar P_R and B_R, to independently study the effect of the bridge width on C_D. In addition, from the comparison of I-girder and box/slab decks, the influence of the girder soffit may be responsible for the lower C_D values in the range $0.2 < h^* < 1$. This can be explained by the cavities between the I-beams, as observed in the work of Lin *et al.* (2012).

Table 2. w/s comparison among the investigated studies

Authors	**w/s**	**Deck Type**
Jempson (2000)	4.0	4 girders I-beam (Type A)
Jempson (2000)	4.6	Box Beam (Type D)
Malavasi and Guadagnini (2003)	3.0	Rectangular Cylinder
Kerenyi *et al. (*2009)	3.7	3 girders I-beam
Kerenyi *et al. (*2009)	4.5	6 girders I-beam
Oudenbroek *et al. (*2018)	4.7	3 girders T-beam
Dráb *et al.* (2019)	11.9	Rectangular Cylinder (A)
Dean (2020)	4.6 / 3.7	TX28/54 – 26' / 46' 4 girders I-beam
Dean (2020)	6.5 / 8.0	TX28/54 – 26' / 46' 6 girders I-beam
Dean (2020)	9.7 / 17.1	26' / 46' slab with railings

The most marked observation to emerge from the data comparison is the key-role and interdependence between h^*, P_R, B_R within the assessment of C_D. Although a higher drag coefficient does not directly correlate to a more vulnerable bridge due to lift and moment effects that are not considered, a final discussion can be drawn on the difference of drag between short and long span decks. A remarkable result is the strong influence of the blockage effect and the existence of an influence domain in which an exponential increase of drag coefficient is associated to a linear increase of blockage, being this exacerbated if a low proximity occurs. Hence, the risk associated to a greater C_D is mainly triggered by high blockage ratios and low proximities. Considering a 10% increase of B_R (when in the range of 0.2 – 0.3) it leads to a 75% rise of drag action on the deck. This situation may occur for short span bridges, located on secondary rivers, in which P_R is around 2 and B_R in the range 0.2 ÷ 0.3. The frequency of such situations is triggered on the structural side by increasing traffic loads and budget constraints (i.e., thicker – often precast – girders) and on the hydraulic side from climate change effects which increase extreme events. In addition, large uncertainties affect water stages due to river cross-section topography (Chen and Liu, 2017). In the case of new structures, an appropriate CFD analysis can be justified on long span bridges, but not in case of short span ones, due to budgetary reasons. Therefore, designers should rely on standards to account for hydrodynamic actions. On this matter, codes as the AASHTO Bridge Design Specifications, the Eurocode 1 (EN1991:2005) and the Australian Standards (AS5100) offer significantly different procedures (CEN, 2005a; AASTHO, 2012; Committee BD-090, 2017). Although all of them differentiate C_D based on the deck shape, only the AS5100 provides the designer insight into

inundation and proximity ratio, while the AASHTO and EN1991-1-6 use a constant drag for all hydraulic conditions and only during the construction phase (only for EN1991-1-6). Although this can be somehow conservative by neglecting lift forces as in the case of Eurocode, such approach can also be controversial, because it does not account for the downward lift effect on foundations and overturning moment on the deck. This implies that existing codes should benefit more from the variety of results from literature.

For the mentioned studies, in case of uplift, there is a generalised agreement on its relevance for structures at risk of overtopping and for lightweight decks. Nevertheless, such comparison can be made if flume experiments will include setups able to measure the deck's weight influence for various materials. To shed light on this point, the analysis of past collapses plays a key-role, as seen in Chapter 3.

2.1.3. Analysis of Flood Fragility

As seen in § 2.1.2, flume tests are commonly used to establish the magnitude of dynamic actions on decks by recording readings from sensors on a pre-established timeframe (e.g. 50 s) and subsequently averaging the results (Dráb *et al.*, 2019). Interestingly, in certain scenarios, lower discharges may result in greater thrusts on structural elements, because the increment of a dynamic action as drag does not progress monotonically alongside the water elevation (Oudenbroek *et al.*, 2018). Consequently, simulations that use incremental water rise are a better candidate for a probabilistic study. Indeed, this method permits calculating the safety of the structure at each water stage and not only at the peak level. Such approach has not applied to decks yet, because in former works that adopted this method, the highest water stage is maintained beneath the level of the bridge deck (Argyroudis *et al.*, 2020). A collection of works on fragility curves due to floods is given in Table 3. It must be mentioned that the blocking probability due to driftwood is not accounted in any of the works within this table.

It should not be neglected that floods typically transport floating debris and material. Indeed, drifting wood logs at the time of the impact against bridges can accumulate at the deck or at piers, producing a backwater rise – once entrapped – and generating also a larger blockage area in the direction normal to the flow one (Ruiz-Villanueva *et al.*, 2017). When combined, these effects cause complex hydraulic actions that must be accurately included in a vulnerability analysis.

Table 3. Works on fragility curves for flood events

Authors	Intensity Measure	Number of Flood Discharges	Hydrodynamic Forces	River hydraulic model
(Kim *et al.*, 2017)	Velocity	1	AASHTO	No
(Tubaldi, Macorini and Izzuddin, 2017)	Scour depth	6	No	No
(Kalendher *et al.*, 2018)	Velocity	100 from Weibull distribution	AS 5100	No
(Lam *et al.*, 2018)	Discharge	100 from 500 year rainfall	No	No
(Mondoro and Frangopol, 2018)	–	3 normal distributions	FHWA	No
(Tanasić and Hajdin, 2018)	Soil cover height	200 year return period	No	No
(Lamb *et al.*, 2019)	Discharge	100 from Weibull distribution	No	No
(Khandel and Soliman, 2021)	Discharge	ANN fitted on historical data	FEMA	No
(Ahamed, Duan and Jo, 2021)	Discharge and scour depth	7	AASHTO	HEC–RAS
(Anisha *et al.*, 2022)	Velocity	5	AS 5100	No

2.1.4. Large Wood Clogging Challenges at Modelling Stage

In this analysis, Large Wood (LW) are studied owing to the effect of damming, which may result in bridge failure. The issue derives from complex phenomena at catchment level. LW transport and budgeting charts are presented in linked literature (Steeb *et al.*, 2017). Nevertheless, even if the LW recruitment is not considered, the best approach in terms of efficiency to minimize consequences related to floods is to mitigate log jams at bridges (De Cicco *et al.*, 2020). Literature works linked to past floods can offer clues on the estimated volume of driftwood (De Cicco *et al.*, 2018). However, information gathered through such process usually concerns mainly clogging build-up at piers (Mazzorana *et al.*, 2018). Conversely, evidences demonstrated that the accumulation of logs is likely to happen at single-span bridges too (Schalko *et al.*, 2017). Likewise in these circumstances, flume tests play a crucial role to unravel the mechanisms of the clogging process. The limitations are linked to scale-related issues on the stiffness and moisture content of log samples, likely overestimating the blocking probability, as noted by De Cicco *et al.* (2018). Conversely, improving the smoothness of such mock-ups results in an underestimation of the phenomenon, thus balancing these challenging effects. Actually, field analysis on LW clogging revealed that flumes provide accurate modelling of both effects: backwater rise and blocking probability (Wyss, Schalko and Weitbrecht, 2021). Equally, the moisture content of wood logs still represents a major concern in holding LW, by using for instance a skimmer wall (Schalko *et al.*, 2018). Other elements that influence the clogging process are: (i) the presence of girder elements with sharp edges, accelerating the entrapment, (ii) a low freeboard and (iii) the uncongested or congested transport of LW (Gschnitzer *et al.*, 2017). Gschnitzer et al. (2017), assessed the driftwood clogging probability at bridge decks through a logistic regression using the outcomes of 5760 flume experiments. Some comprised countermeasures as a baffle mounted on the upstream side of the girder. In addition, the study also investigated the influence of different log shapes including effects of branches. A separate experimental campaign by Schmocker and Hager (2011), computed the blocking probability for a single log only, because tests proved the importance of the first entrapment on the formation of a jam. This phenomenon is dissimilar to the one occurring on piers, as it does not change with the orientation of the log, but after the first entrapment, it is unlikely that the clogging process reverts (Panici and de Almeida, 2018). The blocking probability is given accounting for the log geometry, bridge features and Froude number of the flow.

To tackle the issues linked to LW build-up at bridges, it is essential to develop efficient mitigation actions. These measures may comprise a series of strategies to plan and execute structures as debris

rack or deflectors, that support the diversion of LW from the elements of a bridge (Schalko *et al.*, 2019). Advanced monitoring systems that utilize sensors and remote sensing techniques can also provide real-time information on LW accumulation and assist in making timely decisions to mitigate potential risks (Qi *et al.*, 2022).

In summary, the consideration of LW accumulation and clogging effects on bridges is essential for ensuring their structural integrity and the safety of communities. Flume experiments, field studies, and numerical modelling techniques are valuable tools for investigating the blocking probability, understanding the clogging mechanisms, and developing effective mitigation strategies. Continued research efforts and collaborations between researchers, engineers, and stakeholders are crucial for advancing the knowledge in this field and enhancing the resilience of bridge infrastructure.

2.1.5. Simulations using River Analysis Software (RAS)

Together with tests on flumes, simulations using software are helpful to calculate the deposition and transport of driftwood on a catchment's scale (De Cicco *et al.*, 2020). Nevertheless, additional progresses are necessary to estimate impacts on bridge decks. Considering the scope and objectives of this work, HEC–RAS is chosen as river hydraulics simulation software, primarily due to its widespread recognition and extensive utilization by practitioners. It is important to note that while HEC–RAS is widely recognized and used in the field, there are other software tools available that can also contribute to the assessment of driftwood clogging on bridges (Ruiz-Villanueva *et al.*, 2014).

Within HEC–RAS there is a module that allows to simulate the effect of clogged debris, although only at piers. Indeed, there is no possibility to model such phenomenon against decks (Brunner, 2016). Frequently, clogged driftwood on bridge decks is accounted by varying the deck's geometry; specifically, the girder soffit is progressively lowered as the clogging process progresses (Parola, Apelt and Jempson, 2000). Other works compute the accumulation of driftwood on abutments instead, thus reducing the bridge span (Ruiz-Villanueva *et al.*, 2013). Just in those scenarios HEC–RAS admits the inclusion within the hydraulic model of a blocking obstacle.

A central challenge tackled by this work is to combine deterministic approaches included in software as HEC–RAS, within a probabilistic framework. The method integrates also changes in the geometry of a bridge to simulate the clogging process. To compensate for the lack of such tool, the work employs the HEC–RAS Controller item executed through Python scripts. The implementation of Python routines complements the capabilities of HEC–RAS, enabling the modelling of the clogging process and

the simulation of incremental water elevation. Python, as a versatile programming language, allows for the development of customized scripts that automate the simulation process, facilitate data analysis, and enhance the integration of HEC–RAS within the probabilistic framework. The use of Python routines streamlines the workflow by improving its efficiency.

By considering the uncertainties associated with bridge geometry, a Monte Carlo analysis is used to provide a range of possible outcomes and their associated probabilities. This probabilistic approach enables the generation of fragility curves, which describe the likelihood of a bridge failure as a function of the driftwood accumulation and the corresponding water elevation. The method provides valuable insights into the bridge failure probability and can be used for supporting decision-making processes related to bridge design, maintenance, and risk management.

2.2. Empirical Fragility Analyses

In addition to analytical formulations, the examination of previous bridge collapses has revealed recurring failure patterns. However, as previously mentioned, floods have received less attention compared to seismic hazards due to the intricate nature of the involved variables (Tubaldi *et al.*, 2022).

To assess the susceptibility of bridges to flooding, it is possible to create empirical fragility curves. These tools prove helpful for decision-makers in prioritizing retrofitting efforts and mitigating risks to enhance resilience and minimize potential damages. In this context, the FEMA P-58 methodology for seismic performance assessment can be adapted to generate fragility curves for bridges exposed to flooding (ATC, 2018). The analytical framework of P-58 can be extended to account for hazards other than seismic, utilizing metrics similar to those employed in seismic fragility analysis, such as displacements of selected structural components (Padgett, Spiller, and Arnold, 2012; George and Menon, 2021). However, since information on these metrics is often lacking for most damaged structures, it becomes necessary to explore original metrics. This approach is a common practice in flood fragility analysis, unlike seismic hazard analysis, as the literature indicates a variety of intensity measures, which depends on the available data and the specific failure mode under investigation (Mondoro and Frangopol, 2018; Tanasić and Hajdin, 2018; Yilmaz, Banerjee, and Johnson, 2018). Recently, a seismic risk assessment approach has been employed to evaluate structural damage caused by hydraulic forces during the 2021 flood in a portfolio of buildings located in the Ahr valley. This method utilizes a seismic

damage classification as the foundation for the flood damage model (Maiwald *et al.*, 2022). However, only Anderson *et al.* (2017) developed empirical fragility curves for bridges exposed to river floods.

2.3. Network Disruption Analysis

In the field of transportation network analysis, the performance of bridges plays a crucial role in the network functionality. Evaluating disruptions on roads has been the subject of extensive research over the past two decades, with various authors proposing indicators to assess network performance. Comprehensive reviews of these metrics can be found in the studies by Mattsson and Jenelius (2015) and Jiang *et al.* (2021). Among these metrics, one widely adopted indicator is the Network Robustness Index (NRI), which is initially developed by Scott *et al.* (2006). This pioneering work highlights the significance of network connectivity beyond the conventional volume-capacity ratio, associating the travel-time cost with network performance. This demonstrates that a local disruption may lead to extensive network consequences. The concept is further explored and extended by Nagurney and Qiang (2007) introducing the network efficiency as an indicator by comparing pre- and post-disruption conditions, the decrease in network efficiency can be assessed.

However, both the NRI and network efficiency metrics have limitations when accounting for specific trip purposes. To address this issue, Sullivan *et al.* (2010) proposes an adaptation of the NRI, known as the Network Trip Robustness (NTR), aimed to incorporate also trip purpose considerations. Another approach that combines local and global metrics is presented by Rupi *et al.* (2015), where links are ranked based on both the average daily traffic (ADT) and the variation in trip costs. However, it is essential to acknowledge the potential impact of limited datasets on the outcomes of network performance analysis (Rupi *et al.*, 2015).

While researchers have proposed various methods, the assessment of the impact of closed links on the network typically relies on comparing the network's performance before and after a disruption, with variations in the employed metrics. The generalized travel cost is one of the most commonly utilized metrics (Xu *et al.*, 2017), but alternative approaches have also been explored. For example, Bagloee *et al.* (2017) highlighted the limitations of single-link closures in capturing the combined effects of multiple-link disruptions, emphasizing the importance of considering cascade effects in path-based scenarios. Recent studies have attempted to integrate hazard simulations, such as floods or earthquakes, with

network disruption scenarios (Kermanshah and Derrible, 2017). Arrighi *et al.* (2019) presented an integrated approach that directly links the accessibility index to the hazard return period.

Despite the availability of advanced methods, further research is needed to develop algorithms that can account for the limited availability of datasets in rural areas. Traffic data is often readily available in densely populated regions through cameras and traffic sensors, while data collection poses budget constraints for local authorities in rural areas (Khan *et al.*, 2018). Statistical analysis remains a common approach, despite its limitations (Selby and Kockelman, 2013). However, the emergence of web-based traffic data has provided a promising alternative, with tools like the Google Maps API enabling the gathering of traffic information without the drawbacks of statistical models (Alsobky and Mousa, 2020). Web image-based algorithms, such as the use of colour histograms, have been explored to extract traffic data from platforms like Google Maps (N. Petrovska and A. Stevanovic, 2015).

This study aims to contribute to the field by combining image analysis with engineering theory to quantitatively estimate traffic conditions on roads. While recent approaches often rely on crowdsourced data (Sarvepalli and Davis, 2020), this study focuses on utilizing a web image-based algorithm to gather qualitative data and then utilizing traffic engineering theory to convert this qualitative information into quantitative data. Furthermore, this research addresses specific research needs, including accounting for trip purposes, estimating the percentage of heavy vehicles in traffic flow, estimating vehicle operative costs (VOCs) for cars and trucks, and explicitly considering speed reductions based on the nonlinear volume-capacity ratio. Although individual parameters have been investigated in previous studies, such as the willingness to pay for each extra minute of driving (Pulugurtha, Penmetsa and Duddu, 2019), the need to merge different approaches and disciplines to comprehensively assess disruptions on rural roads still exists.

While more complex approaches that integrate traffic and hazard simulation methods are available (Zhang and Alipour, 2020), this study focuses on demonstrating a potential strategy to address the aforementioned research needs. The proposed methodology is modular, allowing for further improvements and adjustments in each step. For instance, a disruption management module and a module for human-made or natural hazard simulations could be incorporated (Togia *et al.*, 2019). The practical assessment of road network performance involves comparing user costs after a disruptive event to the stationary pre-event conditions. The framework, demonstrated in Chapter 6, accounts for data availability issues by developing an innovative quantitative traffic data gathering method based on qualitative information. The applicability of the proposed method is tested on a real network located in Tuscany, Italy, as per Chapter 7.

3. Bridges affected by the 2021 Flood in Germany

In this Chapter, evidences are gathered from bridge owners after the 2021 flood in Germany. These data encompasses the classification of damages using surveys, pictures, and official reports including the bridge condition ratings. Subsequently, a hydraulic model calibrated on the July 2021 flood is utilized to reconstruct the hazard magnitude at each bridge site (Apel, Vorogushyn, and Merz, 2022). The objective is to establish a connection between the damage level and a metric representing hydraulic forces, ultimately resulting in the creation of fragility curves.

For clarity and structure, § 3.1 provides an overview of the flood event, while § 3.2 details the bridge database, highlighting recurrent failure modes. Paragraph 3.3 is dedicated to the process of generating fragility curves, and § 3.4 presents the results, including insights gained from the research and its limitations.

3.1. The Flooding event of July 14th–15th in Germany

The flood that occurred in July 2021 primarily impacted Germany, Belgium, and Luxembourg, resulting in a tragic toll of more than 200 fatalities, 184 of which in Germany and 38 in Belgium (Kreienkamp *et al.*, 2021). This summer flood of 2021 has been documented as the most expensive flood-triggered disaster in Europe and the deadliest in the past three decades (Mohr *et al.*, 2022). It caused extensive damage to various infrastructure, particularly bridges, which led to the isolation of numerous rural communities (Schüttrumpf *et al.*, 2022). Additionally, the flood disrupted intermodal transport by damaging railway lines, exemplified by the prolonged reconstruction expected in the Ahr valley (Szymczak *et al.*, 2022). Furthermore, gaps in the warning system and damage to critical infrastructures emphasised the urgent need for enhancing disaster management and infrastructure planning (Truedinger *et al.*, 2023).

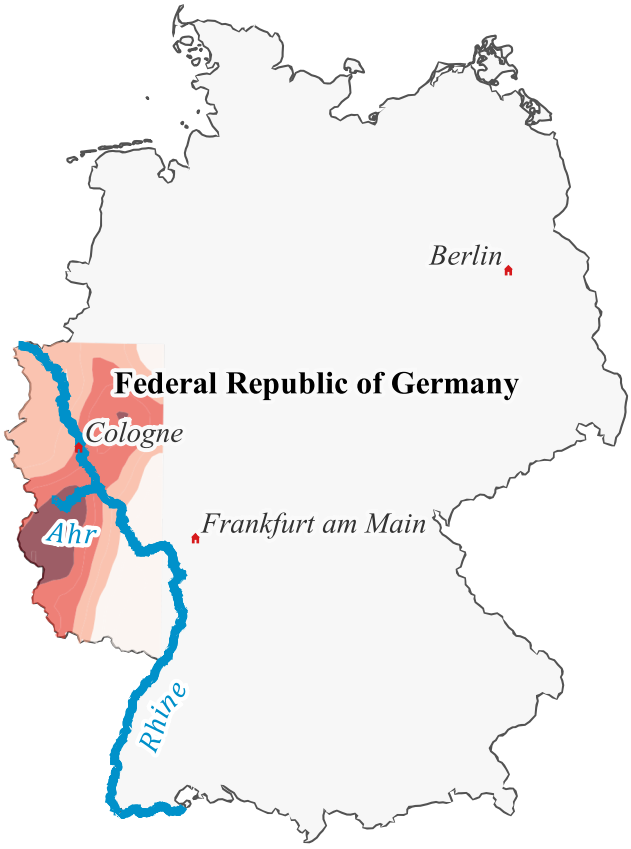


Figure 10. Daily accumulated precipitation (combined microwave-IR) 0.1 deg. [GPM GPM_3IMERGDF v06], July 14th – 15th , 2021 (Huffman et al., 2019). NUTS250 as basemap (BKG, 2022b), Waterbody-DE as source for the river shapefile (BfG, 2022). The accumulated precipitation is highlighted with different shades: darker (>90 mm/24h), intermediate (50 to 90 mm/24h), lighter (30 to 50 mm/24h)

3.1.1. Rainfall Distribution

The rainfall event in the Ahr river catchment, as depicted in Figure 10, was exceptionally severe. This basin experienced more than 60 mm of rainfall within a 24-hour period, with two-thirds of the area receiving over 100 mm (Huffman *et al.*, 2019). In 2016, another flood occurred in the Ahr River, with a discharge value close to what would typically have a 100-year return period. However, in terms of precipitation, this event was milder compared to the one in 2021. What caused the water levels to rise in 2016 was the extended duration of rainfall that began a week before the flood event, leading to a decreased soil's capacity absorbing water (Szymczak *et al.*, 2022). In contrast, the 2021 event witnessed the majority of the rainfall occurring within a 24-hour timeframe, producing peak flows in all secondary reaches (Roggenkamp and Herget, 2022). These high discharges converged in the main reach, the Ahr river. Additionally, the antecedent soil moisture condition was influenced by a persistent depression in the area. Although the peak of the rainfall event happened on July 14th, the event began on July 12th and

continued in the area until July 12-13th, after which the depression temporarily moved towards the Baltic Sea before returning to affect the region on July 14-15th. Thus, one of the contributing factors to such extreme precipitation can be attributed to increased evaporation due to exceptionally high sea temperatures compared to the average for that period (Szymczak *et al.*, 2022). Consequently, it can be affirmed that a climatic change or shift played a role in this unprecedented disaster.

Prior to this event, the river gauge at Altenahr would have measured a discharge of 241 m^3/s for a 100-year return period. Through regression analysis, the 200-year return period peak discharge can be inferred as approximately 265 m^3/s, with $R^2 = 0.99$. This correlation is made using discharge data for return periods of 2, 5, 10, 20, 25, and 50 years. However, as shown in Figure 11, the peak discharge for the 2021 event, as reconstructed by LfU, is estimated at 991 m^3/s (Landesamt für Umwelt Rheinland-Pfalz, 2022). This significant disparity raises additional questions about how flood events are handled, including the appropriateness of extreme value distributions and the role of in-line structures in creating backwater effects when debris accumulates.

Regarding the first question, historical records indicates that the highest discharges in the Ahr river are approximately 1200 m^3/s occurred in Dernau in 1804 and about 600 m^3/s in Altenahr in 1910 (Roggenkamp and Herget, 2014). Peculiarly, these events were not considered in the flood risk assessment conducted by local authorities, which might raise a debate from a risk management perspective. This is particularly noteworthy because similar discharge values were observed in 2021, as depicted in Figure 11 (Bruno Merz *et al.*, 2022). On the other hand, if these rare events were analysed using Extreme Value Theory, they would yield return periods of approximately 10^8 years, underlining a limitation of such statistical models (Ludwig *et al.*, 2022).

The second issue pertains to human-made alterations in the river's cross-section (e.g., parking lots in Altenahr) and the damming effect of bridges, often causing backwater effects (B. Merz *et al.*, 2022). Particularly noteworthy is the interaction between bridges and drifting debris, which frequently leads to clogging and damming (Vorogushyn *et al.*, 2022).

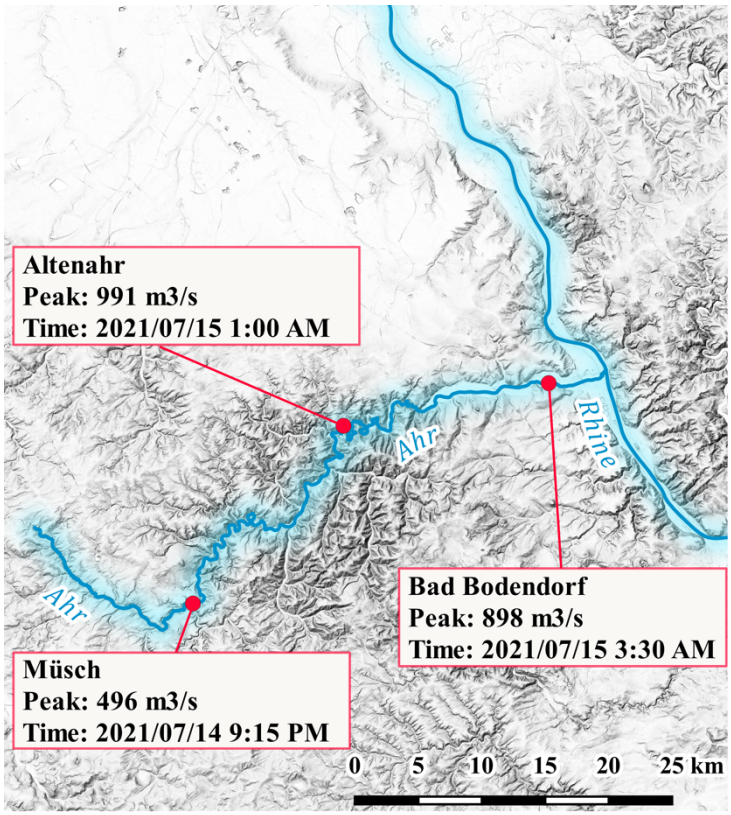


Figure 11. The preliminary data from LfU provides information on how the peak discharge along the Ahr river has evolved over space and time (Landesamt für Umwelt Rheinland-Pfalz, 2022)

This situation is evident in the upper section of the Ahr basin, where small streams retain a substantial volume of sediment and transport wood logs, as depicted in Figure 12. This circumstance is not unique, as erosion rates in Germany frequently surpass acceptable limits (Seeger, 2023). In the end, the movement of driftwood is the primary cause of bridge obstruction, leading to a growth in the horizontal force exerted on bridge decks and piers (Oudenbroek *et al.*, 2018).



(A) (B)

Figure 12. Debris accumulation in Eichenbach, a tributary of the Ahr river, characterized by: (a) the presence of wood logs, some of which measure up to 15 m in length, and (b) have an average diameter of approximately 17 cm for the carried logs. Photos shot by the Thesis' author

3.2. Database of Damaged Bridges

The damaged bridges are situated in two German federal states: North-Rhine Westphalia (NRW) and Rhineland-Palatinate (RLP). As per the German federal bridge database, are found nearly 0.045 federally-managed bridges per km^2 over rivers in NRW and 0.040 in RLP. This translates to approximately 1500 bridges under the jurisdiction of the federal road authority in NRW and 800 in RLP. The database presented here includes 250 bridges, primarily comprising locally managed structures. Given the spatial distribution of rainfall as mentioned, only 32% of these structures are located in NRW, while the remaining 67% are in RLP. Out of these, 99 bridges (representing 60% of the total) are situated over the Ahr river. Consequently, this analysis primarily focuses on this specific watercourse. In Figure 13, the accumulated precipitation is superimposed on the kernel density distribution of the 250 damaged bridges, highlighting the spatial correlation between the severity of the weather event and the bridge damage.

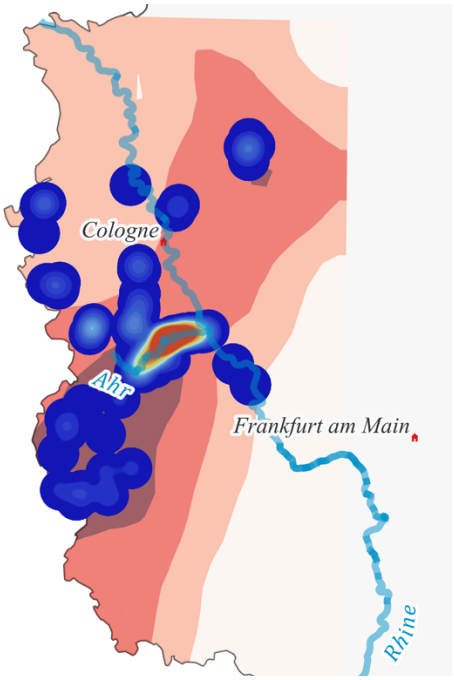


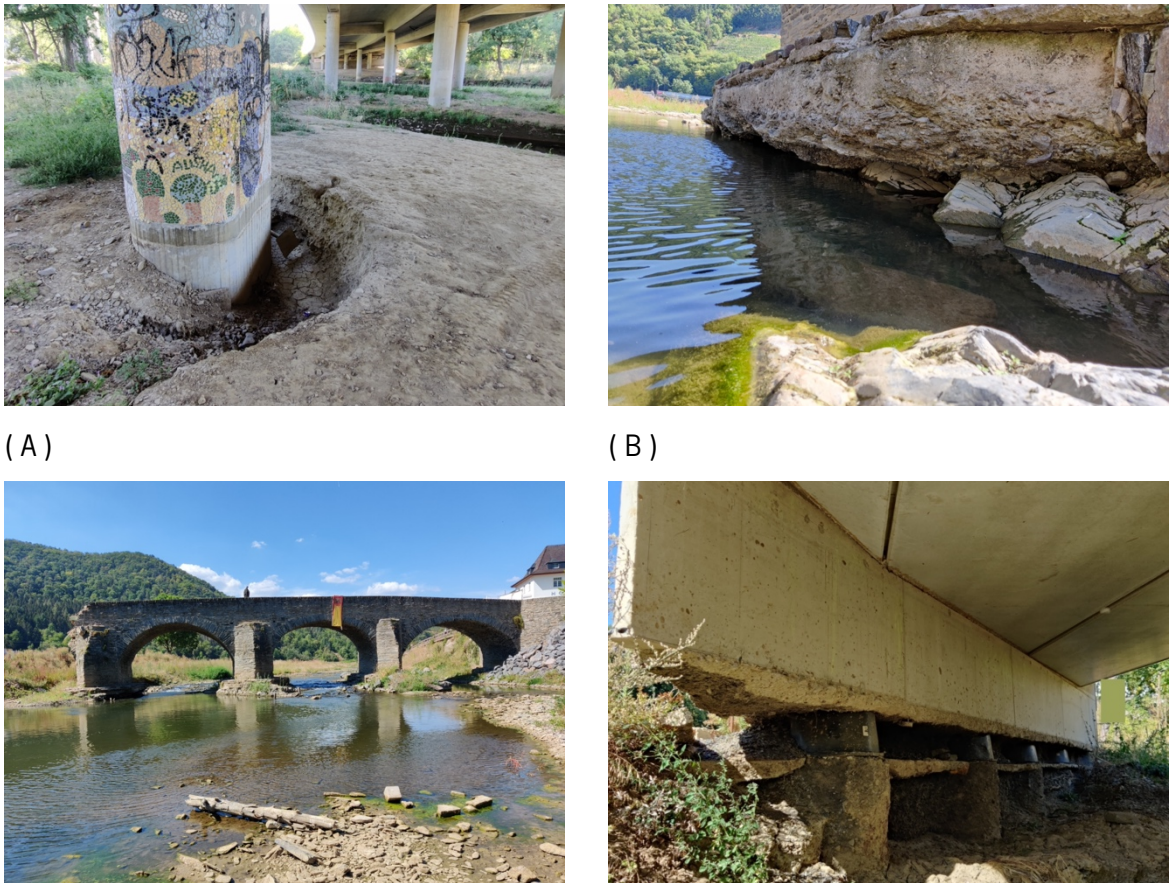
Figure 13. A spatial kernel density estimation has been applied to illustrate the distribution of damaged bridges, represented by dots (blue to red). The Ahr valley emerges as the region most severely affected. Additionally, it is evident that the upper segment of the river basin experienced the highest hydrological stresses, indicated by darker red areas on the rainfall map, where rainfall exceeded 90mm. These conditions led to increased hydraulic forces along the watercourse. Other notable regions are highlighted based on the cumulative daily precipitation, with values falling within the range of 50 to 90mm denoted by red shading, and 30 to 50mm indicated by a lighter red hue. The rainfall dataset is taken from satellite data: (combined microwave-IR) 0.1 deg. [GPM GPM_3IMERGDF v06], July 14th – 15th , 2021 (Huffman et al., 2019). The Germany GIS map is taken from NUTS250 (BKG, 2022b), while the shapefile of Rhine and Ahr from Waterbody-DE (BfG, 2022)

3.2.1. Overtopping and Scouring Mechanisms

The information on each asset is gathered by the Author conducting a dedicated survey, and this data is further enriched by incorporating additional details such as location, missing bridge features, and cross-sectional elevation. The elevation data is obtained from 5-meter and 1-meter digital elevation models (DEMs) (BKG, 2022a, 2022b; LVermGeo, 2022; BfG, 2022). Subsequently, a survey campaign is carried out in collaboration with Ing.-Dipl. Daniel Eickmeier and Ing.-Dipl. Ralph Holst from BASt (Bundesanstalt für Straßenwesen) to delve into the specifics of failure mechanisms. During this campaign, various measurements are collected, and photographic material is documented, as illustrated in Figure 14 and 15. In particular, two primary types of failures are identified: those attributed to scour and those induced by hydraulic forcing. In both cases, the presence of debris obstruction exacerbates these phenomena. Scour refers to the erosion of soil in the vicinity of bridge foundations caused by the erosive action of water from the riverbed and riverbanks. It develops due to the localized hydraulic interaction between the bridge structure and the material in the streambed. As the depth of scour increases, it diminishes the lateral support provided by the soil beneath the structure, leading to settlement of the foundations (Zhang *et al.*, 2022). The survey campaign conducted unveils various types of scour in the Ahr river, which included local scour, contraction scour and long-term riverbed degradation. In . Figure 14 (A), it is highlighted a pit scour hole resulting from the 2021 flood event, with an average depth of approximately 60 cm. The formation of these pits is influenced by the erodibility of the soil, as evidenced by the presence of clay at the bottom of the pit, causing it to shrink. Typically, these pits tend to deepen and expand over time, posing a significant risk to the structural integrity of the bridges. Consequently, it is necessary to monitor structures affected by this type of damage and take preventive measures to ensure that scour does not reach a critical depth.

In Figure 14 (B), it can be observed a pier of the St. Nepomuk Bridge, which is also depicted in Figure 14 (C) as the rightmost pier in the picture. This bridge, a masonry arch structure constructed in the 18th century, suffered partial collapse during the 2021 flood event due to erosion in the approach fill, visible as the missing arch on the left side of picture Figure 14 (C). This erosion resulted in an imbalance in the horizontal thrust of the arch, ultimately leading to its collapse. Additionally, the bridge's in-stream piers are affected by scour, as indicated in Figure 14 (B). As evident from the figure, the pier is constructed with a shallow foundation directly resting on riverbed stones, and a scour depth of 70 cm is measured. The erosion also had an impact on the pier itself, with the aging mortar used in the bridge partly eroded and easily crumbling under minimal pressure. However, a comprehensive investigation of the overall

scour condition of the bridge is necessary, as the upstream side of the bridge does not display signs of sediment accumulation, suggesting a long-term process of degradation. This situation is exacerbated by the narrowing of the flow under the bridge, which locally intensified water velocity. Figure 14 (D) provides an illustration of channel flanking scour observed on a bridge situated along the Ahr river with deep foundations. This phenomenon results in the erosion of the soil adjacent to the bridge abutment, leading to the exposure of the pile heads. Channel flanking scour has the effect of widening the channel, which in turn amplifies the risk of instability along the riverbanks (Arneson *et al.*, 2012). In this specific case, the bridge did not collapse; however, in numerous other instances along the Ahr river, channel flanking scour had indeed resulted in bridge failures. In summary, scour inflicted significant damage on masonry arch bridges, whereas reinforced concrete structures with deep foundations experienced only minor effects from it.



(A) (B)

(C) (D)

Figure 14. Scour mechanisms observed during the survey include: (A) pit scour, (B) pier scour, (C) approach fill scour, and (D) channel flanking scour. These images were shot by the Thesis' author

Other frequent failures are initiated by deck overtopping, with clogged debris playing a significant role in this process. The size of hydrodynamic forces was intensified by the presence of wood logs and

transported material, leading to the formation of dams that had profound repercussions on both the structure itself and its immediate surroundings, resulting in backwater effects.

Figure 15 (A) depicts the remaining in-stream pier of a wooden bridge, while its deck was discovered approximately 5 km downstream. In Figure 15 (B), it is shown the steel deck of a footbridge, which was dragged several hundred meters from its original location. From these examples, it is evident that only lightweight decks were subject to dragging. However, post-flood research works indicates that some mixed steel-concrete road decks and a steel deck of a railway bridge also experienced dragging (Szymczak *et al.*, 2022).

During the 2021 flood, hydraulic forces acting on the decks caused damage to all structures, and a visible pattern emerged: beam bridges with simply supported spans exhibited a greater susceptibility to hydraulic forcing when compared to arch bridges. Notably, no arch bridges that were overtopped experienced complete collapse. Masonry arch bridges, on the other hand, sustained severe damage, including the removal of infill material, carriageways, and railings. However, their ultimate failure was primarily triggered by scour, as illustrated in Figure 15 (D). In contrast, overtopped arch bridges constructed with reinforced concrete suffered relatively minor damage compared to masonry ones, primarily affecting railings and parapets, as seen in Figure 15 (C).

In the context of wood log impact and clogging, conducting experimental campaigns can offer valuable insights into the predominant forces (Schmocker and Hager, 2011; Gschnitzer *et al.*, 2017; Majtan, Cunningham, and Rogers, 2022). By looking at relevant literature and as evidenced in § 2.1.4, clogged driftwood against bridges significantly diminishes structural safety by increasing the area exposed to the impact of the flow.

Upon reviewing the gathered evidence, it became clear that driftwood played a pivotal role in the collapse of both arch and beam bridges. In contrast, damages attributable to uplift forces can only be considered in the case of wooden structures, as wood holds greater buoyancy compared to other materials, and there is no evidence of such effect within the portfolio of examined structures.



Figure 15. Examined overtopping mechanisms include: (A) dragging of a wooden deck; (B) dragging of a steel deck; (C) railing damage resulting from overtopping; and (D) a combination of overtopping and scour, with the latter being the primary factor leading to structural failure. These images were shot by the Thesis' author

3.2.2. Classification of Damage according to DIN 1076

The German Standard DIN 1076 prescribes the safety and functionality requirements of road infrastructure, particularly focusing on the examination and evaluation of Bridges, Tunnels, and Culverts (Naumann and Holst, 2005). Various types of damage are carefully assessed and rated, providing justification for any reduction in structural integrity, durability, or traffic safety. To assist analysts in determining the condition rating of a bridge, guidelines have been established, utilizing a grading system that spans from 1 to 4, inclusive of one decimal place (Haardt, 1999). The most favourable condition for a structure is denoted as 1, while 4 is reserved for structures that have collapsed. It's worth noting that this scale is not linear, meaning that a structure rated 2.0 is not necessarily twice as safe as one rated 4.0. Similarly, the decimal point at threshold boundaries should not be interpreted as a minor increment.

For instance, moving from 3.4 to 3.5 indicates a significant difference in damage severity. The classification adheres to the scheme outlined in Table 4.

Table 4. DIN 1076 definition of condition ratings for bridges (Haardt, 1999)

Rating	**Structural Safety**	**Traffic Safety**	**Durability**
1.0 - 1.4	Not compromised	Not compromised	Not compromised
1.5 - 1.9	Not compromised	Not compromised	In the long-term it can be compromised
2.0 - 2.4	Not compromised	Not compromised	In the medium-term it can be compromised
2.5 - 2.9	Not compromised	It can be compromised	It can be compromised
3.0 - 3.4	Is compromised	Is compromised	Extensively compromised
3.5 - 4.0	Extensively compromised	Extensively compromised	Extensively compromised

Within the database of bridges affected by the 2021 flood, numerous structures underwent post-event inspections carried out by certified surveyors. Regrettably, for certain structures, such inspection data are unavailable. In such cases, alternative forms of documentation, including photographs and damage reports, are collected for most of these bridges. To address the challenge of having quantitative information for some entries and qualitative information for others, expert judgment is utilized to standardize and harmonize the two sets of data. However, a small fraction of structures lacks sufficient data for assessment and, consequently, is excluded from consideration. The process of assigning categories to bridge ratings is made more straightforward due to the semantic descriptions associated with them. This process takes into account the comprehensive description outlined in DIN 1076, which is briefly summarized in Table 4.

To strike a balance between granularity and precision, four distinct damage categories are established:

- D1 = undamaged;
- D2 = slightly damaged
- D3 = moderately damaged
- D4 = extensively damaged

The categories employed here deviate from the HAZUS classification system, which includes slight, moderate, extensive, and complete damage (Padgett, Spiller and Arnold, 2012). This variance primarily stems from the distinct rating systems associated with the structures involved. Specifically, the German bridge condition rating, based on DIN1076, differs from that of the NBI (National Bridge Inventory) (Haardt, 1999). Consequently, the categories chosen align with the HAZUS-based classification, which is commonly used in existing literature pertaining to empirical fragility curves for bridges (Padgett, Spiller and Arnold, 2012; Balomenos, Kameshwar and Padgett, 2020). This decision is made with the intention of simplifying future research-level comparisons while upholding a rigorous approach that adheres to the damage levels outlined in Table 4, as described in the German standard DIN1076. The sole deviation from the HAZUS classification system pertains to structural collapse (German rating = 4.0), which is equated with extensive damage in DIN1076. This distinction is made since the German rating spans from 3.5 to 4.0, as indicated in Table 4. In both the USA and Germany, these ratings are determined by qualified experts. In this context, the condition rating hinges on experts' judgment related to the boundary of the safety domain, which is closely linked to failure mechanisms. Furthermore, even though ratings of 1.0 to 2.9 generally signify a structurally sound and uncompromised bridge, it is deemed prudent to establish two categories to differentiate them based on the potential for damage that could compromise long-term durability. Consequently, the adopted scheme is presented in Table 5.

Table 5. Mapping bridge condition ratings to a qualitative damage level, determined by equivalence with the structural safety parameter

	Undamaged	**Slightly Damaged**	**Moderately Damaged**	**Extensively Damaged**
Damage Level	D1	D2	D3	D4
Rating	1.0 – 1.9	2.0 – 2.9	3.0 – 3.4	3.5 – 4.0

3.2.3. Population Statistics

Data regarding the construction date is successfully collected for 184 out of the 250 bridges. An examination of the age distribution in conjunction with the number of failures for each structural typology reveals that beams and arches are the most impacted categories, accounting for a total of 125 and 82 bridges, respectively. Notably, there is a substantial number of recently constructed beam bridges, particularly footbridges. Analysis of post-disaster evidence indicates that many of these structures collapsed due to unexpected water forces, often exacerbated by driftwood blockages, leading to increased horizontal thrust on the decks, as illustrated in Figure 15 (A) and (B).

Subsequently, an analysis is conducted by examining bridge inspection records from before the flood, comparing them to all bridges under federal management. Structures that appear in both databases are removed from the federal one. Through this analysis, a statistically significant difference in the average condition rating (prior to the flood) is identified among arch bridges that were damaged during the flood, when compared to their counterparts in the federal database. Similar differences are not observed for the other types of bridges.

Additionally, the data allow for a similar comparison after filtering the federal database to focus solely on bridges over rivers in the states of NRW and RLP. In this regard, a Kruskal-Wallis (K-W) test is conducted on the two databases. The K-W test, suitable for non-parametric data, is equivalent to ANOVA. The factor considered is the bridge typology, categorized as follows: a) beam and box girder bridges, b) arch bridges. Prior to the K-W test, the data is tested against the Levene's assumption, which resulted in the rejection of the null hypothesis with a confidence level at $\alpha = 0.05$ (Brown and Forsythe, 1974). The K-W test yields a significant result with a p-value of 0.0001. To gain further insights into each subgroup, a non-parametric Post-Hoc test is employed, with the p-value adjusted in accordance with Bonferroni's assumption (Bonferroni, 1936). The results indicate the most significant difference in condition rating among beam bridges, with an adjusted p-value of 0.0010, and among arch bridges, it is 0.0043. On average, the condition rating of damaged bridges assessed before the flood is statistically worse in comparison to the undamaged population. These differences naturally become more pronounced when considering the ratings assigned to the damaged bridges after the flood.

It's worth noting that while the test is significant as reported, not all undamaged structures were exposed to the same level of hazard magnitude. To provide further clarity on this aspect, an analysis is conducted to explore the correlation between the damage level and an intensity measure representative of hydraulic forces on bridges. The selection of triggering mechanisms is based on evidence obtained

from surveys and damage reports. Subsequently, it is determined that one mechanism, namely scour, predominates over hydraulic forcing. This finding is emphasized in Figure 16, taking into consideration the bridge deck typology (beam versus arch bridges) and the deck weight (heavy decks made of masonry and concrete versus lightweight decks constructed of steel and wood). Subsequently, the FEMA P-58 method is utilized to construct fragility curves based on these correlations (ATC, 2018).

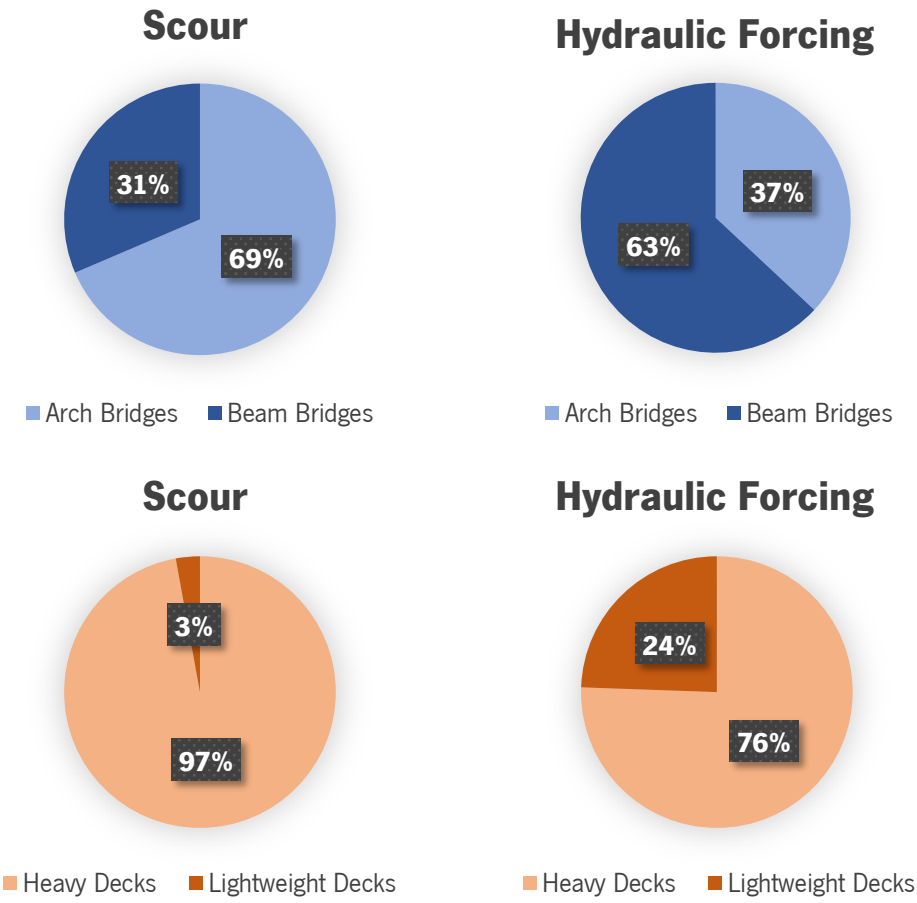


Figure 16. The proportions of arch bridges, beam bridges, heavy and lightweight decks concerning the two damage mechanisms

3.3. Fragility Curves Generation

Fragility curves describe the relationship between the intensity of a hazard and the resultant probability of experiencing a defined damage level suffered by structures. Different metrics can be employed to represent the hazard, and in the context of floods, it is customary to use metrics such as flow discharge or water elevation, depending on the specific scenario. In this particular study, a metric denoted as h^{**} is adopted. This metric represents the ratio between the flood height and the elevation of

the bridge deck, as illustrated in Figure 17. The choice of the symbol h^{**} is considered to distinguish it from h^{*}, which is referred to as the 'inundation ratio' and is defined in Equation (1).

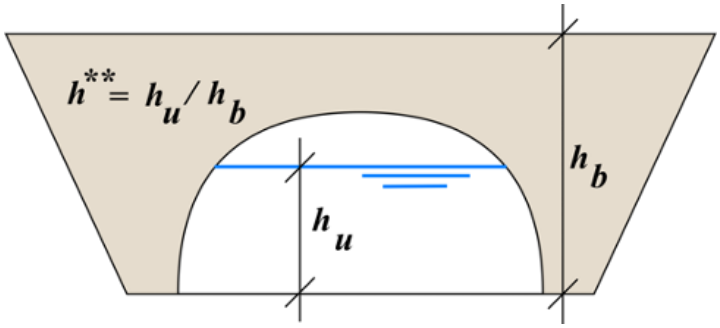


*Figure 17. The definition of h** as IM for the fragility model*

The chosen metric allows for the use of a single category across various bridge geometries, as the relative height exhibits a strong correlation with the observed damage levels.

In contrast, in other flood-related phenomena such as hurricanes, the storm surge may serve as a viable alternative. However, in regions like the one examined in this case, the varying bridge clearances present a challenge. Typically, bridges in mountainous terrains have lower clearances, while those downstream have higher clearances. Interestingly, despite this difference in clearance, both upstream and downstream bridges experienced similar levels of damage. Nevertheless, in such instances, recorded water elevations and flow discharges differ. On the contrary, the metric h^{**} remain relatively consistent. Consequently, from a structural perspective, h^{**} contributes to standardizing the population in terms of hazard assessment.

Another intensity measure considered is water velocity, but the lack of additional information to differentiate between different types of soils results in significant uncertainties. Furthermore, it is necessary to consider the simulated velocity upstream of the bridge, as local constriction can lead to a significant increase in velocity. As mentioned in § 3.1, the reconstructed peak discharge is valuable for investigating various aspects of the flood process. In this context, Apel, Vorogushyn, and Merz (2022) developed a hydraulic model of the Ahr River between Altenahr and Sinzig, examining the impact of buildings on the increased volume of water. As previously mentioned, the water discharge is similar to that of 1804, although minor damage was observed at that time. The study by Apel, Vorogushyn, and Merz (2022) holds particular relevance for infrastructure managers because the increased water height directly influenced bridges. Buildings occupied areas that would have otherwise been inundated by water, similar to the situation in 1804. This phenomenon raised water levels, supporting the use of water height as a characterization of hazard intensity. While discharge would have been a superior intensity measure,

such data are characterised by great uncertainty due to the river overtopping bridges, leading to pressurized flow underneath many structures.

The fragility curves are derived using the following equation:

$$F_d(r) = \Phi\left(\frac{\ln\left(\frac{r_i}{\mu_d}\right)}{\beta_d}\right) \tag{5}$$

The distribution parameters are determined using the Maximum Likelihood Estimation (MLE) technique, as follow:

$$\mu_d = \exp\left(\frac{1}{n_d} \cdot \sum_{i=1}^{n_i} ln(r_i)\right) \tag{6}$$

$$\beta_d = \sqrt{\frac{1}{n_d - 1}\sum_{i=1}^{n_i}\left[\ln\left(\frac{r_i}{\mu_d}\right)\right]^2} \tag{7}$$

In these equations, $F_d(r)$ represents the estimated fragility at intensity level r for damage state d. The parameters μ and β denote the mean and standard deviation values of the lognormal cumulative distribution, respectively, while n signifies the number of data elements or specimens collected empirically. The subscript d is used to distinguish between different damage levels. The model is subject to two tests for validation: a goodness of fit test and an outlier management criterion. The goodness of fit test assesses whether the data align with the hypothesized normal distribution. Typically, goodness of fit to a normal distribution is evaluated using the Kolmogorov-Smirnov (K-S) test. However, in this case, the fit is imposed by calculating μ and β, rendering the K-S tables invalid. In such cases, the Lilliefors' test is employed, which utilizes a modified K-S table (Lilliefors, 1967). Outliers are managed using the Peirce's criterion (Ross, 2003).

Confidence intervals are computed, taking into consideration the uncertainty provided by the Digital Elevation Model (DEM). The DEM's documentation reports an error of ± 0.3 up to 1 m, depending on the terrain type (BKG, 2022a). Assuming measurements are conducted with an accuracy of 0.5 m and considering 95% confidence intervals for the data points, Figure 18 is generated. However, it's important to note that since the relationship between velocity and water elevation is approximated due to data limitations, the fragility curves presented in § 3.4 are computed solely for h^{**} as the Intensity Measure (IM).

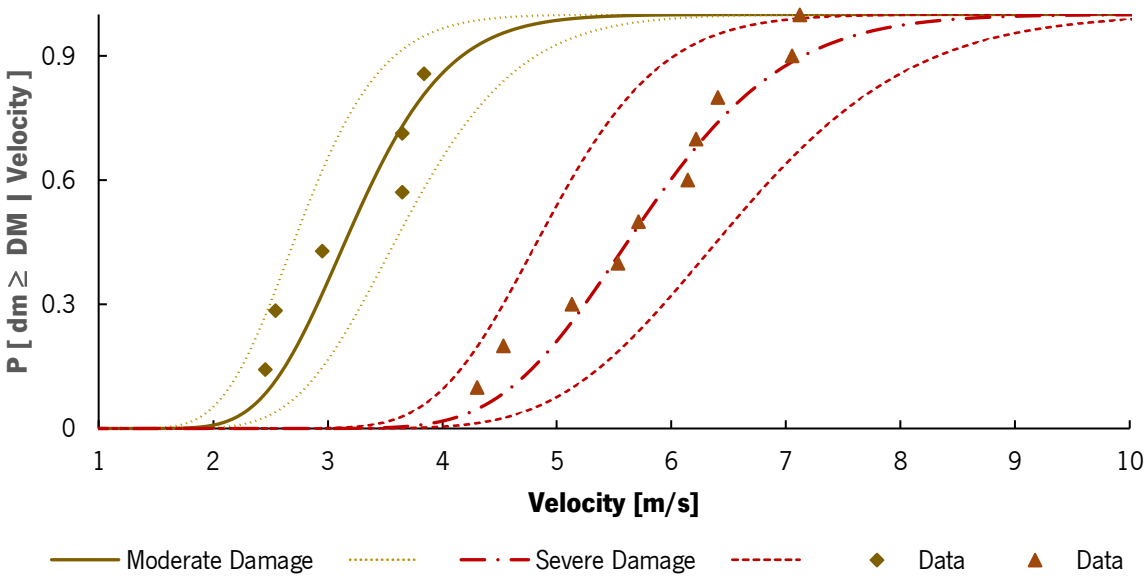


Figure 18. Confidence intervals for the damage states categorized as moderate and severe, specifically focusing on velocity data for Arch bridges. The 95% confidence intervals are prominently displayed along with the mean value derived from the fitted distribution

3.4. Results

The bridge population is categorized in two distinct manners: firstly, based on the material used in the bridge deck, and secondly, based on their typology. In the first categorization, structures with lightweight decks, such as those constructed with steel and wood, are distinguished from their heavier counterparts, typically made up of concrete or masonry. Steel and wood decks are jointly considered due to their similar observed failure modes, which include deck dragging and uplift. Similarly, concrete and masonry bridges are grouped together. Consequently, the term "lightweight" (abbreviated as LWY) is employed to denote structures featuring steel and wooden decks, while "heavy" (abbreviated as HVY) is used for those constructed with masonry and concrete materials. This nomenclature is retained in both Figure 19 and Figure 20. Regarding the failure mechanisms, the various scour typologies are consolidated into a single category, as illustrated in Figure 14, to distinguish them from those stemming from hydrodynamic dragging and uplift, as depicted in Figure 15.

Figure 19 presents the likelihood of encountering severe damage in both lightweight and heavy deck structures for the two distinct failure modes. It is evident that bridges affected by scouring exhibit significantly higher probabilities of incurring damage in both lightweight and heavy decks, in comparison to instances of hydraulic forcing failure mode. Nonetheless, when examining cases where the deck is not

overtopped (i.e., h**<1), a consistent pattern emerges across both damage mechanisms. This observation confirms that the damage incurred is not influenced by the deck's material composition but rather by additional factors associated with distinct failure mechanisms, such as the scouring of instream piles. For conditions where h**>1, variations do exist between lightweight and heavy decks under scour conditions, although these differences remain relatively minor when considering the inclusion of uncertainties, denoted by the 5% and 95% confidence intervals. It is worth noting that these intervals, although not explicitly represented in Figure 19 for clarity purposes, are displayed alongside the velocity data as the IM in Figure 18.

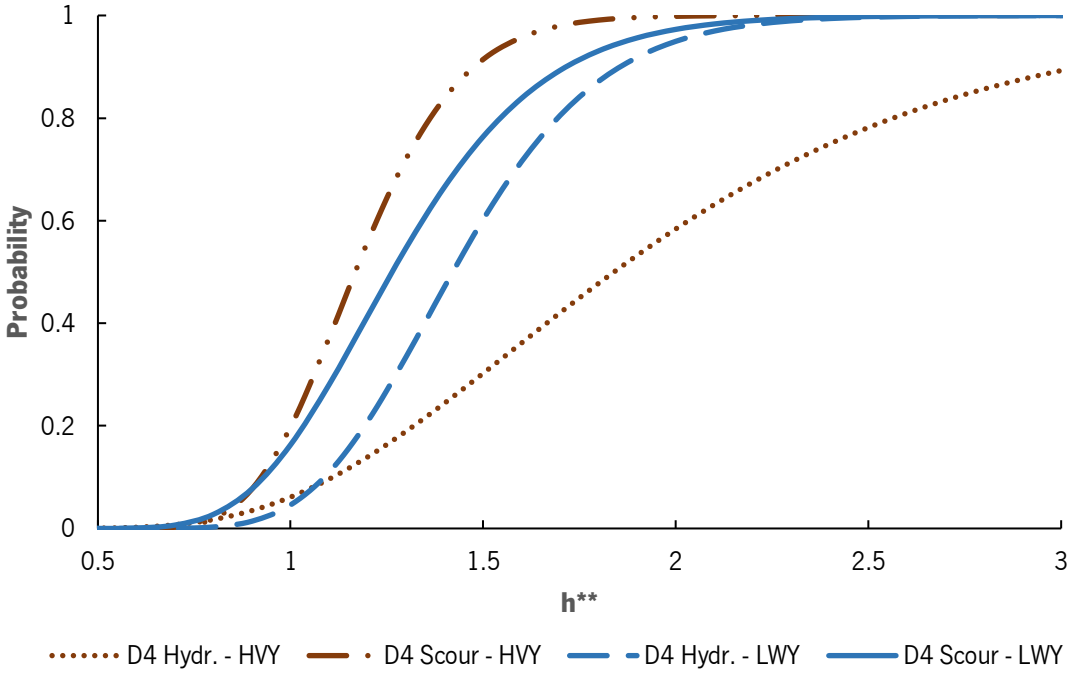


Figure 19. Fragility curves illustrating the susceptibility of heavy (HVY) and lightweight (LWY) bridge decks to severe damage under scour and hydraulic forcing (Hydr.) scenarios. The D4 designation corresponds to the damage level as defined in Table 5

Indeed, upon inclusion of the confidence bands (ranging from 5% to 95%), the most notable disparity between scour and hydrodynamic mechanisms becomes evident, particularly in the context of heavy decks within the overtopping range (h**>1). In this scenario, it is observed that heavy decks exhibit a reduced likelihood of experiencing severe damage during high water stages when compared to situations involving scour. Similar observations hold true for lightweight decks; however, it should be noted that the curves for these decks overlap when considering the confidence bands. Furthermore, distinctions become apparent when assessing damages resulting from high water stages. As anticipated, lightweight decks demonstrate significantly higher probabilities of incurring severe damage in comparison to their heavier counterparts.

When examining the categories of slight and moderate damage, it becomes evident that only heavy decks are affected, as depicted in Figure 20. Consequently, lightweight structures exclusively exhibit severe damage, reflecting their relatively lower resistance to hydraulic forces. Thus, Figure 20 illustrates the progression of damage states for heavy decks exclusively, subjected to the same failure mechanisms. As anticipated, the behaviour of heavy decks under scour exhibit a higher severity compared to that under the hydraulic forcing damage mechanism. Specifically, at low water stages, there is a greater likelihood of slight damage occurring. It's important to note that the degree of damage is also influenced by the presence of debris carried by the flow. However, due to the limited availability of data, it was not possible to assess the impact of this factor on the fragility model.

Another noteworthy observation pertains to the absence of slight damage during scour events. This reinforces the understanding that erosion poses a significant challenge for heavy decks, primarily resulting in moderate to severe damage. A crucial point of consideration is that when these bridges are overtopped (h**=1), there is an 80% likelihood of encountering moderate to severe damage in the case of scour, while the probability decreases to 36% when hydraulic thrust serves as the initiating damage mechanism. In terms of damage levels, the probability of scour causing moderate damage stands at 33%, with hydrodynamic loads being responsible for the remaining 67%. However, for severe damage, scour accounts for a substantial 78% of occurrences, leaving hydrodynamic loads responsible for the remaining 22%.

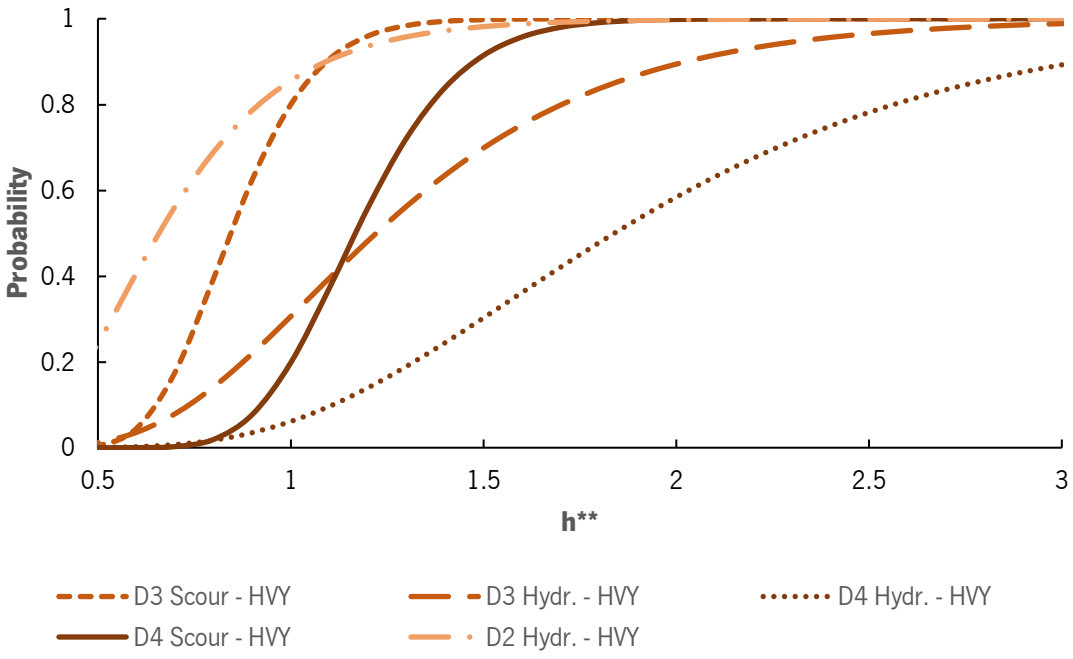


Figure 20. Fragility curves depicting heavy bridges (HVY) under both scour and hydraulic forcing (Hydr.) scenarios, encompassing all damage levels including D2, D3, and D4 as per Table 5

In the context of the second group, beam structures, which encompass trusses and box-girders, are differentiated from arch bridges. The outcomes for beam and arch bridges are elucidated in Figure 21 and Figure 22, respectively. An evident observation from Figure 21 is the absence of moderate damage within the category of beam bridges. Consequently, when consolidating the fragility assessments by considering both bridge material and typology, it becomes apparent that moderate damage, as depicted in Figure 20 for heavy decks, is exclusively attributed to arch bridges. An overarching trend that emerges across these findings is the pronounced impact of the scour mechanism, resulting in elevated probabilities of damage for a given h^{**}.

Another notable observation pertaines to the absence of arch failures attributed to the hydraulic forcing mechanism, as illustrated in Figure 22. Consequently, the severe damage induced by hydraulic forcing, as depicted in Figure 20, can be attributed to beam bridges. This raises a critical question regarding whether arch bridges are susceptible to collapse due to water thrust and which specific component of hydraulic forcing (drag or uplift) causes the most damage. While there is a consensus among studies and data regarding the dragging action, there is a divergence of findings with respect to the uplift component. Studies by Falconer *et al.* (2010) and Majtan, Cunningham, and Rogers (2023) suggest the presence of a positive uplift mechanism for arch bridges, referred to as "upthrust." Conversely, flume experiments on hydrodynamic forces acting on bridge decks conducted by other authors, including Jempson (2000), Kerenyi, Sofu, and Guo (2009), Oudenbroek *et al.* (2018), and Dean (2020), report negative uplift coefficients for most submergence ratios encountered during floods. This discrepancy in findings highlights an ongoing debate within the field. The dynamic effect of uplift is partially offset by the Archimedes' thrust, which may become predominant at higher submergence ratios due to less negative dynamic uplift at elevated water stages. The evidence collected from the collapsed bridges during the 2021 flood in Germany aligns with a positive drag and negative uplift scenario, as none of the arch bridges exhibit the failure mechanism described in Falconer *et al.* (2010). Instead, the damage to arch bridges is attributed to the combined effect of wood clogging and drag forces. A major issue arose from the substantial blockage of arches by debris, resulting in significant drag forces that contributed to the removal of backfill, leaving the arch structure standing against the flow (Grates, 2023). Additionally, the impact of hydraulic forcing against the intrados often led to minor damage, such as detachment of masonry mortar, exposed rebars, and damage to parapets, among other effects. This phenomenon is illustrated in Figure 22, where instances of slight damage are observed for partially submerged arch bridges (h^{**}<0.5).

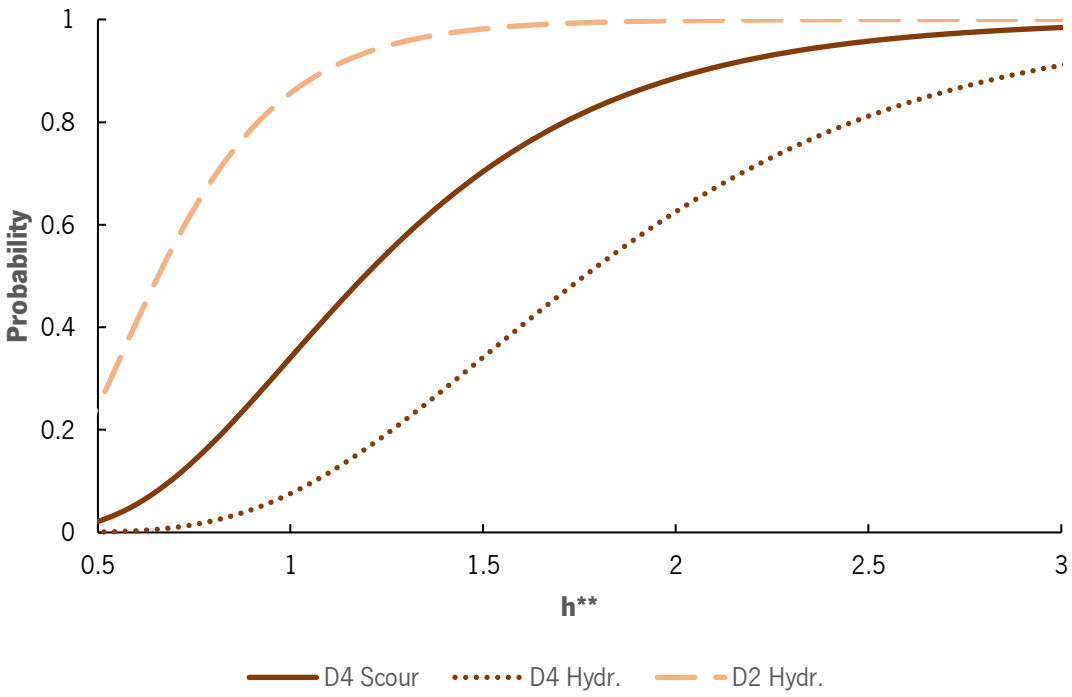


Figure 21. Fragility curves illustrating the susceptibility of beam bridges to damage under the influence of scour and hydraulic forcing (Hydr.) mechanisms are presented. The damage levels, denoted as D2 and D4, are in accordance with the classifications outlined in Table 5

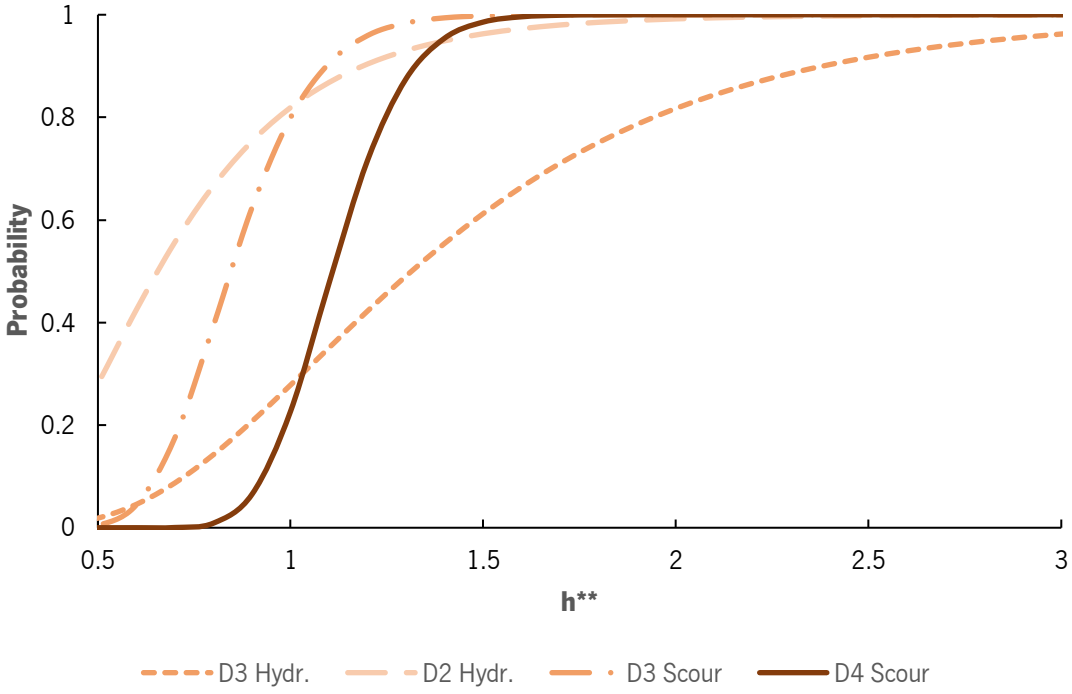


Figure 22. Fragility curves depicting the vulnerability of arch bridges to damage under scour and hydraulic forcing (Hydr.) scenarios are displayed. The damage levels, specifically denoted as D2, D3, and D4, align with the categorizations outlined in Table 5

In contrast, the drag forces acting on beam decks are comparatively less pronounced than those experienced by arch bridges, primarily attributed to their reduced blockage. Nonetheless, beam bridges demonstrate significant damage stemming from water thrust, particularly notable in simply supported decks, as illustrated in Figure 15 (A) and (B). It is worth noting that the pursuit of superstructure weight optimization can result in vulnerabilities when confronted with elevated water levels, a phenomenon confirmed by existing research (Balomenos, Kameshwar and Padgett, 2020).

Finally, when considering slight damage (D2), nearly indistinguishable probabilities are observed for both typologies, as depicted in Figure 21 and Figure 22. This observation aligns with empirical evidence, as arch and beam bridges encounter distinct phenomena that can nevertheless be classified within the same damage category.

In summary, within the examined database, arch bridges exhibit greater robustness than beam bridges when subjected to high water stages. Nevertheless, beam bridges demonstrate a lower occurrence for damages caused by hydraulic forcing due to their reduced obstruction to the flow. Regarding scour, it is evident that arch bridges experience both moderate and severe damage, while beam decks primarily encounter the latter. However, in the context of severe damage, scour poses a more substantial threat to arch bridges, with the probability of damage escalating rapidly once the bridge is overtopped. In conclusion, arch bridges are more susceptible to scour and debris clogging, despite their structural robustness compared to beam bridges, as evidenced by the presence of a moderate damage level. Furthermore, the significance of damage resulting from hydraulic forcing and driftwood impacts on bridges is highlighted. These failure mechanisms are currently underrepresented in existing standards such as EN1991:2005, as discussed in Chapter 2. Therefore, in the next chapter, a novel analytical formulation for deriving fragility curves due to hydraulic forcing and driftwood clogging effect is presented. The framework is also implemented in a software developed by the Author for the purpose.

4. Bridge Deck Vulnerability

In this Chapter, the focus is on examining the impact of hydraulic forcing on single-span bridge decks, incorporating the driftwood clogging effect. A stochastic approach is employed, within an analytic framework, to analyse these effects. The challenges of modelling flood fragility curves are also presented, with an emphasis on the differences in flood treatment within a single or multi-hazard framework. Paragraph 4.1 provides a clarification of the assumptions made and reviews key concepts such as hydrodynamic coefficients and driftwood blocking probabilities. The stochastic vulnerability analysis is introduced within § 4.2, including the definition of limit states and the determination of the bridge's conditional probability of failure. Paragraph 4.3 presents the automatization of HEC–RAS. The methodology is applied to a case-study bridge and discussed in Chapter 5.

4.1. Assumptions of the Proposed Method

In this Paragraph, a detailed illustration of the assumptions underlying the proposed method is presented. A detailed discussion on essential concepts such as hydrodynamic coefficients and driftwood blocking probability is also included. The analysis enhanced the understanding of how these factors contribute to the definition of fragility curves.

4.1.1. General Assumptions

The proposed model investigates the relationship between bridges and the riverine environment, according to specific assumptions. Firstly, the focus of this study is solely on the bridge's superstructure, deliberately excluding considerations of scour effects on piers and abutments. As such, the processes involving erosion are deemed out of the present scope of the work.

Secondly, in the simulations, the bridge is represented as a rigid body, drawing inspiration from the approach usually employed in flume experiments (Oudenbroek *et al.*, 2018). This simplification allow to streamline the analysis and keep the outputs under control, without introducing additional uncertainties given by the structural response, as a field validation was not possible to perform.

Then, the failure event is determined using a Boolean metric, with the limit states domain arising from the assumption of unknown or absent bearings. This hypothesis often follows actual bridges having a single span where bearings do not have shear keys and/or lateral restraints, which introduce further safety margin against the dragging of the deck (Sassu, Giresini and Puppio, 2017).

Lastly, the hydraulic analysis primarily relies on a 1D HEC–RAS model. However, when dealing with intricate river geometries and significant flow deviations from prevalent 1D dynamics, a more sophisticated modelling must be used, given the possibility of implementing a 2D analysis within HEC–RAS itself. Another important aspect concerns the driftwood clogging simulation, as it should be avoided using a 1D model for wood logs accumulation due to the complex interaction between driftwood and the deck. Therefore, in this study, reliable blocking probability estimates are derived from data obtained through actual flume tests, as outlined in § 4.1.3.

The choice between using a 1D or 2D analysis is also influenced by the availability of data for representing the river geometry. For instance, if data from lidar surveys is accessible, it can provide more comprehensive information compared to the traditional cross-section field survey. Nevertheless, the framework's architecture remains unchanged regardless of the flow representation chosen. Eventually, these assumptions provide a robust foundation for evaluating the bridge's vulnerability in response to interactions with the riverine environment. The next paragraphs provide further details on how the hydrodynamic coefficients and the driftwood blocking probability are computed.

4.1.2. Description of Hydrodynamic Coefficients

Hydraulic forces acting on a bluff body when submerged or partially submerged can be classified into static and dynamic components. The static component on the deck can be assessed by considering the water elevation, which allows for the separation of these two components. Subsequently, the dynamic portion can be further broken down into horizontal and vertical components, denoted as 'drag' (F_D) and 'lift' (F_L) respectively, as depicted in Figure 23. Additionally, a moment (M_{cg}) is considered to account for the distance between the line of action of the force and the centre of mass of the body.

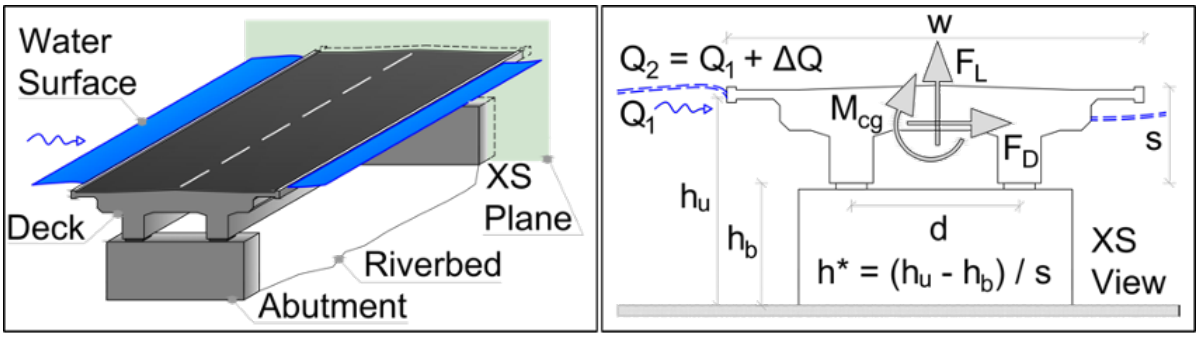


Figure 23. On the left side are the elements of the Bridge Deck, and on the right side is a schematic representation of the forces in a cross-section (XS) view. For clarity, it is omitted the depiction of river embankments, wing walls, and approach ramps, which are meant to be located adjacent to the bridge abutments. The Inundation Ratio is indicated as h. Water discharges are represented by Q_1 and Q_2, while h_u and h_b symbolize the water and deck elevation, respectively. The deck thickness is denoted as s, the width as w, and the bearing distance as d*

The ratio between the force (F_i) and the kinetic energy density, represents the hydrodynamic coefficient (C_i) as per Equation (8).

$$C_i = F_i / 0.5 \rho_w V_u^2 A \tag{8}$$

In which $i = \{D, L\}$ denote respectively drag and uplift, and ρ_w is the density of water, which can fluctuate because of turbidity of the flow. The upstream approach water velocity is indicated as V_u, while A is the body's projected area towards F_i. The moment coefficient is expressed through Equation (9), where M_{cg} represented the moment computed with respect to the deck's centre of gravity and accounted for the overturning of the bridge's superstructure. The remaining geometric parameter, w , symbolises the deck's width.

$$C_m = M_{cg} / 0.5 \rho_w V_u^2 A \cdot w \tag{9}$$

Studies investigating hydrodynamic actions have resulted in formulations that have been incorporated into standards and guidelines. These include Eurocode (CEN, 2005a), FHWA Report HRT-09-028 (Kerenyi, Sofu and Guo, 2009), AASHTO (AASTHO, 2012) CIRIA Manual (Kirby *et al.*, 2015) and AS5100 (Committee BD-090, 2017). Notably, there are differences among these codes concerning the coefficients related to hydrodynamic forces. Indeed, one notable advantage of using AASHTO or Eurocode over FWHA and AS5100 lies in their practicality of application, given the constant drag coefficient with the water elevation, as well as the absence of uplift and overturning components. However, simpler formulations may present certain challenges. For example, how to compute the increased thrust on

foundations caused by negative uplift force on partially submerged decks when no uplift coefficient is given. To this regard, additional tools should be provided, addressing the problem of quantifying the relevance uplift and overturning mechanisms for each bridge design or typology (Tubaldi *et al.*, 2017). Several multi-hazard frameworks have incorporated drag actions (Li *et al.*, 2020). However, most approaches for deriving flood fragility curves do not consider variable hydrodynamic coefficients. This is because hydrodynamic coefficients do not steadily increase with water levels, and as a result, the critical condition may arise for discharges that are lower than the standard 200-year return period. In this study, the FHWA Report HRT-09-028 results are used because Kerenyi *et al.* (2009) utilized CFD simulations to extend the range of tested conditions and reproduce their experimental results. They provide drag, lift, and moment coefficients as functions of the inundation ratio (h^*), which is calculated as the difference between the water's free surface and the bridge clearance, divided by the deck thickness, as per Figure 3 and Equation (1). According to Kerenyi *et al.* (2009), the drag coefficient initially takes values around 2 for $h^* \approx 0$, and it decreases up to $h^* \approx 0.8$, which corresponds to the point of incipient deck overtopping. After that, the drag coefficient starts to increase, reaching around 2 for $h^* \geq 1.5$. While the drag coefficient is always positive, the lift coefficient exhibits negative values (for I-girder decks), acting as a stabilizing force. It reaches values of about -1.5 at $h^* \approx 0.9$ and then approaches zero for $h^* > 3$. The moment coefficient is negative in the interval $0.25 < h^* \leq 1.5$, indicating a counter-clockwise rotation of the deck, as per Figure 23. Conversely, for $h^* \geq 1.5$, the moment coefficient exhibits an opposite behaviour. It is essential to note that different curves exist concerning the bridge width, w, as it influences the water profile beneath the lowest deck chord and consequently affects the applied forces.

4.1.3. Description of the Driftwood Clogging Probability

The clogging of driftwood at bridges can be considered a stochastic process influenced by various factors. Recent experiments have provided valuable insights into this process, including equations proposed by Schalko *et al.* (2018) to estimate the backwater rise caused by LW. Several test campaigns have reached a consensus on the most significant factors affecting the clogging process, namely, the congestion of wood logs during transport, low freeboard at bridges, and decks with exposed structural elements featuring sharp edges (De Cicco *et al.*, 2020). While De Cicco *et al.* (2018) have extensively studied the clogging process at bridge piers, less attention has been given to log entrapment at bridge decks. Two studies have addressed this issue, focusing on the clogging probability of single and multiple logs. Categorical probabilities are employed to quantify the likelihood of clogging. The research of

Schmocker and Hager (2011) parameterized the clogging probability based on bridge (B) and log (L_L) lengths, log diameter (D_L), and flow depth (h). Interestingly, the orientation of driftwood does not significantly affect the clogging probability when the bridge deck is the only obstacle, unlike the scenario observed at piers. The probability of clogging for a single log is computed as:

$$P_M/P_{LM} = -0.074 + 0.88\, L_L\, (h + 0.5D_L)/BH \tag{10}$$

Where the bridge clearance is denoted by H. The maximum clogging probability tested at three different relative flow depths ($h/H = 0.9, 1.0, 1.07$) is represented by P_{LM}. The approach used in this framework involves a variable water level, while Equation (10) allows the assessment of the blocking probability only at the specific relative water stages $h/H = \{0.9, 1.0, 1.07\}$. Despite an interpolation can potentially be applied, the overtopping phenomena typically exceeds $h/H = 1.07$, as evidenced in Chapter 5. As a result, an extrapolation of results can introduce additional uncertainties and it is therefore not taken into consideration. This restriction is absent in the work carried out by Gschnitzer *et al.* (2017). In their study, the authors use logistic regression to calculate the clogging probability of logs, considering seven predictor variables: (i) h/H (relative flow depth), (ii) the channel gradient, (iii) the transport condition of driftwood, which can be either in single or congested logs, (iv) L_L/B (log to bridge length ratio), (v) the logs' smoothness, (vi) single or multi-span bridges, (vii) a possible baffle to be installed on the upstream side of the deck. Hence, the driftwood blocking probability according to Gschnitzer *et al.* (2017) is:

$$P = 1/\left(1 + e^{-(\beta_1 x_1 + \beta_2 x_2 + \cdots + \beta_7 x_7)}\right) \tag{11}$$

Each regression coefficient, denoted by β_i , is associated to a predictor variable, termed as x_i. Upon comparing the regression equations, the one derived from Gschnitzer *et al.* (2017) indicates a lower clogging probability for h/H values greater than 0.95. This comparison is made using the reference case-study presented in the paper by Schmocker and Hager (2011). However, due to limitations in the h/H values employed in the research of Schmocker and Hager (2011), a single-setup comparison is used. Interestingly, a 18% gap in blocking probability is observed when applying Equation (10) and (11) using the following parameters: $Fr = 0.8, h/H = 1, L = 10\ m, B = 9.5\ m, D_L = 0.5\ m, H = 2.3\ m, i = 0.07$. Schmocker and Hager (2011) report a single log blocking probability of 0.48 using their formulation, whereas the formulation of Gschnitzer *et al.* (2017) yields 0.39, representing an 18%

difference. Consequently, in this study, Equation (11) is utilized to characterize the clogging process, primarily due to the broader range of tested h/H values. Additionally, when investigating driftwood with branches, it reveals that the clogging probability increases up to 0.85, signifying a 54% increment. While the impact of branches is measurable, research on wood density and its buoyancy is still evolving. Previous studies by Ruiz-Villanueva *et al.* (2016) report wood densities ranging from $600\ kg/m^3$ ($\pm 200\ kg/m^3$) to $800\ kg/m^3$ ($\pm 170\ kg/m^3$), with corresponding buoyancy levels spanning from 18-30% for green wood, which is denser than the instream one, reported to be the range 25-44% (Ruiz-Villanueva *et al.*, 2016). For the specific setup discussed earlier ($D_L = 0.5\ m$), these values result in 9 cm to 22 cm as emerging portion. Considering the measurement of wood density is beyond the scope of the work from Gschnitzer *et al.* (2017), it is judged more appropriate to consider wood logs with the lowest rising height, to be on the conservative side. Additional details are provided in Chapter 5.

4.2. A Novel Approach to Bridge Deck Fragility Analysis

The methodology is depicted in Figure 24. The process begins by using HEC–RAS – commonly used software by practitioners – to define the hydraulic model. The hazard can be characterized using an established hydrologic model and gauge station statistics (Ercolani and Castelli, 2017). Subsequently, the hydrodynamic coefficients are computed at each water stage, while iteratively increasing the discharge. Stochastic parameters are considered based on the degree of knowledge of the investigated bridge. Then drag, lift, and overturning limit states are computed. Fragility curves are then derived through Monte Carlo simulations. Analysing clogging scenarios necessitates updating previous tasks, specifically iteratively modifying the HEC–RAS bridge geometry to simulate the accumulation of logs against the bridge deck. This simulation involves the gradual lowering of the bottom chord of the girder during each iteration to mimic the effect of entrapped driftwood, which simulates an increment of the deck's thickness. For each distinct geometry, a new fragility curve is generated, and the failure path is confined within a three-dimensional space comprising failure probability, discharge, and amount of accumulated driftwood (cross-sectional increased blockage). Automated routines employed to control HEC–RAS are based on the work of Goodell (2014), adapted to the Python language as showcased in the study conducted by Dysarz (2018). Additionally, the Python scripts developed in this work are also written in Visual Basic for Application (VBA) for comparison and validation purposes. The detailed explanation of the method is

presented in § 4.2.1, while § 4.2.2 explains the limit states, and § 4.2.3 outlines the procedure for obtaining the fragility curves.

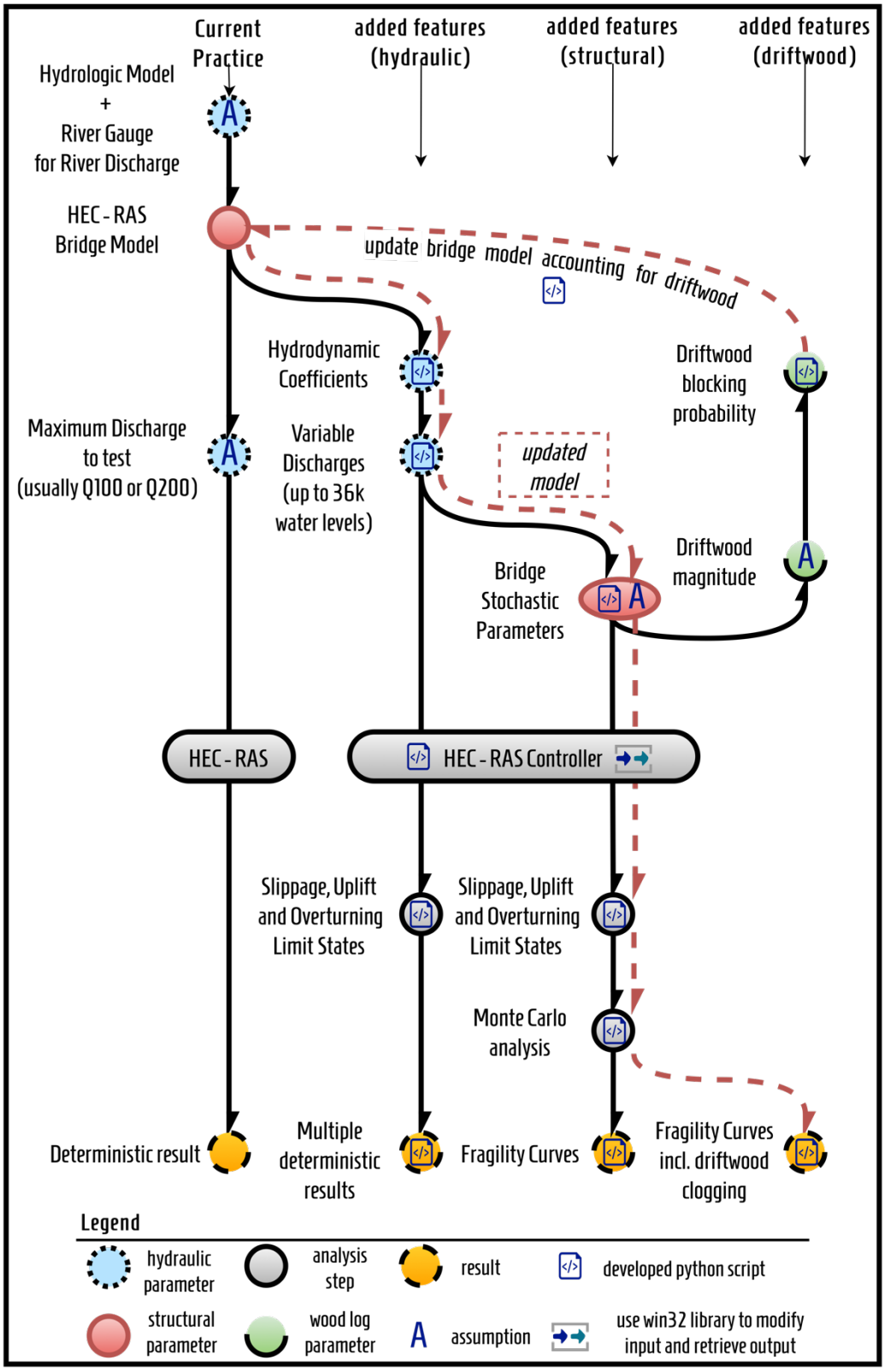


Figure 24. Method's workflow to obtain fragility curves from a HEC-RAS bridge model

4.2.1. General Overview of the Novel Approach

The framework presented in Figure 24 is specifically applicable to single span bridges and is founded on the assumptions detailed in § 4.1. The failure mechanisms take into account sliding, uplift, and deck overturning events observed during real floods – as per Chapter 3 – and flume experiments, as documented by Oudenbroek *et al.* (2018). Stochastic variables are linked to a previously validated survey methodology, which was tested on 71 bridges (Pucci *et al.*, 2019).

In the case study described in Chapter 5, uncertainties arise with regard to the deck weight due to the unavailability of original design sheets and potential measurement errors. To address this, literature data is employed to probabilistically characterize the deck weight based on the span length, bridge material, and typology, following the insights provided by Petrangeli (1996). This uncertain parameter, which strongly depends on design practices and codes adopted at a country level is derived from the work of Petrangeli (1996) for an Italian site.

To incorporate the uncertain deck weight in the limit state equations, a Monte Carlo simulation is utilized. Subsequently, for each water depth, the flow velocity, discharge, Froude number, and the associated hydrodynamic coefficients are computed based on the sampled values from the Monte Carlo simulation. Then, the overall hydraulic loads acting on the bridge can be assessed.

The hazard return period remains unaffected by the progression of the framework due to the utilization of variable water depth obtained through the combined use of HEC–RAS and Python. This integration enables the computation of the hazard curve separately from the hydraulic simulations. The approach employed in this methodology may be understood as a lookup table, where simulations are executed only once. To illustrate this point, an example may be considered where discharges are computed from $1\ m^3/s$ to $500\ m^3/s$ in increments of $0.1\ m^3/s$, resulting in a total of 4990 HEC–RAS flow stages for analysis. The Python scripting facilitates running these simulations in a single process.

Apart from the HEC–RAS computations, based on the results obtained from a chosen hydrologic model, it is determined that a 200-year return period flood corresponds to a discharge value of $250\ m^3/s$. However, when additional factors like climate change effects are incorporated into the hydrologic model, an altered discharge value may be attributed to the same mean annual exceedance frequency; for instance, it could be $275\ m^3/s$. Nonetheless, the entire hydraulic simulation remains valid, as the new discharge value ($275\ m^3/s$) lies within the range of previously simulated flow stages ($1\ m^3/s\ -500\ m^3/s$).

This separation of the physical model from the probabilistic hazard characterization yields increased cost-effectiveness for the methodology. By utilizing the lookup table-like approach and performing simulations only once, the computational efficiency is significantly enhanced, allowing for more practical and cost-efficient hazard assessments.

Thus, the probability of failure is subsequently calculated as:

$$P_f = P(\, g(x) \leq 0 \mid h^* = h_i^* \,) = \left[\left(\sum_{c=1}^{N_{tot}} N_c \right) \Big/ N_{tot} \right]_i \tag{12}$$

The limit state function is termed $g(x)$ in a generic structure, h_i^* is the i-th inundation ratio (Figure 3), for $i = \{0, 1, \dots, n\}$, where n is the number of simulated flow discharges, h_{ui} the water stage upstream the bridge, h_b the clearance and s the deck thickness. $N_c = 1$ if $g_k(x) < 0$ (corresponding to the failure of the bridge), while $N_c = 0$ if $g_k(x) \geq 0$. N_{tot} and N_c are the total and the generic simulations' number, for a fixed h_i^*.

The fragility curve is determined using the maximum likelihood method, which involves fitting the probabilities derived from Equation (12) across all the tested discharge ranges (see § 4.2.3). HEC–RAS simulations are conducted under a steady-flow regime, as the hydrodynamic effect is assessed using Equations (8) and (9). The current methodology is specifically designed for single-span bridges, as the presence of a pier in conjunction with driftwood can be simulated using the existing dedicated tool within HEC–RAS. However, the software's capabilities currently lack the ability to model the clogging process on single-span decks. To address this, the method is repeated for various bridge geometries while accounting for the driftwood effect. In a worst-case scenario, this effect is equivalent to lowering the bottom chord of the upstream face of the deck. As a result, the driftwood clogging represents a sequential damage state.

4.2.2. Computation of Limit States (LS)

The limit states (LS), represented by $g(x)$, are formulated as equations of supply $s(x)$ subtracted from demand $d(x)$, applied to the deck system shown in Figure 23. The streamflow force acting on the deck has an unknown direction, and it is therefore necessary to include both hydrodynamic forces and an additional moment. As discussed in § 4.1.2, the hydrodynamic coefficients can take on both positive and negative values to account for different thrust directions. For instance, the uplift force is commonly assumed to have a positive upward direction, but during the initial stages of partial

submersion of the deck, the corresponding coefficient, C_L, assumes a negative value (Kerenyi *et al.*, 2009). This indicates a downward force, resulting in increased normal force on bearings and foundations. This dynamic component is connected to the static one.

Thus, the failure of the deck results from the interaction of both static and dynamic discharge components, leading to three potential failure mechanisms: (i) the unseating of the girder through a sliding mechanism (drag), (ii) the uplifting of the deck due to the interaction of buoyant and dynamic uplift forces, and (iii) the overturning of the deck caused by an uneven distribution of drag and uplift forces relative to the deck's centre of gravity. These LSs are considered simultaneous since the equations take into account both the static and dynamic aspects of the flow, as further evidenced during the derivation of fragility functions. The equations for drag, uplift, and overturning are defined according to Equations (8) and (9) provided in § 4.1.2. Within these equations, the drag, lift, and moment components are represented as F_{Di}, F_{Li}, M_{cg}, respectively, with the subscript i ranging from 1 to n_Q, where n_Q denotes the number of flow profiles set in the HEC–RAS simulations. The occurrence of the slippage mechanism, denoted as S_{Lij}, resulting from sliding at the bearing interface, is expressed by Equation (13), where j varies from 1 to n_{MC}, and n_{MC} represents the number of iterations performed by the sampling algorithm in the Monte Carlo analysis.

$$S_{Lij} = H_{ij} - F_{Di} - 0.5\,\rho_w\, g \cdot\, wetUP_i^2 + 0.5\,\rho_w\, g\, \cdot wetDN_i^2 \tag{13}$$

The wetted portions of the bridge deck are indicated as $wetUP$ and $wetDN$, g is the constant of gravitational force and the horizontal capacity against deck unseating is H_{ij}, calculated according to Equation (14).

$$H_{ij} = \mu\left(Fz_i - F_{Li} - B_{RFi} - B_{Ti} - \frac{M_{cgi}}{d} + \frac{B_{Ti}w}{6}d\right) \tag{14}$$

At the girder's interface the coefficient of friction is indicated as μ, while the components of buoyancy are indicated as B_{RFi} and B_{Ti} and defined according to Equations (16) and (17). The distance between bearings is indicated as d, according to Figure 23, the deck's width and weight are denoted respectively as w and Fz_i.

$$Fz_i = G_{sqm}L_d w_d\ + s_{cls}L_d w_d \rho_{cls} \tag{15}$$

The steelwork tonnage $[kgf/m^2]$ and the volume of concrete per square meter of deck's surface $[m^3/m^2]$ are indicated as: G_{sqm} and s_{cls} . These values are taken from existing works , given a certain span length range and structural typology (Petrangeli, 1996).

For the mentioned parameters, a normal distribution is hypothesized. The remaining terms represent the density of the concrete ρ_{cls}, and the transversal and longitudinal dimensions of the deck, respectively L_d and w_d.

Due to the different water elevations upstream and downstream the bridge, the hydrostatic thrust may assume – in the most general case – a trapezoidal distribution. Therefore, it can be split into a rectangular and triangular distribution. These are termed respectively B_{RF} and B_T as per Equations (16) and (17) respectively.

$$B_{RF} = \rho_w \, g \, w \, wetDN \tag{16}$$

$$B_T = 0.5 \, \rho_w \, g \, w \, (wetUP - wetDN) \tag{17}$$

The final addition to Equation (14) accounts for the moment exerted on the deck's centre of gravity resulting from the triangular distribution of buoyancy. The uplift mechanism occurs due to the algebraic sum between the deck's self-weight and the combined dynamic and static components of the hydraulic force. Another underlying assumption is that no vehicles are present on the bridge at the time of failure. However, past disasters have shown that this assumption is not always met (Puppio, Novelli and Sassu, 2018). Nonetheless, considering additional loads from vehicles, it would lead to less conservative predictions of collapse probability due to the added resistance against uplift. It is therefore hypothesized no live loads on the bridge deck. This assumption is also maintained for the overturning limit state. The uplift limit state is evaluated using Equation (18).

$$U_{\mathrm{Pij}} = Fz_j - (F_{Li} + B_{RFi} + B_{Ti}) \tag{18}$$

The overturning mechanism takes place when the entire deck rotates under the influence of water thrust. This rotation is a result of the moment generated by the water thrust and its distance from the deck's centre of gravity (cg), as depicted in Figure 23. In line with findings from earlier research (Jempson, 2000; Oudenbroek *et al.*, 2018), it is assumed that the rotation occurs around the rightmost bearing, with the water flowing from left to right, as illustrated in Figure 23.

The distance measured vertically between the deck's centre of gravity and the lower chord of the girder h_{cg} is computed at each simulation ($j = \{1, \dots, n_{MC}\}$). Therefore, h_{cg} is evaluated by calculating the static moment of the deck concerning the lower girder chord. This calculation is necessary since the weight distribution varies with each iteration (up to n_{MC} times) in the Monte Carlo procedure. Conversely, the horizontal distance L_{cg} between the rotation point at the rightmost bearing and the centre of gravity is assumed to remain constant, considering that decks are typically symmetric to the x-z plane. The overturning moment is then given by Equation (19).

$$O_{\mathrm{Vij}} = Fz_j L_{cg} - (F_{Li} + B_{RFi} + B_{Ti})L_{cg} + F_{Di}h_{cgi} - M_{cgi} + \frac{B_{Ti}w}{6} \qquad (19)$$

4.2.3. Fragility Analysis

A fragility curve (FC) is defined, in accordance with Equation (20), as a cumulative distribution function that portrays the probability of failure for a particular structure or the likelihood of exceeding a specific limit state (LS). In this research, the fragility curve is calculated as the conditional probability of surpassing a specific damage state (DS) when a particular magnitude of the hazard, im_i, is encountered.

$$P[\, DS \geq ds_k \mid IM = im_i \,] = \Phi\left(\frac{\ln(q_i/\mu_k)}{\beta_k}\right) \qquad (20)$$

The discharges q_i are considered in the HEC–RAS simulations, with IM denoting the river discharge and ds_k representing the damage states associated with the three limit states, $k = \{1, 2, 3\}$, outlined in § 4.2.2. In this study, failure is treated as a Boolean event in Equation (12), making the associated probability categorical. To obtain the probabilities of failure, FCs are parameterized using a lognormal distribution, with μ_k and β_k representing its mean and standard deviation, respectively.

LSs are computed using Equations (13), (18) and (19), and their outputs are incorporated into Equation (12). The FC is then fitted to the observed probability of failure using the maximum likelihood method (Baker, 2015). Ultimately, the final fragility curve is derived from Equation (20).

The connection between the collapse probability and the return period can be established by integrating the joint probability density function, while taking into account that $p(Q) = 1/T_r$, as:

$$P(DS \mid Tr) = \int p(DS \mid Q)p(Q)dQ \tag{21}$$

$$T_r(Q) = C_1 e^{C_2 Q} \tag{22}$$

In these equations, $p(DS|Q)$ represents the probability density function of fragility, while C_1 and C_2 are two constants determined based on extreme-value distributions using historical discharge data from river gauge stations (Herschy, 2019). Consequently, the hazard's annual exceedance frequency can be recalculated not only using actual river flow data but also considering potential future trends.

To incorporate the impact of driftwood, the entrapment probabilities $p(D)$ and new HEC–RAS geometries are taken into account. The fragilities associated with the updated bridge geometry are denoted as conditional probabilities $p[DS|Q^*]$, where $Q^* = f(Q, D, h)$ depends on the river discharge, driftwood dimensions and bridge geometry. This function is implicitly accounted for when integrating the hydraulic model with the inputs derived from the driftwood model and the rainfall events (i.e., hydrologic model). In such cases, the fragilities consider driftwood occurrence as a certain event, i.e., $p(D) = 1$, while $p(D)$ shows that the blocking probabilities are mostly below 1 for most events (see § 4.1.3). Thus, to incorporate the marginal $p(D)$ within the updated fragilities, the following equation is employed:

$$P[\, DS \geq ds_k \,,\, D = d_m \mid Q^* \,] = \frac{\left(p(DS,\, D = d_m \cap Q^*)\right)}{\left(\int p(DS,\, D = d_m \cap Q^*) dQ^*\right)} \tag{23}$$

$$P(\mathrm{DS}, \mathrm{D} = \mathrm{d_m} \cap Q^*) = p[DS^* \mid Q^*]\, p(Q^*) \;\wedge\; p(Q^*) = p(D|Q) = p(D) \tag{24}$$

Since the driftwood blocking probability is not a function of the flow discharge, $p(D)$ and $p(Q)$ are independent events, as per Equation (24). Therefore, Q^* can be replaced with Q, due to the fact that the modified bridge geometries are analysed using the same range of discharges. Furthermore, the hydraulic and structural models already account for the modified geometries for every clogging scenario. Hence, $p(DS^*|Q^*)$ incorporates the consequences of having lowered the upstream side of the bridge deck. Indeed, DS^* pertains to d_m, which represents the clogging event. In all the equations, the subscript k identifies the three LS – overturning, slippage and uplift. Employing Equation (23), a new set of FC is derived and can be plotted for each k-th mode of failure in the Failure Probability – Discharge – Blockage Ratio space. The definition of Blockage Ratio can be found in Equation (4). For each mode of failure,

sequential probabilities in Equation (25) are evaluated. The occurrence probability of changes in the driftwood clogging upstream of the bridge deck is assessed for a given LS (i.e., fixed d_k) to understand the influence of entrapped logs in succession.

$$P[\,DS = d_k, D = d_m \mid Q\,] = \tag{25}$$

$$= P[\,DS \geq d_k, D = d_m \mid Q\,] - P[\,DS \geq d_k, D = d_m + 1 \mid Q\,]$$

4.3. Automating HEC–RAS

The proposed approach is embedded in a computer program called BrHyD (Bridge Hydraulics and Driftwood) developed by the Author. The software can help to analyse the hydraulic vulnerability of bridges, also including driftwood effects. The program is able to control HEC–RAS through the use of win32com library together with the native HEC–RAS APIs. In this specific application, the HEC–RAS Controller API is used, as displayed in Figure 25.

Concerning the win32com library, it allows to call a HEC–RAS API because HEC–RAS is an application in a Windows environment that was designed as a Component Object Module (Goodell, 2014). Therefore, BrHyD works as a client program designed to use not only the routines and functions of HEC–RAS Controller, but also implementing own routines and functions to extend the capabilities of HEC–RAS. For example, optimization and probabilistic analyses uses as inputs the outputs from HEC–RAS and through Python packages generates more elaborate outputs, such as fragility curves.

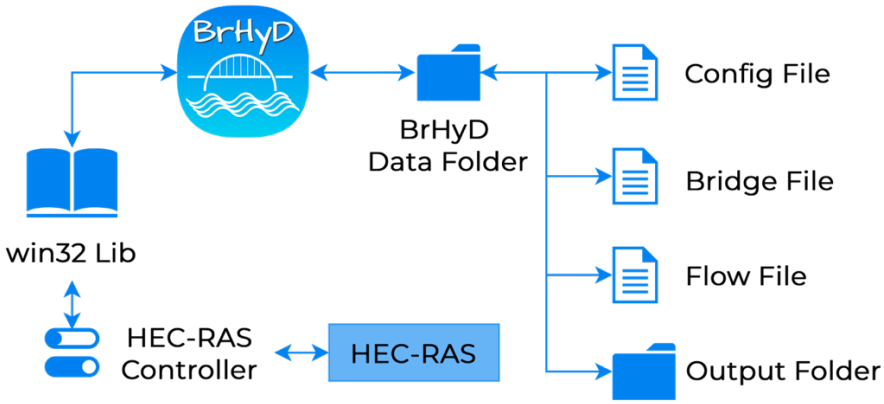


Figure 25. Scheme of the BrHyD program's functioning

Once installed, BrHyD creates a Data Folder in the main user directory; inside the folder, it generates three files and the output folder. The configuration file contains the necessary information concerning the link to a specific HEC–RAS Project, Plan and Flow. The bridge file holds the relevant information concerning the investigated structure, as displayed in Figure 26, while the Flow file stores the discharge values to be prompted by the user. Notably, the flow file of BrHyD it is not a copy of the HEC–RAS one, because it is designed to memorize different information and in a different way (it does not use the 8-bit parsing scheme).

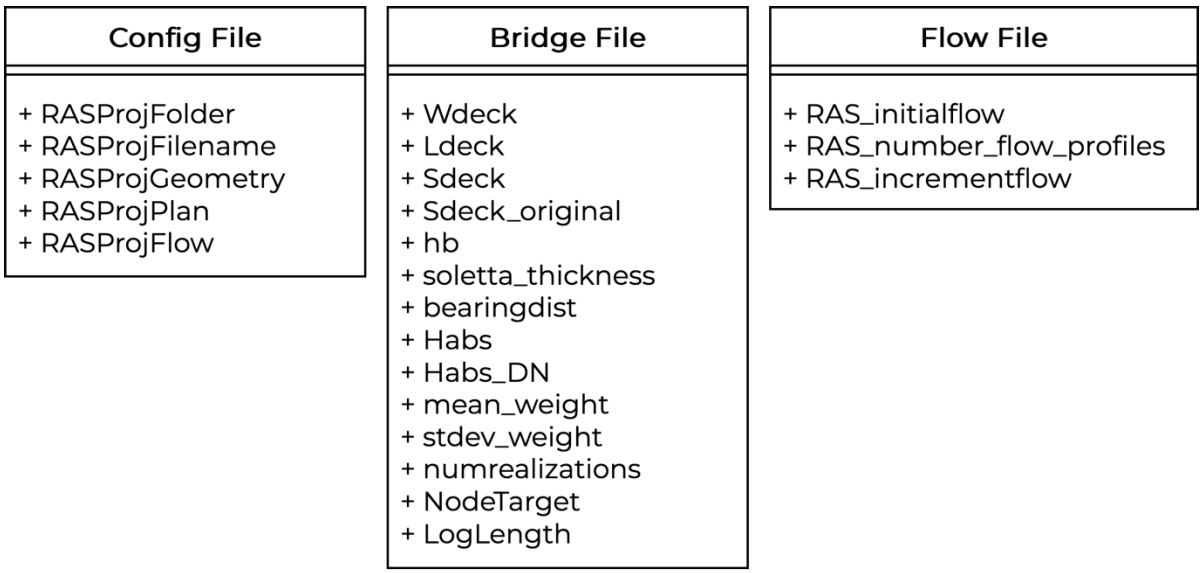


Figure 26. Content of the files needed for the BrHyD execution

The program offers the possibility for a GUI as per Figure 27. The GUI reveals many of the BrHyD's functionalities, which can be divided into three main groups: (i) Performing hydraulic analyses in batch or single-value through HEC–RAS; (ii) Study the effects of driftwood clogging on bridge decks, a functionality that is not yet implemented in HEC–RAS; the key-feature is the usage of actual flume experiments results rather than a fully analytical framework; (iii) The generation of fragility curves for single-span bridge decks accounting also the driftwood blocking probability obtained from actual flume tests.

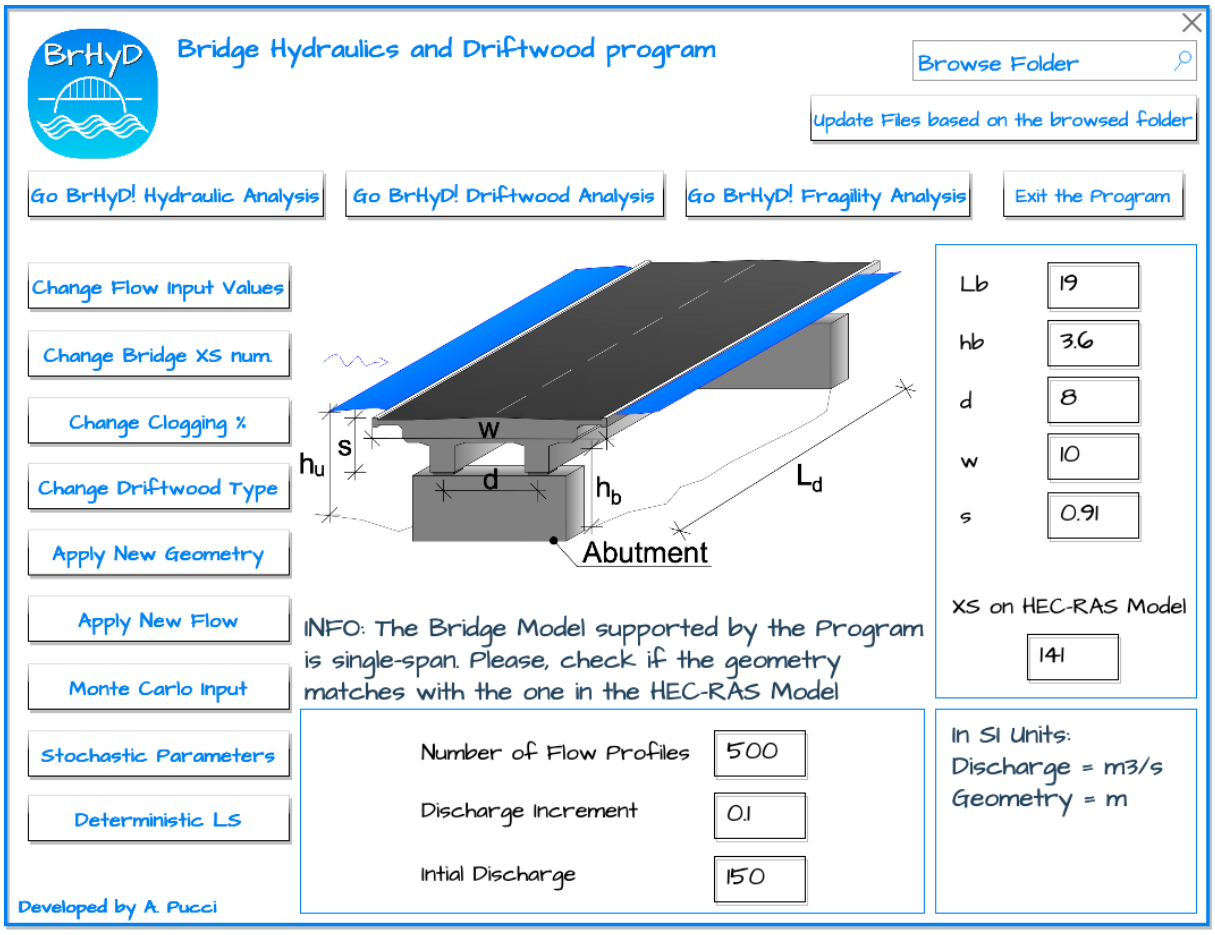


Figure 27. BrHyD GUI

In addition, the user is able to modify parameters of an existing HEC–RAS model up to a certain extent. Specifically, BrHyD can operate on existing RAS plans, flows and RAS geometry files. Concerning the first, based on existing RAS plans, the user can choose between them, allowing to perform multiple analyses using different setups. In addition, within each plan, the user can modify the flow values (within the RAS Flow file) that are inputted to HEC–RAS. This feature allows the user to simulate in a single HEC–RAS run up to 36 000 water discharges. The upper boundary for this number is specified by HEC–RAS. The time needed to perform batch hydraulic is just a function of the complexity of the HEC–RAS model and the capabilities of the computer's hardware. The units of numerical values prompted in BrHyD must be coherent with the HEC–RAS Project selected; otherwise the program could not (yet) understand whether the discharge is provided in m^3/s rather than in cfs. The program can also modify the geometry of a bridge to simulate the clogging mechanism, as well as to compare between different design options. In addition, BrHyD can not only input values to HEC–RAS but also retrieving outputs from specific XS; i.e., the upstream and downstream XS of a bridge. This feature allows in the specific application, to use the XS output table values to compute the hydrodynamic coefficients. In the current version of the program, the equations based on the work of Kerenyi *et al.* (2009) are implemented, although the code

is already under development for considering also the values proposed in other works, such as those of Jempson (2000) and Dean (2020).

Concerning the driftwood analysis, it is calculated according to the work of Gschnitzer *et al.* (2017); the parameters of the logistic regression can be modified to simulate different scenarios and, therefore, obtaining different blocking probabilities. In particular, the effectiveness of mitigation strategies can be implemented.

The program also allows to include driftwood of different dimensions. However, the approach uses data from driftwood clogging experiments. It is therefore recommended to use only the dimensions within the tested range of wood logs.

BrHyD is developed using Python language, as already mentioned, but also a VBA-based version of the program is complied, which comes in a self-installing .exe package. However, the VBA-version of BrHyD has less features as the Python's one. Nevertheless, both software are employed to validate the method, when computing the LS. This is achievable with VBA because a linearization of the failure domain around the zero of each failure domain is performed.

5. Bridge Deck Fragility Analysis Application

The proposed approach described in Chapter 4 is implemented for a bridge, taken as case-study, situated in the Municipality of Carrara, Tuscany, Italy.

5.1. Description of the Region

The Province of Massa and Carrara can be divided into two main geographical regions: the coastal area and the mainland. The coastal plain stretches approximately 4-5 km wide, following a North-West to South-East direction. Towards the eastern part, this plain transitions into the foothills area, characterized by heights below 1000 m. Moving inward, the territory reaches the watershed, where vegetation becomes scarce, and altitudes consistently exceed 1000 m, reaching up to 1950 m above sea level. The internal mountainous region is characterized by steep slopes, and the presence of sub-vertical walls is notable, particularly in areas with carbonate formations. This results in a dramatic transition within a relatively short distance of 10 – 15 km, from a mountainous highland environment to a coastal marine environment.

The watercourses in the districts of Massa and Carrara originate from the Apuan Alps and flow directly to the sea. These watercourses typically have short routes, with a general east-west trend. The upper and middle basins exhibit high slopes, while the low basin, located in the lowland part, has embanked and hanging riverbeds. The natural solid transport within these watercourses is relatively modest, dependent on the geological characteristics of the contributing basins, where debris covers are not extensively present. However, in the past, significant artificial solid transport occurred due to marble processing, involving waste material discharge into the riverbeds and sawing activities (resulting in fine fractions). Currently, the artificial debris contribution has significantly decreased, with natural materials forming the majority of the material reaching the sea, except for the Frigido and Carrione rivers, which still carry notable volumes of material.

The morphology of this region, combined with the interception of humid currents from the Mediterranean and the Atlantic area by the Apuan Alps Mountain range, leads to high annual rainfall, with values reaching up to 3500 mm. These unique conditions, coupled with the steep slopes of the mountain

basins, the presence of debris covers, and extensive human activities, create a general environment of instability and hydrogeological risk.

The Carrione is a river that originates from the Apuan Apls and steeply flows into the floodplain. The watercourse is known for having caused extensive damages along the years to the towns of Carrara, Avenza and Marina di Carrara. At the moment, an extensive plan to reduce the hydrogeologic risk along this watercourse is ongoing. Specifically, the reduction of peak discharge will be obtained through the realization of a series of dams located in the upper part of the watershed. The basin of Carrione – displayed in Figure 28 – is only 46 km^2 wide, but the combination of intensive land use for marble extraction (white spots in the satellite image), urbanisation and climatic shifts, contributed to several disasters. A general overview of past floods that affected the Municipality of Carrara is presented in Table 6.

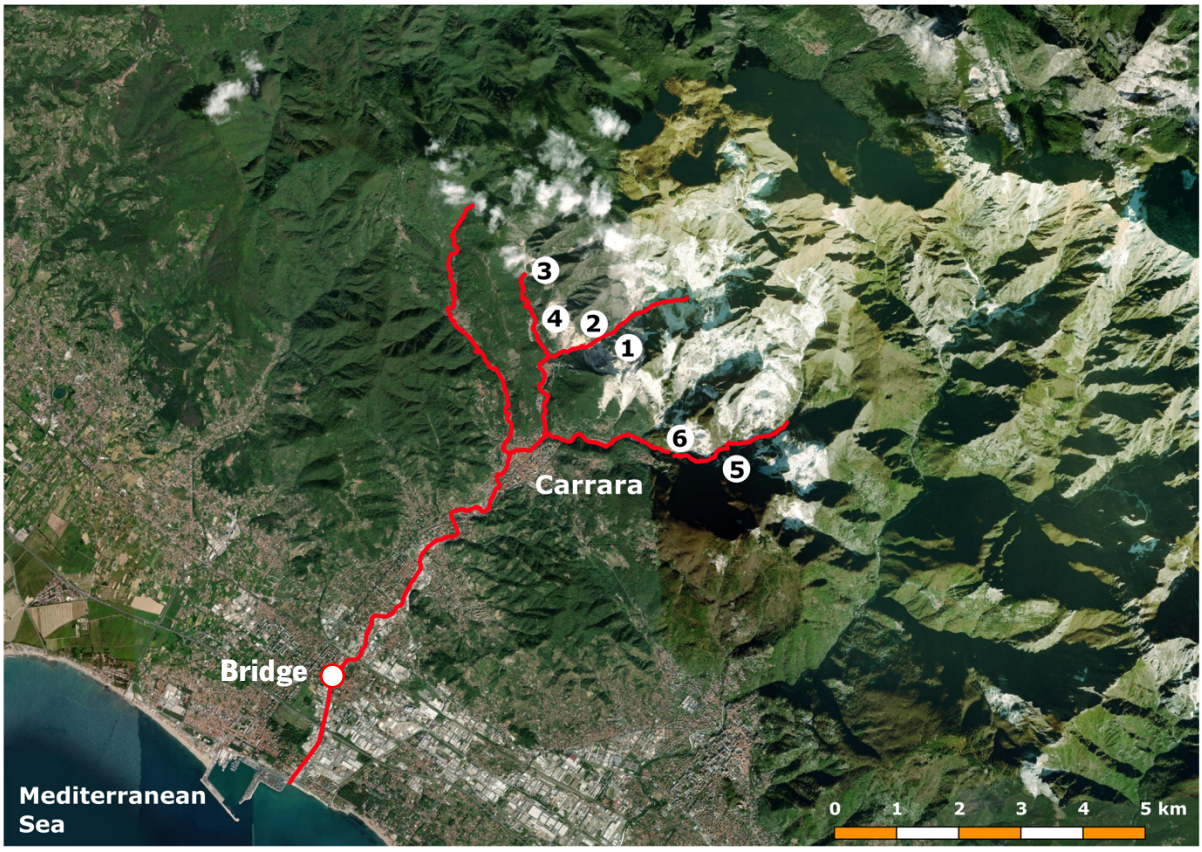


Figure 28. Carrione river, with the location of the six locations of the upper basin that sustained major damages in the 2003 flood. The location of the case-study bridge is also indicated

The costliest event occurred on September 23rd, 2003, where 6 Million EUR were spent just to clean streets from the debris. The total cost of the flood was estimated to be around 304 Million EUR.

The overtopping of the "via Menconi" bridge – highlighted in Figure 28 – caused the inundation of Avenza and Marina di Carrara, affecting 18 000 people. After the 2003 flood, the authorities deemed

necessary to reconstruct the bridge, widening and deepening the river's cross-section by 3.8 and 1.2 m, respectively. The new bridge, which is the subject of this present study, was opened to traffic in 2007. However, recent flood events revealed its inadequate performances due to low clearances, making it susceptible to overtopping. Consequently, in 2021, the owner replaced it.

Table 6. Historical floods in Carrara, concerning the Carrione river

Event	Damages (present value) [M€]	Rain Depth [mm]	Hours of rain [h]
27/10/1949	18.5	230	2 to 3
24/07/1968	15 (estimated)	303.8 (233.8)	24 (6)
16/11/1968	10 (estimated)	No data	No data
24/09/1982	20 (estimated)	200	4
23/09/2003	304	250	24
11/11/2012	24.7	300	24
28/11/2012	11	200	2
05/11/2014	100	200	3

5.2. Description of the Hydraulic Model and the Bridge

The hydraulic study on the lower reach of the Carrione river in 2007, estimated a peak discharge of 425.1 m^3/s for a 200-year return period. However, in 2014, a subsequent study commissioned by Regione Toscana used the MOBIDIC Model developed by Castelli (Castelli *et al.*, 2014) and reported a higher peak discharge of 459.6 m^3/s. After recalibrating the MOBIDIC model, an updated peak discharge of 437.9 m^3/s was determined in 2018 (Castelli, 2018). Therefore, since 2014 the hydraulic model (calibrated on the hydrologic one) highlighted the high vulnerability of the 2007's "via Menconi" bridge, which made it again at risk of overtopping. In addition, the HEC–RAS model evidences that a backwater rise occurrs at the bridge location. This complex interaction of hydraulic phenomena is the main reason behind the decision to investigate further this specific bridge, among the 71 inspected in the previous survey campaign in 2018 (Pucci *et al.*, 2019).



Figure 29. The bridge over the Carrione river taken as case-study. It was built in 2007 and demolished in 2021

The bridge under consideration, displayed in Figure 29, is constructed with a composite steel-concrete deck, where 60 cm tall I-girders are interconnected through studs to a concrete cap with a thickness ranging from approximately 20 to 25 cm. However, the specific design documents detailing the deck's composition were not accessible during the investigation. Consequently, only the overall external dimensions of the deck were available, as obtained from the inspection campaign conducted in 2018 (Pucci *et al.*, 2019). Due to the unavailability of the design sheets, the self-weight of the deck remained unknown. In light of this limitation, it is formulated a hypothesis concerning its self-weight based on the available measurements, structural typology, and the span length of the bridge.

The bridge has a width of 10.4 m and spans a distance of 19 m between the bearings. To address the lack of specific data for the bridge at hand, existing data pertaining to similar bridges is consulted. In this context, the literature provided insights into the steelwork tonnage and the proportion of concrete, which are further guided by the information presented in Table 7 (Petrangeli, 1996).

Table 7. The incidence of concrete and steelwork for composite bridges spanning up to 20 m

	Steelwork Tonnage	**Concrete**
Mean	$250\ kg/m^2$	$0.3\ m^3/m^2$
Standard Deviation	$50\ kg/m^2$	$0.1\ m^3/m^2$

To reduce computational costs, the 1D HEC–RAS model does not incorporate the steel railing as an active component. This simplification results in an underestimation of the blockage effect during the flow transition above the deck. Nevertheless, the lack of consideration for the steel railing becomes consequential when overtopping water forces act in combination with debris, leading to the collapse of the steel parapets even before any of the investigated limit states will occur. In contrast, the reinforced concrete parapets play a crucial role by contributing a fictitious thickness to the deck, which should not be disregarded (Puppio, Novelli and Sassu, 2018).

The bridge shown in Figure 29 is an integral component of a comprehensive HEC–RAS model developed by request of local authority, “Regione Toscana”. The model is made available under license from Regione Toscana, and for further details, additional information can be obtained from the corresponding department, "Direzione Difesa del Suolo e Protezione Civile," at the local authority. The entire stretch of the Carrione River within the floodplain is encompassed in the model. The interactions and influences of all the bridges spanning over the river, including backwater rise effects, are included within the computations using HEC–RAS.

5.3. Application and Results

The hydrologic model employed in this study utilizes MOBIDIC, incorporating two calibrated datasets for the computation of discharge. The hydraulic model utilized is a 1D HEC–RAS geometry, which adequately captures the river's behaviour with satisfactory accuracy. The hydrodynamic and driftwood coefficients essential for the analysis are sourced from FHWA, as documented in the works of Kerenyi *et al.* (2009) and Gschnitzer *et al.* (2017), respectively.

The LS Equations (13), (18) and (19) are formulated based on the rigid-body hypothesis, a concept commonly utilized in hydrodynamic flume experiments (Jempson, 2000; Picek *et al.*, 2007; Kerenyi *et al.*, 2009; Dean, 2020). These equations hold true when no lateral restraint systems are in

place. However, if lateral movement is restricted, such as through the use of shear keys, a shear failure mechanism needs to be considered.

In the case of the actual bridge, the presence and characteristics of installed bearings, which could potentially act as lateral restraints, could not be determined. Consequently, only Equation (13) may not accurately represent a possible failure mechanism for the real structure. Nevertheless, despite this uncertainty, the framework's validity can be demonstrated using this dataset, which offers the distinct advantage of a calibrated hydrologic and hydraulic model.

Various setups are examined using BrHyD, the developed software presented in Chapter 4. This tool enables interaction and modification of inputs related to HEC–RAS geometry and flow, incorporating a probabilistic model as well. Concerning the setup for the case-study bridge, intervals of 150 m^3/s and 600 m^3/s are chosen as initial and final discharges, respectively, with an increment of 1 m^3/s. The values are selected to strike a balance between accuracy and computational cost for the specific case-study.

The HEC–RAS outputs provide water stages and velocities for both upstream and downstream cross-sections of the bridge. Subsequently, for each HEC–RAS discharge step, a Monte Carlo analysis with 20 000 simulations of bridge weights is conducted. LS computation and the generation of fragility curves are performed in line with Equations (13), (18), (19) and (20), respectively.

Given that hydrodynamic coefficients are subject to variations with water stages and velocity, their values are calculated for each HEC–RAS output table. This results in a total of 9 million unique combinations of deck weight and river discharge, which serves as input for the limit states computation.

To manage computational costs, a linearization approach is applied to the three failure domains near the zero of each limit state function, and only this specific value is recorded in the output file. To ensure accuracy and consistency in results, the entire procedure is cross-validated using BrHyD developed with python and the analogous software but coded with VBA, within the current range of tested flows. The parameters of the fragility curves are summarized in Table 8, providing mean and standard deviation values. Then these parameters are employed to obtain Figure 30.

Table 8. Fragility curves parameters without the driftwood effect

Limit State	**Mean [m^3/s]**	**Standard deviation [m^3/s]**
Slippage	308.941	0.020
Overturning	365.646	0.045
Uplift	420.074	0.109

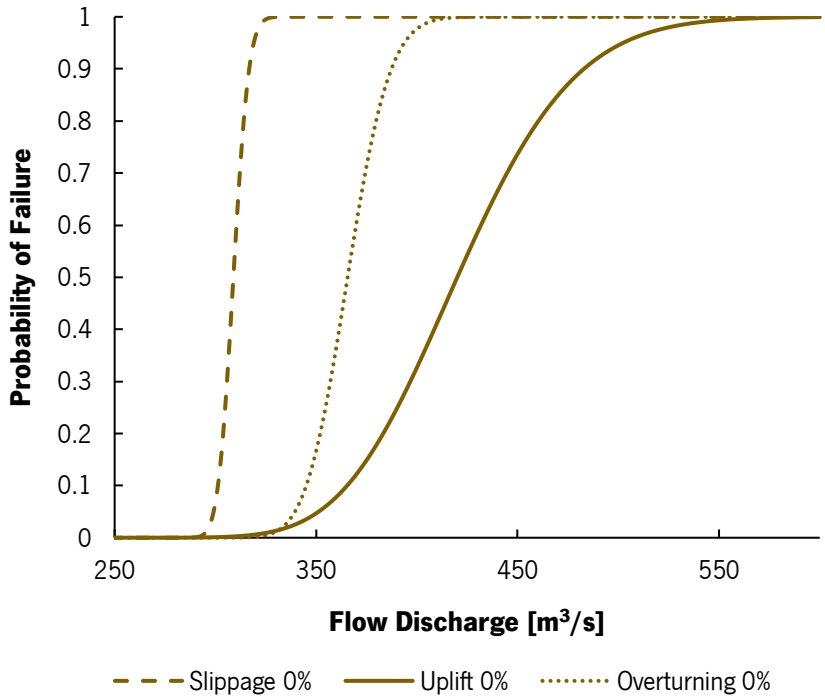


Figure 30. Slippage, Uplift and Overturning LS without driftwood clogging effect

The three failure mechanisms act concurrently under the influence of the same force, implying that once the first limit state is reached, structural failure occurs. In the specific case-study, slippage emerges as the most critical failure mode. Subsequently, the probability of driftwood blocking is calculated for each water surface elevation using Equation (23). The resulting fragility curve does not exhibit a normal distribution, as the probability of wood log entrapment follows a logit model.

To account for the most severe limit state, which is slippage, the 9 million runs are conducted for different blockage ratios. These ratios represent the proportion of the bridge clearance occupied by clogged driftwood, with values of 10%, 20%, 30%, and 40%.

When the blockage ratio is 0.20, it corresponds to the unclogged scenario, wherein only the deck's thickness hinders the river flow, calculated as 0.91 m / (3.6 m + 0.91 m) = 0.2. As per § 4.1.3, the initial driftwood accumulation is assumed to be 9.1 cm, corresponding to a deck's thickness increment (Δs) of 10%. Subsequent entrapped logs follow the same principle, leading to driftwood clogging thicknesses of 9.1 cm (Δs = 10%), 18.2 cm (Δs = 20%), 27.3 cm (Δs = 30%), and 36.4 cm (Δs = 40%) caused by a succession of log entrapments.

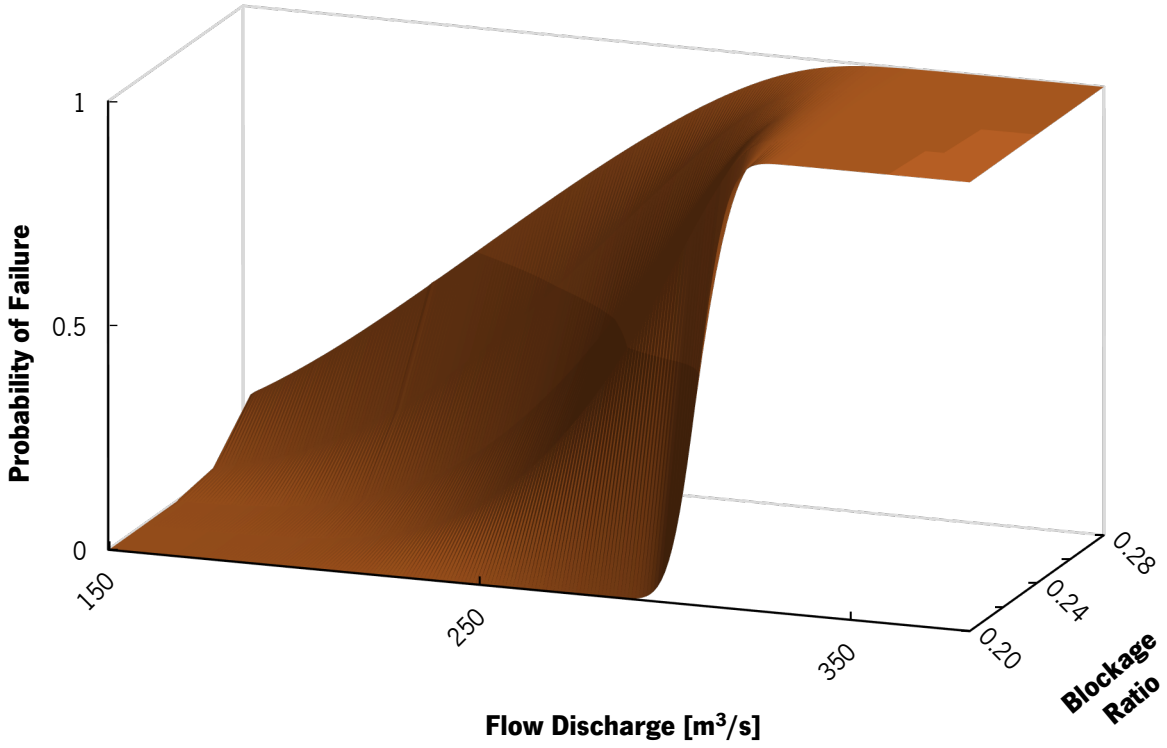


Figure 31. Interpolated Fragility Curves for Various Scenarios with Driftwood Blockage: the Influence of Increased driftwood clogging can be noticed in the "Blockage Ratio" axis, where the blockage ratio 0.20 corresponds to the case of absent clogged wood logs, while higher values characterise added driftwood

Bayesian probability is employed to analyse each scenario, initially assuming clogging as a certain event and subsequently considering its occurrence probability using Equation (11). The resulting fragility curve exhibits variation due to the log accumulation process, leading to higher probabilities of failures for a given discharge when driftwood clogging is present. Figure 31 and 32 demonstrate the significant impact of the blocking phenomenon on the failure probability of the bridge, with even a slight reduction in clearance leading to a noteworthy decrease in the structure's safety. Specifically, at a discharge of 298 m^3/s, the failure probability without driftwood clogging is 3.3%, whereas it rises dramatically to 76.8% when a 9.1 cm thick log jam occurs. This increase in failure probability is attributed to the amplified hydraulic forces experienced by the bridge deck, as the area normal to the flow expands; this value corresponds to 10 % of the deck's thickness (i.e., 91 cm x 0.1 = 9.1 cm).

The final aspect under consideration pertains to the impact of recalibrating the hydrologic model on the failure probability. Alterations in land use and the effects of climate change on precipitation patterns can result in the same discharge having different return periods. Consequently, a structure's safety levels throughout its lifespan will not only be influenced by factors such as structural aging and corrosion but also by changes in design loads. Figure 33 illustrates the application of this aspect to the case-study presented.

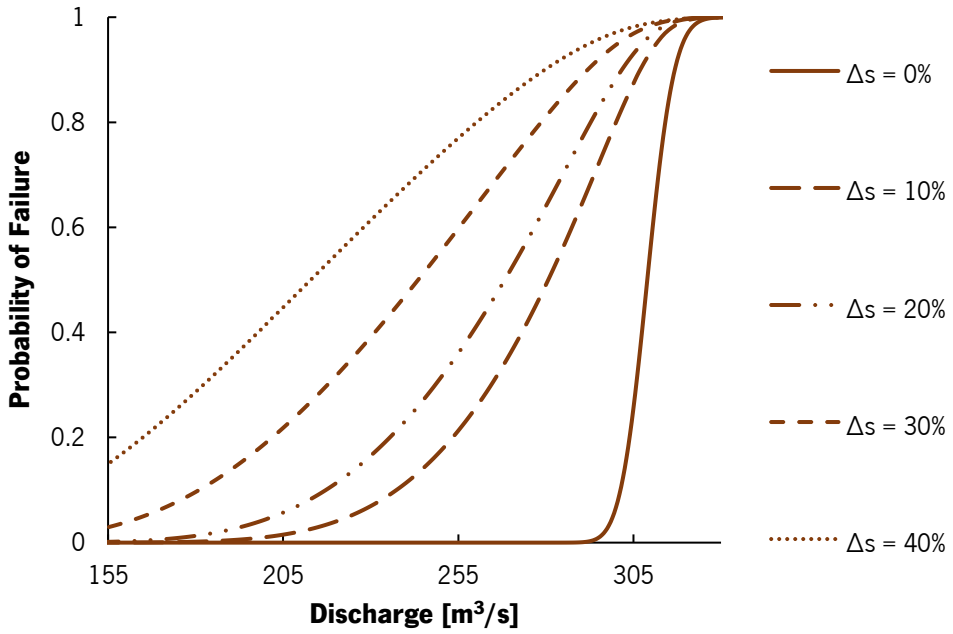


*Figure 32. Representation of FC at various clogging scenarios, indicated as a % of deck's thickness increment (Δs). The results are shown for slippage LS, where Δs = 0% corresponds to the Slippage curve of Figure 30. For each 10%, it results in Δs = 9.1cm increment of deck thickness; i.e., at Δs = 10%, the total deck thickness is: 0.91m + 0.1*0.91m = 1.00m*

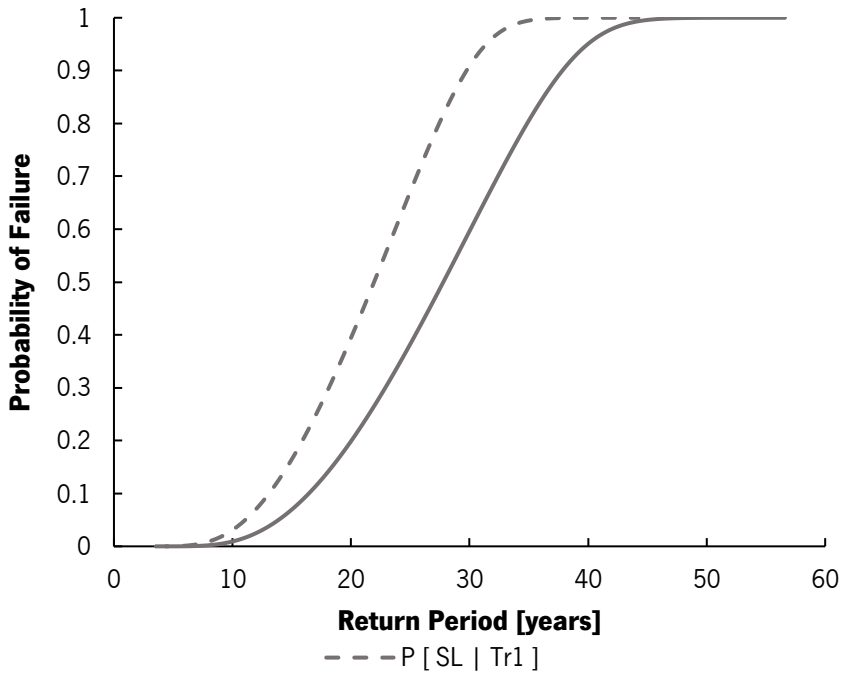


Figure 33. Effect of the recalibration of hydrologic model on the probability of failure, for slippage LS. The dashed line is employed for the first model (Tr1), while the continuous line displays the FC after the recalibration of the model (Tr2). As a result, P[SL | Tri] represents the conditional probability of failure for the slippage limit state (SL) given the original hydrologic model (Tr1) and the recalibrated hydrologic model (Tr2)

Based on Figure 33, it can be observed that a flood with a 30-year return period, before the model recalibration, would result in a failure probability of 0.9. However, after recalibration, the failure probability reduces to 0.6 for the same return period. The corresponding discharges for the 30-year return period are 306.1 m^3/s and 287.1 m^3/s, respectively. Therefore, the recalibration leads to a decrease in peak discharge of 6.2%, resulting in a significant 33.3% decrease in the failure probability.

This finding highlights that a relatively small decrease in peak discharge, as achieved through recalibration, can lead to a notable improvement in the structure's safety. The same principle applies when dealing with higher loads, wherein the hydrologic model recalibration proves to be crucial in ensuring structural safety.

The results highlight the relevance of assessing the hydraulic vulnerability of existing bridge stock on the structural safety point of view, which can be affected not only by factors such as aging, but also by changes in design loads due to land use and/or climate-related changes. In addition, the quantification of driftwood clogging mechanism is crucial for the definition of loads in new and existing structures.

Therefore, the proposed model provides valuable insights into the risks and vulnerabilities of bridge superstructures under different hydraulic conditions.

Overall, the study emphasizes the significance of considering multiple scenarios, probabilistic models, and recalibration techniques to comprehensively assess the safety of structures exposed to hydrological hazards. Such comprehensive evaluations can help engineers and decision-makers make informed choices during both the design and management of bridges.

6. Network Analysis

Alongside with an asset-level analysis, the network-level one helps to draw better conclusions on the relevance of specific assets on the overall system functionality. As stated in the previous Chapters, bridges have been identified as the most vulnerable component of the infrastructure system, particularly in the context of flood events (Giresini, Puppio and Sassu, 2016). Their collapse during floods can result in longer downtime compared to temporary flooded road links (Kalendher *et al.*, 2018). This vulnerability poses a significant challenge, especially in rural areas where the availability of traffic data is often inexistent. Consequently, bridge managers face the dual task of addressing local bridge issues and considering their impact on the entire network.

To address these challenges, the proposed framework aims to provide a versatile tool that can be applied in various contexts, as in rural areas. By developing a comprehensive methodology, this framework offers a systematic approach for bridge managers to assess and address the vulnerabilities of their bridge networks. The methodology's applicability is demonstrated through its implementation on the road network of Massa and Carrara in Tuscany, Italy.

The subsequent Paragraph presents an in-depth introduction to the framework, outlining its components and providing detailed explanations of the necessary code. This documentation enables users to replicate and adapt the framework for other locations, ensuring its widespread applicability and facilitating its implementation in different settings.

By offering a standardized and adaptable tool, the proposed framework equips bridge managers with the means to effectively evaluate the vulnerabilities of their bridge networks and devise appropriate mitigation strategies. The framework's versatility and replicability enable its implementation in diverse locations, promoting improved bridge network management and enhancing overall network resilience.

6.1. The Detour-Impact Index

The performance indicator proposed in this model is defined as the Detour-Impact Index (DII), which quantifies the effects of a disruption on the road network. The DII is calculated using Equation (26), where it is expressed as the ratio of the increased user costs following a disruption to the pre-event

conditions. This metric distinguishes itself from existing indicators by explicitly incorporating cost-specific functions rather than generalized ones.

The DII takes into account two crucial components: (i) the delay-cost function (DC) and (ii) the vehicle operating cost (VOC). These factors are influenced by various parameters, including (i) the average traffic speed, which is determined by the nonlinear volume-capacity relationship; (ii) the average daily traffic (ADT) along each road link; (iii) the driver's time cost function (DTC); and (iv) the traffic composition, specifically the percentage of trucks. Equations (28) and (29) provide detailed formulations for these components.

To further enhance understanding, Figure 34 provides a visual representation and explanation of the DII, illustrating how it captures the combined effects of the delay-cost function and the vehicle operating cost in assessing the impact of disruptions on the road network.

By utilizing the DII, the model enables a comprehensive evaluation of the consequences of disruptions, providing a more accurate and detailed assessment of the road network's performance. The DII's incorporation of cost-specific functions and consideration of various factors related to traffic speed, volume, driver's time cost, and traffic composition contribute to a more nuanced understanding of the impacts and costs associated with disruptions in the network.

$$DII_i = \frac{\Delta H_i}{NH_j} \tag{26}$$

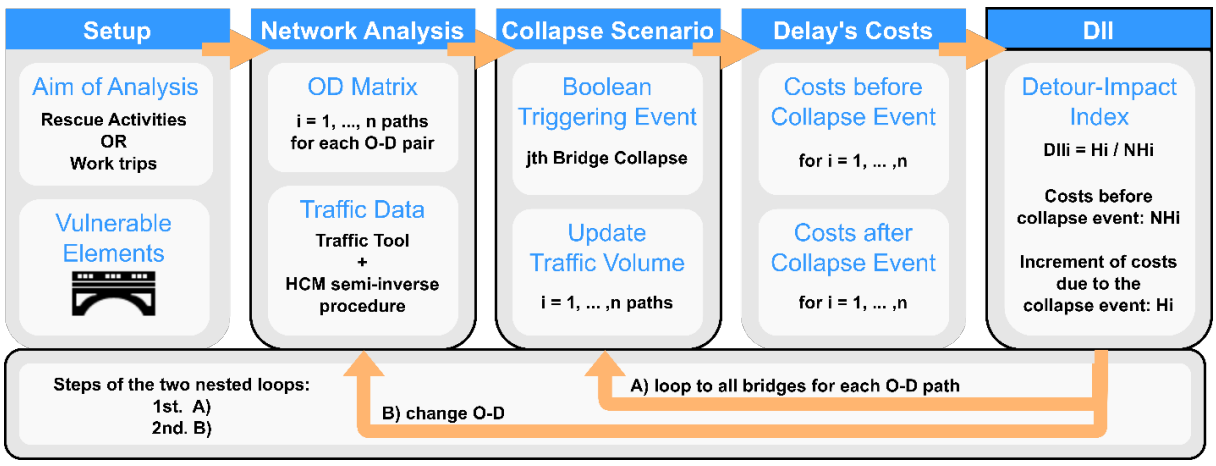


Figure 34. The DII (Detour–Impact Index) Method Flowchart

Let $i = 1, \ldots, n$ represent the alternative paths, and j denote the path that is closed due to the failure of a network component. The increment of costs ΔH in EUR associated with the post-hazard

scenario is compared to the costs (NH) assessed in the absence of hazards. The DII measures the impact of traffic-related costs, with higher values indicating a greater impact.

It is important to note that in Equation (26), the increased costs on alternative paths are normalized to those of the closed route during normal operations. This normalization allows for the estimation of the detour's impact, which is particularly useful for regular users when a path is closed. For each i-th alternative, three types of expenditures need to be considered: (i) the normal-operational costs in the j-th path, (ii) the normal-operational costs in the i–th path, and (iii) the post-hazard costs in the i–th path.

To evaluate the parameter ΔH for each link, the costs obtained in the post-hazard scenario $(DC_k + VOC_k)$ on the i-th path are subtracted from the costs in the normal condition $(NC_k + NVOC_k)$ as shown in Equation (27). Here, $k = 1, \ldots, m$ represents the links of the selected i–th path that connect the Origin-Destination O-D points as illustrated in Figure 35.

By considering these calculations and utilizing the framework, it becomes possible to quantify the impact of disruptions and evaluate the associated costs on different alternative paths. This analysis aids in understanding the detour effects and assists regular users in making informed decisions when faced with a closed path.

$$\Delta H_i = \sum_{k=1}^{m} (DC_{ik} + VOC_{ik}) - (NC_{ik} + NVOC_{ik}) \qquad (27)$$

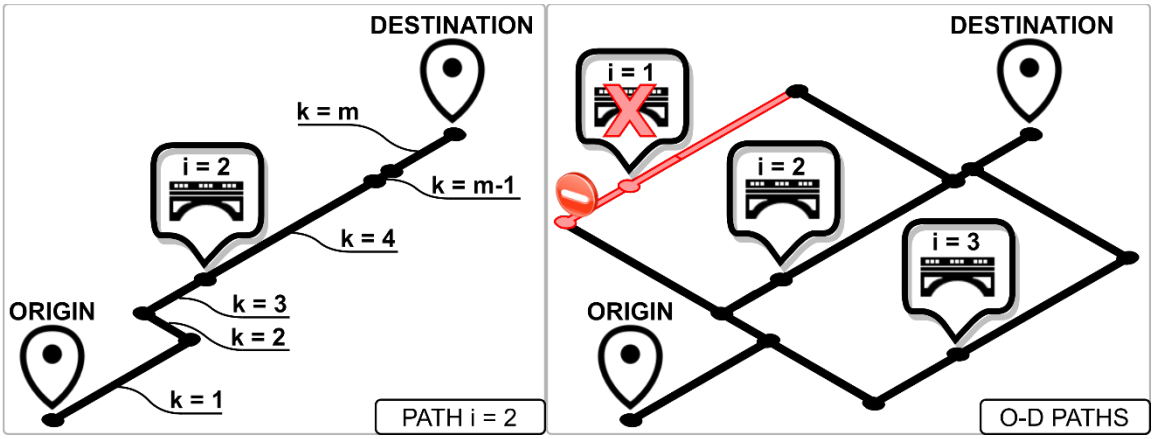


Figure 35. Failure scenario and example of alternative path. The network on the right side shows i=1 as the j-th path. The path considered as alternative is displayed on the left. In the specific case, i = 2

To calculate ΔH, it is insufficient to solely consider the post-hazard scenario. If the term $(NC_k + NVOC_k)$ it is excluded from Equation (27), ΔH would encompass the total expenditures, including the traffic component during normal-operational conditions. To better understand this concept, the daily delay costs, denoted as $\mathrm{DC_k}$ in Equation (28) can be examined.

In other words, by including the term $(NC_k + NVOC_k)$ in Equation (27), it is distinguished the additional costs incurred specifically as a result of the hazard event. This approach allows to isolate and evaluate the incremental impact of the hazard-related disruptions on the network. By focusing on the daily delay costs represented by DC_k in Equation (28), a clearer perspective on the financial implications of delays caused by the disruptions is gained.

By considering both the post-hazard scenario and the corresponding normal-operational conditions, it can effectively be quantified the specific impact of the hazard event on the network, accounting for the additional costs associated with delays. This approach ensures a comprehensive assessment of the detour-related expenditures and provides a more accurate understanding of the economic consequences of the disruptions.

$$DC_{ik} = T_{aik} \cdot 1day \cdot ADT_{ik} \cdot \sum_{r=1}^{4} (DTC_{ir} \cdot p_{ir}) \quad (28)$$

The traversal time of the k-th link, denoted as $\mathrm{T_{aik}}$ is computed as the ratio of the k-th link length $\mathrm{L_{ik}}$ to the reduced speed $\mathrm{S_{aik}}$ obtained through the updated volume-capacity ratio of the street. The average daily traffic on the k-th link of the i-th alternative path is represented by $\mathrm{ADT_{ik}}$.

In the traffic assignment problem, a system-optimal management approach is adopted, although alternative assignments can be explored, as detailed in the § 2.3. The cost per unit of time (hours) associated with the user's trip purpose is captured by $\mathrm{DTC_{ir}}$, which corresponds to the cost for individuals undertaking work or non-work trips while driving a vehicle of class "r," as described by Gervásio and da Silva (2013). In rural areas, commuter journeys, specifically work trips, are typically the most common scenario. For more detailed analyses, the $\mathrm{ADT_{ik}}$ can be disaggregated into work and non-work trips using census data and local surveys. In such refined setups, the computation of indirect costs should be performed separately and added before calculating the DII.

The percentage of each vehicle type in the traffic composition is denoted by p_{ir}. Similarly, the parameter $\mathrm{NC_{jk}}$ is evaluated accordingly, incorporating the $\mathrm{ADT_j}$ term and the normal operation speed $\mathrm{S_{nk}}$. The vehicle operating cost (VOC) is computed based on the methodology outlined by Gervásio and da Silva, (2013), with modifications to suit the proposed framework. Thus, the $\mathrm{VOC_{ik}}$ is calculated according to Equation (29). Considering these parameters and equations, the framework enables the evaluation of traversal times, traffic composition, and associated costs, contributing to a comprehensive analysis of the DII.

$$VOC_{ik} = -\frac{S_{pik}}{S_{nik}} \cdot L_{ik} \cdot 1day \cdot ADT_{ik} \cdot \sum_{r=1}^{4} (DTC_{ir} \cdot p_{ir}) \quad (29)$$

Both the parameters VOC_{ik} and $NVOC_{ik}$ incorporate the present speed S_{pik}. In VOC_{ik} the value of S_{pik} is equal to S_{aik} during the post-hazard conditions, while it is equal to S_{nik} during normal conditions. This differentiation is accompanied by a negative-value VOC term. This choice is made because the vehicle's operative cost is highest when the expression L_{ik}-S_{pik}/S_{nik}·L_{ik} reaches its maximum value, which occurs when S_{pik} equals S_{aik}. Consequently, in Equation (27), VOC_{ik}-$NVOC_{ik}$ corresponds to L_{ik}-S_{aik}/S_{nik}·L_{ik}, representing the difference in operative expenditures between vehicles traveling at normal speed S_{nik} and reduced speed S_{aik}.

Similarly, the parameter $NVOC_j$ is evaluated accordingly, with the same consideration regarding the ADT_j term and without the minus sign. In this case, no difference is assessed, but rather only the operative costs associated with the traffic volume ADT_{jk}. The DII serves as the ultimate output of the framework. The methodology involves five distinct steps: (i) delimitation of the study area; (ii) acquisition of road network and bridge maps; (iii) identification of settlements and construction of an O-D matrix to generate the paths; (iv) utilization of the developed Traffic Script algorithm to analyse congestion scenarios; and (v) consideration of collapse scenarios for each infrastructure and assessment of the DII.

The flowchart depicting the methodology is presented in in Figure 34, accompanied by a detailed theoretical discussion within this Paragraph. The application of the methodology is exemplified through a case study in Chapter 7, demonstrating its practical implementation and effectiveness.

6.2. Analysis of the Study Area

The selection of the study area is accomplished using a Geographic Information System (GIS) tool, whereby administrative boundaries are utilized to delineate the specific portion of territory. It is important to note that the framework presented in this study is specifically tailored for rural areas, and as such, other contexts are not investigated in detail. However, it is worth mentioning that the theoretical model of the framework remains applicable in urban areas as well, albeit requiring a higher computational effort due to the increased density of bridges, roads, and alternative paths commonly found in cities. Nonetheless, the availability of more data in urban areas justifies the adoption of existing methods, whereas the proposed framework demonstrates its practical usefulness in rural contexts.

The second step in implementing the framework involves gathering the road network map and the vector containing the locations of bridges within the study area. This task can be accomplished by utilizing GIS maps, although it is important to acknowledge the issue of data availability, specifically with regards to the accurate dataset of bridge locations. To overcome this challenge, two procedures are proposed. In Procedure 1, the road network map is considered as a graph G(S, N), comprising links (S) and nodes (N), with nS denoting the number of links and nN denoting the number of nodes. By assigning an elevation attribute to each link Zi = {−1, 0, 1}, as proposed in Jedlička *et al.*, (2016), bridges can be identified using the expression: $B=Z_0 \cap Z_1$, where $Z_0 \subseteq S$ and $Z_1 \subseteq S$. In Procedure 2, bridges can be identified by utilizing a river network map W consisting of nW segments, employing the expression $B=(W \cap Z_0) \cup (W \cap Z_1)$, where Z_0 and Z_1 represent elevation attributes.

Furthermore, the study requires information regarding the locations of strategic buildings, which can be obtained from Emergency Limit Condition (CLE) maps (Dolce, Bramerini and Castenetto, 2016). It is important to acknowledge that the number of bridges, strategic structures, and infrastructure links considered in the analysis may be reduced depending on whether a hazard simulation scenario is conducted in parallel. Additionally, settlements are identified and connected to the Civil Protection headquarters through the use of a destination vector D, where D is a subset of N. This ensures that the arrival point is integrated into the graph G, enabling the utilization of routing algorithms such as Dijkstra (Schneck and Nökel, 2020).

The subsequent step involves the design of the O-D matrix. Each small town is linked to the Civil Protection headquarters, resulting in multiple destinations for each origin. Each O-D pair P consists of nP paths, and routing algorithms, such as those described by Pella and Ose (2018), can be employed to generate each path p ∈ RnP. Each path is comprised of a set of links k = 1...m (Figure 35), with each link characterized by a traffic volume v_k. While theoretically one can assume knowledge of the volume of vehicles, in practical applications, data availability on rural roads poses a significant challenge. To address this, an innovative web-based method has been developed to gather traffic data, which will be further explained in the subsequent Paragraph.

6.3. Analysis of Traffic Data

The novel methodology initiates by utilizing web-based traffic layers, such as those available in Google Maps. While these layers provide qualitative information, they can serve as an immediate, simple,

and effective means to collect data on traffic conditions when traditional on-site traffic counters are unavailable. It is important to note that the proposed method is not intended to replace the more reliable traditional in-situ counting techniques; rather, it aims to provide an initial estimation of traffic volume and quality.

The fundamental concept underpinning the proposed procedure revolves around populating each v_k vector with quantitative information derived through a two-step process: (i) the utilization of the Traffic Script to gather qualitative data, and (ii) the application of an algorithm to convert the qualitative traffic information into vehicle volumes. This approach allows for the transformation of subjective traffic observations into objective and quantitative measures. By leveraging web-based traffic layers, users can obtain a general sense of traffic conditions in the absence of dedicated traffic counters, providing valuable insights for further analysis and decision-making.

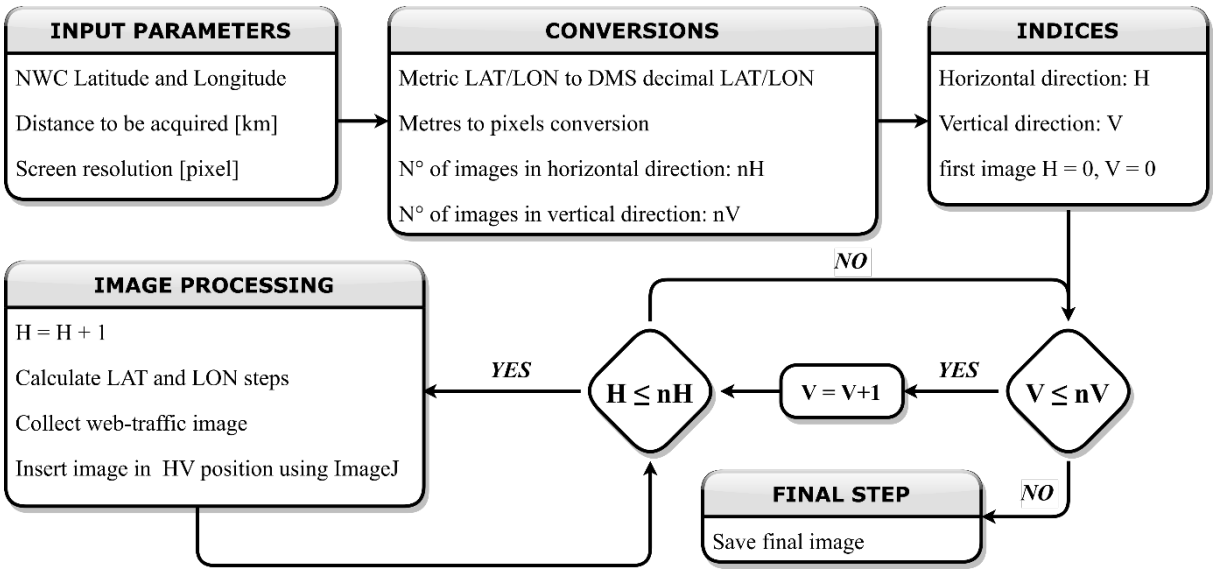


Figure 36. The flowchart of the Traffic Script, described in detail in § 6.4

6.4. Obtaining the Traffic through the Traffic Script

To collect the qualitative data from web-based traffic layers, a custom script called Traffic Script is developed by the author. The script is implemented using ImageJ software (WS, 2009). The algorithm's flowchart is illustrated in Figure 36, and the code can be found in § 6.5.

The Traffic Script captures individual web images, such as those from Google Maps, at different latitude and longitude coordinates, and then merges them into a single, larger image. This merging

process follows a matrixial order, utilizing nested loops for latitude and longitude calculations. Figure 37 provides a practical example of this assembly process.

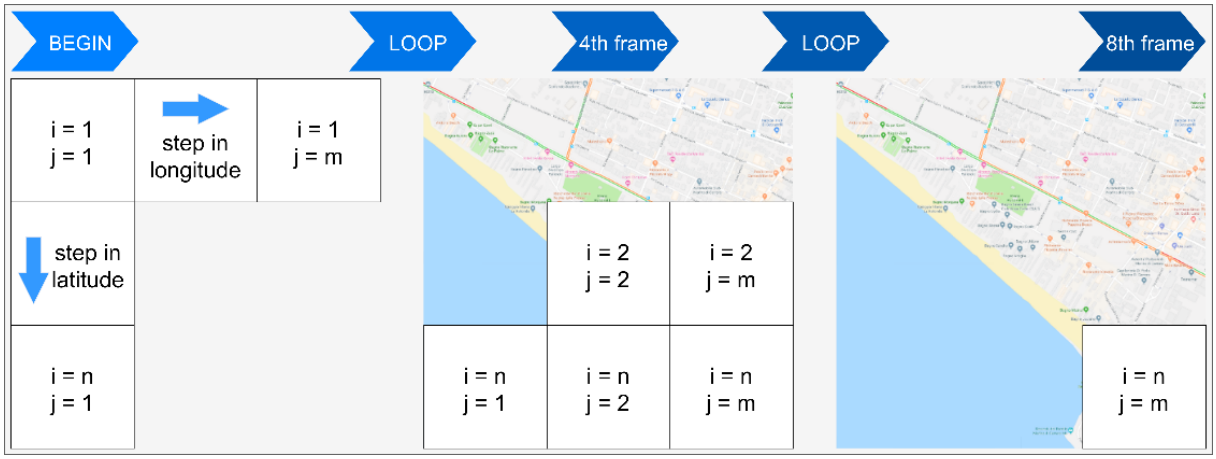


Figure 37. The process of image assembling. In the specific case, images are retrieved from Google Maps©

Subsequently, a raster is generated for each web-based traffic colour using another ImageJ script, which is provided together with the Traffic Script. Each raster image is then overlaid with the road network shapefile using GIS software. This is achieved by importing the raster file along with its companion tfw file, which is also created by the Traffic Script. By utilizing GIS plugins, the properties of each raster can be incorporated into the shapefile. Additionally, a new column is created in the attribute table for each path p ∈ RnP. It is important to note that user supervision is necessary during these automated steps, as occasional manual adjustments may be required.

The web-based traffic colours, as observed in maps such as Google Maps, are categorized as follows: green corresponds to AB, orange to CD, red to E, and dark red to F. These labels are used to populate the newly created column in each p vector file, resulting in a road network shapefile with qualitative traffic information. As the simulations rely on web-based traffic data, multiple simulations can be conducted during local peak hours or at specific times, depending on the objectives of the analysis.

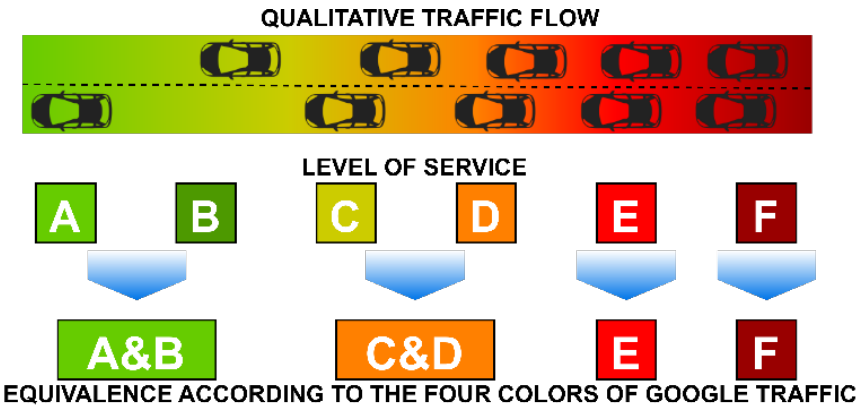


Figure 38. The Level Of Service (LOS) comparison with the qualitative classification of Google Traffic

6.5. More Insights into the Traffic Script

This Paragraph illustrates the rationale behind the Traffic Script, by examining its code. The language used is “IJ1”, a C variant. The IJ1 is implemented in the ImageJ software; as such, the compilation is made within ImageJ. The user is prompted to introduce several calibration parameters, which are spread throughout the code. Therefore, it is deemed necessary to explain each block of the code for a better reproducibility. The program comes with a GUI to facilitate its usage.

The first chunk of code is reported below:

```
//EPSG_25832 (ETRS89 UTM32N) but it works also on other UTM zones based on ETRS89 (change variables "utmz" and "north" embedded in this code.
lat_START=4937506.816283; //***insert latitude in km***
lon_START=525114.659777; //***insert longitude in km***
Hokm=1.5; /*horizontal extension in km*/
Vekm=1.5; /*vertical extension in km*/
titolo = "Results"; /* destination’s folder name*/
aspetto = "C:\\User path ...\ TrafficScript\\";
Dialog.create("Traffic Script");
Dialog.addMessage("Check brower compatibility and adjust the code accordingly");
Dialog.addMessage("Disclaimer: This example code redirects the user to Google Maps.");
Dialog.addMessage("The user should respect Google Maps Terms of Service");
Dialog.addMessage("and the Authors are not responsible for any violation of the fair use of Google Maps Terms of Service.");
Dialog.addMessage("If the user wish to use another web-based service, she/he should modify the code in the URL section");
Dialog.addMessage("More info at https://www.google.com/intl/en_en/help/terms_maps.html" );
//set P1 and P2 to correctly crop the images according to the user’ screen dimensions
Dialog.addString("Destination folder's path:", aspetto,30);
Dialog.addString("Destination folder's name:", titolo,30);
Dialog.addNumber("Starting Latitude:", lat_START,10,30,"check if the coordinate is in the right UTM zone");
Dialog.addNumber("Starting Longitude:", lon_START,10,30,"check if the coordinate is in the right UTM zone");
```

```
Dialog.addNumber("Horizontal distance (H) in km of the area to be analysed:", Hokm,2,5,"km");
Dialog.addNumber("Vertical distance (v) in km of the area to be analysed:", Vekm,2,5,"km");
Dialog.addNumber("Width in pixel of the screen:", 1440);
//EDITABLE FOR OTHERS SCREEN RESOLUTION
Dialog.addNumber("Height in pixel of the screen:", 900);
//EDITABLE FOR OTHERS SCREEN RESOLUTION
Dialog.show();
```

The above code produces the following graphical result:

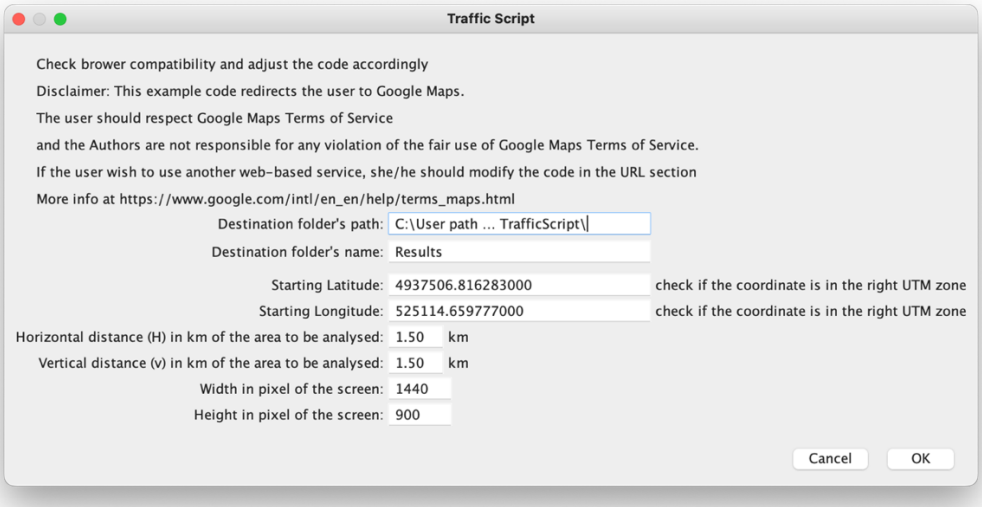


Figure 39. Traffic Script GUI: input variables

Then, the program reads the user's inputs and starts to calculate the final LAT, LON tuple based on the desired area to analyse. In this case, 1.5 km is selected for both coordinates. Then, the function "cells_numb()" computes how many images are required at a certain resolution and scale. Both parameters have been calibrated using ImageJ pixel ruler in combination with the corresponding metric distances reported inspecting the web-based maps.

The following Traffic Script Code reads the user's inputs and establishes the number of frames to be produced, based on pixel-based calibration of web-based images.

```
aspetto = Dialog.getString();
titolo = Dialog.getString();
latitudine_iniziale = Dialog.getNumber();
longitudine_iniziale = Dialog.getNumber();
L_area_selezionata_km = Dialog.getNumber();
```

```
H_area_selezionata_km = Dialog.getNumber();
L_schermo_px = Dialog.getNumber();
H_schermo_px = Dialog.getNumber();
scelta = Dialog.getChoice();
latin=latitudine_iniziale;
longin=longitudine_iniziale;
deltalong=L_area_selezionata_km;
deltalat=H_area_selezionata_km;
Lpx=L_schermo_px;
Hpx=H_schermo_px;
filenome=titolo;
latfin=latin+deltalat*1000; //FINAL LATITUDE OF IMAGE
longfin=longin+deltalong*1000; //FINAL LONGITUDE OF IMAGE
print(latfin);
print(longfin);
//P1 & P2 are the crop parameters.
P1=(Lpx/2)-210; //NWC x value
P2=(Hpx/2)-352; //NWC y value
t=1200; //time parameter
lunghezza_cella=707; //horizontal length of image
altezza_cella=707; //vertical length of image
A00=cells_numb(); //call to the function
//The function cells_numb compute how many images are required at a certain resolution and scale;
function cells_numb() {
metriapx=0.86577; //to be calibrated if the images overlap. This parameter is set for Google's z
parameter equal to: z=17
Ltot_img_in_px=deltalong*1000/metriapx;
frameorizz=floor(Ltot_img_in_px/lunghezza_cella);
Htot_img_in_px=deltalat*1000/metriapx;
framevert=floor(Htot_img_in_px/altezza_cella);
FO=frameorizz;
Nimg_Vert=FO;
```

```
FV=framevert;
Nimg_Oriz=FV;
print("horizontal frames");
print(FO);
print("vertical frames");
print(FV);
print("the total number of images will be: ", FO*FV);
A00=" "+(FO*FV);
return A00;}
```

Then, the program generates directories to store partial results and generates other related variables. It is at this stage that the user can change the UTM zone, including the hemisphere in which the area is taken, as follows:

```
// Main Directory
Main = aspetto+titolo+File.separator;
File.makeDirectory(Main);
//String Concatenate + calculus function call.
Path1 =Main+File.separator;
File.makeDirectory(Path1);
//CHANGE FROM HERE for other web-based maps
a="https://www.google.com/maps/@";
calculus();
function calculus() {
Path =Path1+File.separator;
File.makeDirectory(Path);
madi=0.86577*707; //calibration parameter
x1=latin;
y1=longin;
frameorizz=floor((deltalong*1000)/madi);
framevert=floor((deltalat*1000)/madi);
FO=lunghezza_cella*frameorizz;
FV=altezza_cella*framevert;
frametotali=frameorizz*framevert;
```

```
dimensione=(madi*framevert)/1000;
print(dimensione);
longinAUX=longin-madi*0.5;
latinAUX=latin+madi*0.5;
print(longinAUX);
print(latinAUX);
sl='','';
resto="17z/data=!5m1!1e1";
subcalculus();}
function subcalculus() {
x=lon_START;
y=lat_START;
//— CHANGE HERE FOR OTHER UTM ZONES —//
utmz=32;
north=true;
```

Then, the UTM coordinates entered in the first page of GUI are converted in decimal degrees. This because it is easier for the user to indicate the areal dimension in km to be analysed rather than inserting the final coordinates in decimal degrees. Hence, the Map Projection's Working Manual from USGS is used to transform UTM kilometric coordinates in WGS84 ones (Alsobky and Mousa, 2020). The given input coordinates are also subjected to a preliminary validation, to understand whether errors from the user lead to coordinates outside the permissible ranges, given that each UTM zone has boundaries. The Traffic Script Code to change kilometric into decimal degrees coordinates is presented below:

```
// Symbols as used in USGS PP 1395: Map Projections - A Working Manual
a_param=6378137.0; //equatorial radius (in meters)
f_factor=1/298.2572236; //polar flattering
degTOrad=PI/180; //degrees to radians
//constants
k0=0.9996;
//scale on central meridian
b_const=a_param*(1-f_factor);
//polar axis
```

```
e_const=sqrt(1-(b_const/a_param)*(b_const/a_param));
//eccentricity
e0=e_const/sqrt(1-e_const*e_const);
//called e' in reference
esq=(1-(b_const/a_param)*(b_const/a_param)); //e^2 for use in expansions
e0sq=(1-e_const*e_const);
//e0^2
//First some validation:
if (x < 160000 || x > 840000) {
print("Outside permissible range of easting values.");
return;}
if (y < 0){
print("Negative values are not allowed for northing.");
return;}
if (y > 10000000) {
print("Northing may not exceed 10,000,000.");
return;}
//actual calculation
zcm=3+6*(utmz-1)-180; //central meridian of zone
e1=(1-sqrt(1-e_const*e_const))/(1+sqrt(1-e_const*e_const));
//called e1 in usgs pp1395
M0=0; //in case of origin other than zero lat (not needed for standard UTM)
//M is the arc length along standard meridian
if (north) {
M = M0 + y/k0;}
else { // southern hemisphere
M = M0 + (y-10000000) / k;}
mu=M/(a_param*(1-esq*(1/4+esq*(3/64+5*esq/256))));
phi1=mu+e1*(3/2-27*e1*e1/32)*sin(2*mu)+e1*e1*(21/16-55*e1*e1/32)*sin(4*mu); //footprint
latitude
C1=e0sq*pow(cos(phi1),2);
T1=pow(tan(phi1),2);
```

```
N1=a_param/sqrt(1-pow(e_const*sin(phi1),2));
R1=N1*(1-e_const*e_const)/(1-pow(e_const*sin(phi1),2));
D=(x-500000)/(N1*k0);
//phi=phi1-(N1*tan(phi1)/R1)*(((D*D)*(1/2-D*D*(5+3*T1+10*C1-4*C1*C1-
9*e0sq)/24))+(pow(D,6)*(61+90*T1+298*C1+45*T1*T1-252*e0sq-3*C1*C1)/720));
phi = (D*D)*(1/2-D*D*(5+3*T1+10*C1-4*C1*C1-9*e0sq)/24);
phi = phi+pow(D,6)*(61+90*T1+298*C1+45*T1*T1-252*e0sq-3*C1*C1)/720;
phi = phi1-(N1*tan(phi1)/R1)*phi;
```

Then, the output latitude and longitude in WGS84 Map Projection are computed. The area of interest, previously indicated as 1.5 km x 1.5 km, translates into a number of image frames in horizontal (longitude) and vertical (latitude) directions. These intermediate outputs are displayed in the following GUI:

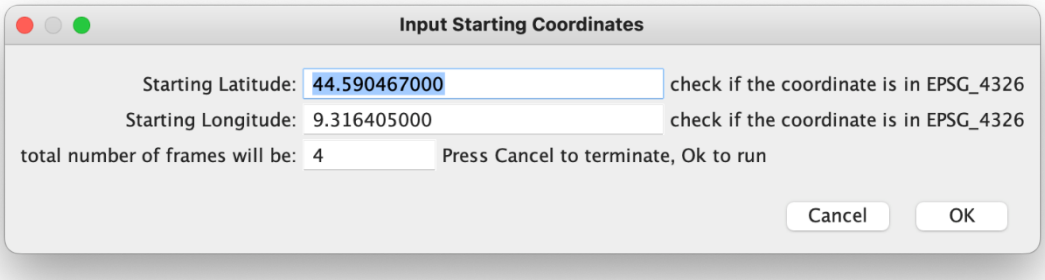


Figure 40. Traffic Script GUI: output intermediate variables

The code to generate the GUI of Figure 40 is displayed as follow:

```
//output Latitude
outLatitude=floor(1000000*phi/degTOrad)/1000000;
outLatitude=d2s(outLatitude, 10);
lng=D*(1+D*D*((-1-2*T1-C1)/6+D*D*(5-2*C1+28*T1-3*C1*C1+8*e0sq+24*T1*T1)/120))/cos(phi1);
lngd=zcm+lng/degTOrad;
//output Longitude
outLongitude=floor(1000000*lngd)/1000000;
outLongitude=d2s(outLongitude, 10);
Dialog.create("Input Starting Coordinates");
Dialog.addNumber("Starting Latitude:", outLatitude,10,30,"check if the coordinate is in EPSG_4326");
```

```
Dialog.addNumber("Starting Longitude:", outLongitude,10,30,"check if the coordinate is in EPSG_4326");
Dialog.addNumber("total number of frames will be:", A00,0,10,"Press Cancel to terminate, Ok to run");
Dialog.show();
```

If Run button in Figure 40 is clicked, the program generates the final image dimension. Two additional calibration parameters are introduced to fine-tuning the assembly process described in Figure 37. The code is displayed below:

```
outLat = Dialog.getNumber();
outLon = Dialog.getNumber();
print(outLat);
print(outLon);
//finecalcolo
filenome=titolo+"X"+x1+"X"+y1;
newImage(filenome, "RGB
White", FO, FV,1); //this generates the final image
setLocation(0,0);
sel1=getImageID();
Latadimm=0.005455;  //image shift adjust on rows. Calibrate for each user (if needed)
Longadimm=0.007584; //image shift adjust on columns. Calibrate for each user (if needed)
```

The final image processing consists of two nested for cycles, one for the Longitude (horizontal step) and one for the Latitude (vertical step). The ftp parameter defines the concatenation of strings to select the URL of web-based images. Waiting intervals are included as a buffer to account for WLAN or WiFi speed and CPUs load. To this end, a user has to adjust the parameter if a slower/faster machine or network are employed. The final image assembly process is executed within ImageJ and saved as a .tif file. The “CleanAll” function ensures that all the open windows are closed properly and ensures no background activity.

```
for(n_incremento_V=0;n_incremento_V<framevert;n_incremento_V++) {
steplat=outLat-(n_incremento_V*Latadimm);
steplat=d2s(steplat, 10);
for(n_incremento_H=0;n_incremento_H<frameorizz;n_incremento_H++) {
steplong=outLon+(n_incremento_H*Longadimm);
steplong=d2s(steplong, 10);
```

```
ftp=a+steplat+sl+steplong+sl+resto;
run("URL...", "url="+ftp);
wait(5*t);
run("Capture Screen ");
wait(300);
makeRectangle(P1, P2, lunghezza_cella,
altezza_cella);
run("Crop");
setLocation(100,0);
sel2=getImageID();
selectImage(sel2);
run("Select All");
run("Copy");
wait(300);
selectImage(sel1);
wait(600);
makeRectangle(n_incremento_H*lunghezza_cella, n_incremento_V*altezza_cella, lunghezza_cella,
altezza_cella); //make an empty rectangle in ImageJ, to store the mosaic of images as final one
run("Paste");
selectImage(sel2); //image selection within ImageJ
close();}}
selectImage(sel1); //image selection within ImageJ
saveAs("Tiff",Path+filenome+".tif"); //save image on the selected path
close();}
function CleanAll() { //start of the CleanAll fuction, to free up temporary memory and prepare other runs
if (isOpen("Results")) {
wait(50);selectWindow("Results"); run("Close" );} //waiting time needed, depending on hardware
while (nImages()>0) {
wait(50);
selectImage(nImages());
run("Close");}}
// end of CleanAll function
```

6.6. Traffic Data Transformation: Qualitative to Quantitative

The qualitative information obtained from the Traffic Script is transformed into quantitative data using a novel algorithm that incorporates equations from the Highway Capacity Manual (HCM) (Transportation Research Board, 2010). The process is outlined in Figure 41. The qualitative traffic obtained from the Traffic Script is compared with the level of service (LOS) defined by the HCM, with the criterion established according to Figure 38. The rationale behind this choice is rooted in the definitions of each qualitative metric. For instance, Google has stated that the traffic colours represent different levels of congestion-induced delay (Google LLC, 2020), while the LOS is a measure of traffic performance.

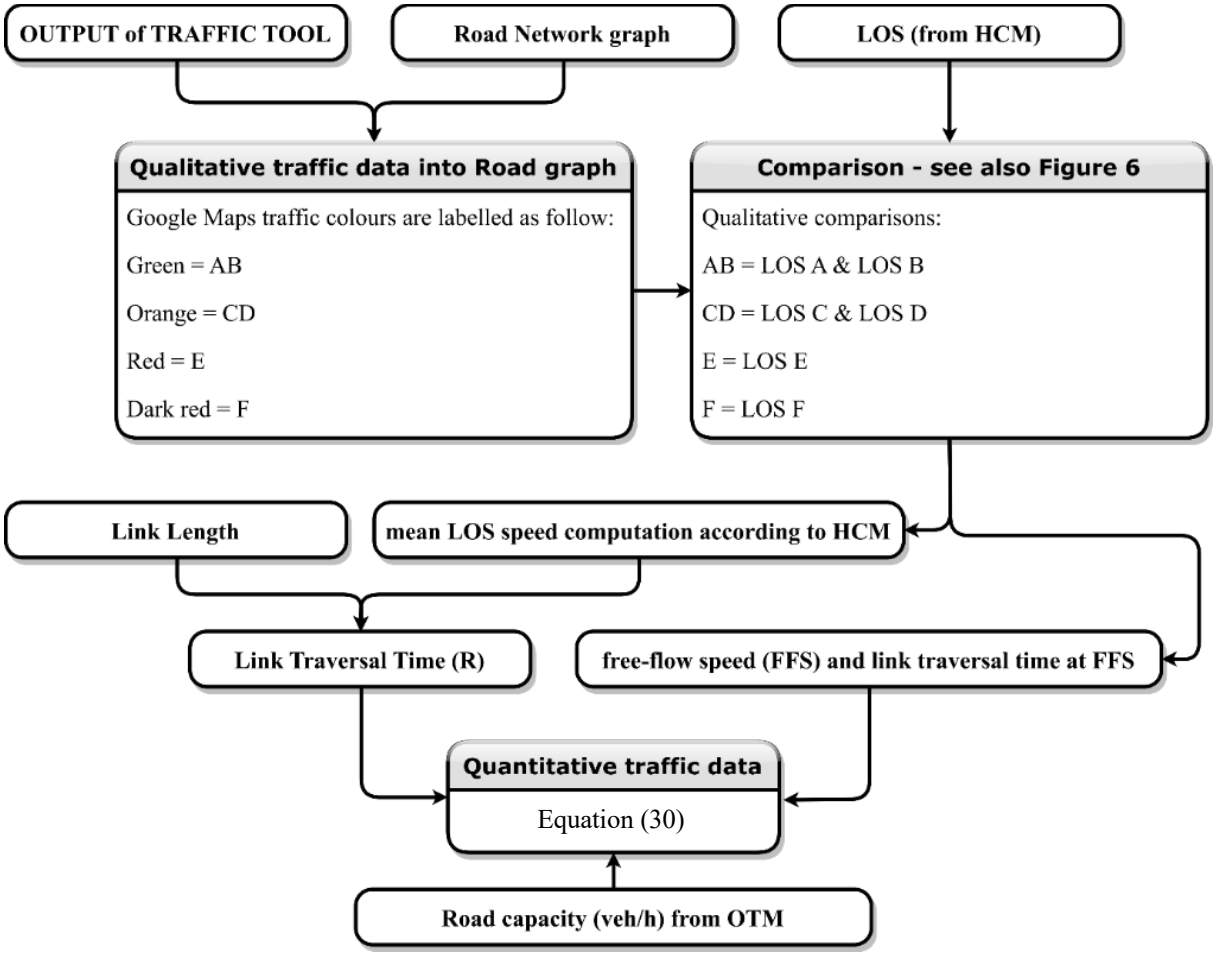


Figure 41. The flowchart for quantitative traffic assessment

The qualitative relationship between these two indices can be based on the expected level of delay. Since Google Traffic has four levels and the LOS has six, a clustering of the HCM index is proposed. An additional innovation lies in the use of the LOS as an input, although it is traditionally considered an output. A reverse-phased method is adopted, allowing for the computation of quantitative traffic volumes. Each LOS is associated with a range of traffic speeds, and the mean value of each speed range, denoted

as S_{LOS}, is assumed. The link traversal time, denoted as R_t, can then be calculated using the simple relation $R_t = L/S_{LOS}$, where L represents the link length. Similarly, the link traversal time at free-flow speed, denoted as R_0, can be evaluated using the HCM. Consequently, the quantitative traffic volume, which is based on the LOS of road links, can be determined using Equation (30).

To derive the volume of vehicles, the acquired images are processed using the script provided in § 6.5. This script is also integrated into a GIS environment following the procedures described in the previous subparagraph.

$$v = \left\{ \frac{T \cdot (R_t - R_0) + 2(R_t - R_0)^2}{2JL^2 + T(R_t - R_0)} \right\} \cdot c \tag{30}$$

In Equation (30), J represents a calibration parameter with specified values in the HCM, while c denotes the capacity of the street in vehicles per hour, which is obtained from open transport maps (OTMs) (Jedlička *et al.*, 2016). T refers to the reference period, typically set as 1 hour. It should be noted that the aforementioned equation does not account for delays caused by signalized intersections. While this can be a concern in urban areas with numerous traffic lights, it is generally not applicable to rural areas. The traffic volume derived from Equation (30) is directly associated with the Average Daily Traffic (ADT) term in Equation (28) and (29), and consequently, it is directly linked to the DII. To obtain the ADT, the volume in vehicles per hour needs to be divided by the hourly volume factor, which is typically assumed to be 0.10. The computation of traffic volume sets the foundation for the subsequent step, which introduces the collapse scenarios.

6.7. Bridge Collapse Scenario

All the data that has been collected and processed thus far is utilized to simulate the repercussions of a road failure. The first step involves converting the road network into a routable graph. In this process, nodes are generated at each intersection based on the map's topology, and directional properties are incorporated into the network, with edges serving as connectors between nodes. Subsequently, all the paths between an origin and destination (O-D) pair are generated using a routing plugin. Existing algorithms with a GIS interface can be utilized for this purpose (Gusev, 2015). This aspect is particularly significant when considering alternative paths. Each route contains information regarding

traffic volumes, which have been calculated using Equation (30). For each O-D path, Equation (31), adapted from the HCM, is employed to evaluate the traversal time R_c, expressed in hours, during the collapse scenario.

$$R_c = R_0 + 0.25\left[\frac{v_{upd}}{c} - 1 + \sqrt{\left(\frac{v_{upd}}{c} - 1\right)^2 + \frac{16J \cdot v_{upd}}{c} \cdot L^2}\right] \qquad (31)$$

The detoured traffic from the collapsed link is represented by the volume-capacity ratio v_{upd}/c, as illustrated below. The total travel time for a given O-D path is determined by summing all the computed R_c values for each link of length L. To simulate the failure scenario, all the paths for each O-D pair are taken into consideration. The computation of the DII is demonstrated according to the framework depicted in Figure 42, where the positions of bridges are determined by the intersection of links a, b, c ∈ S and the river w ∈ W. In this study, the failure of a bridge is treated as a Boolean event, although the probability of bridge collapse can be assessed using hazard simulation models combined with appropriate structural analysis techniques (Sassu, Giresini and Puppio, 2017), as highlighted in Chapters 3 and 4. The collapse scenario results in the redirection of traffic volume from one path to the alternative one using a system-optimal assignment. However, the proposed method can also accommodate other traffic assignment approaches, such as the user equilibrium. To illustrate this capability and summarize the workflow, an example is presented using a simple three-link network, as shown in Figure 42. Once the traversal time R has been calculated using Equation (31), the economic costs can be computed to determine which alternative path is the most critical. The computations are performed according the following pseudo-code:

```
For p = 1 to np do //np are the number of paths
        V_detour = Vp //the V_detour is the traffic on closed path Vp
        Updated Volumes = Initial Volumes
        For iteration = 0 to Vp do
                For i = 1 to nb do //nb is the number of bridges
                        If I = p then
                                i = i +1
                        else
                                Traffic Assignment Computation
Compute DIIj
```

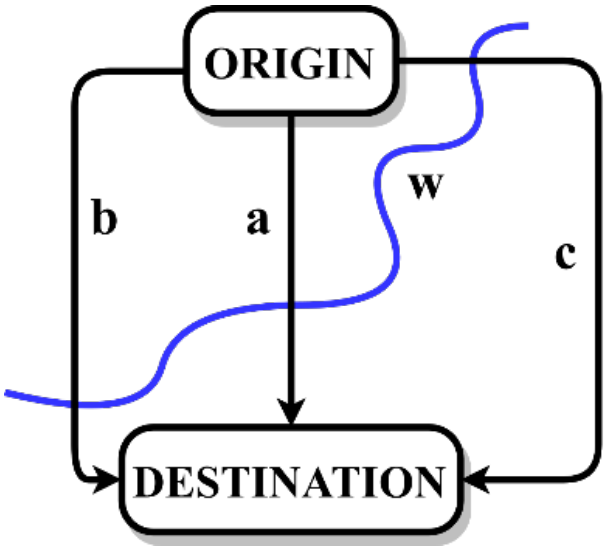


Figure 42. Bridge locations are at the intersections of road links with river

Table 9. Parameters for the network displayed in Figure 42

Source	**Dijkstra GIS**	**Script**	**OTM**	**HCM**	**HCM**	**Equation (30)**
Route	Length	LOS	Capacity	Av. Speed	FFS	Volume
a	2 km	E	800 veh/h	20 km/h	55 km/h	800 veh/h
b	3 km	CD	500 veh/h	33 km/h	65 km/h	420 veh/h
c	4 km	AB	600 veh/h	50 km/h	55 km/h	270 veh/h

During the collapse scenario simulation, the traffic volume from the closed path is redirected to the remaining paths based on the chosen traffic assignment method. From the perspective of the infrastructure manager, minimizing overall system disruption would be desirable, while in a scenario without any intervention, the user optimum assignment reflects the more realistic behaviour of drivers. By considering the data presented in Table 9 and the network configuration depicted in Figure 42, the results of the DII are reported in Table 10.

Table 10. Results, in terms of DII, according to the parameters of Table 9 and the network of Figure 42. Two assignments are included, for comparison purpose

Path A Closed. Detoured Vol. = 800 veh/h	**System Opt. Assign.**		**User Equil. Assign.**	
Alternative Paths:	b	c	b	c
Vol./cap. @ post-hazard conditions	1.13	1.54	1.54	1.2
DII	1.1	4.0	2.4	2.3
Path B Closed. Detoured Vol. = 420 veh/h				
Alternative Paths:	a	c	a	c
Vol./cap. @ post-hazard conditions	1.30	0.75	1.30	0.75
DII	2.6	1.3	2.6	1.3
Path C Closed. Detoured Vol. = 270 veh/h				
Alternative Paths:	a	b	a	b
Vol./cap. @ post-hazard conditions	1.31	0.90	1.21	1.03
DII	3.8	1.1	2.6	1.6

From this straightforward example, it becomes apparent that employing the system optimum assignment intensifies the differences between alternative paths, thereby highlighting critical situations that can arise during a network disruption. Conversely, if the user equilibrium is used, these distinctions are not as easily discernible to local managers, as there are no significant variations in terms of DII. However, this example underscores the versatility of the proposed method, which can effectively accommodate different traffic assignment models. In its current version, the framework can handle one disruption at a time for each path in Rnp. In cases of multiple-link failures, higher DIIs may be generated, and an updated version of the model will include the probability of experiencing multiple disruptions. The DII introduced here serves as a summary measure of the impact that the closure of a specific path has on its users, taking into account the resulting disruptions on other routes and comparing them to the initial network conditions, which may already be congested due to inadequate management. In the subsequent chapter, the performance indicator is applied to a real-world scenario.

7. Road Network Analysis and DII Application

The framework described in Chapter 6 is put to the test in the municipalities of Massa and Carrara, situated in the Tuscany region of Italy. These areas have experienced significant damages in the past decade, as highlighted in Chapter 5. Despite that the 2003 flood was the costliest event ever recorded for the area, the events of 2011 and 2012 left a wider mark on the road network's functionality, leaving a lasting impact. The first disaster occurred in October 2011, in the northern part of the Province of Massa and Carrara, when intense rainstorms led to the collapse of 11 bridges and caused damages amounting to 100 million EUR (Bini *et al.*, 2012). Subsequently, in 2012, a coastal inundation occurred, resulting in the collapse of several bridges and causing 24 million EUR worth of damages. These events, along with the occurrence of other notable bridge failures in recent years (Bazzucchi, Restuccia and Ferro, 2018), have shed light on a previously unknown issue with secondary road bridges, which could potentially have a significant impact (Stochino, Fadda and Mistretta, 2018a, 2018b). Research conducted by Puppio, (2018) revealed that 70% of bridges are situated on secondary infrastructure, with an average density of one bridge per kilometre, and out of these, only 20% are documented in official maps. Consequently, it is not surprising that such bridge collapses have severe consequences for the affected population, leaving entire communities isolated. Thus, given the vulnerability of the Italian territory, the proposed method has been specifically applied in this context.

In the municipalities of Massa and Carrara, a total of 756 crossings are identified through the overlay of road and water networks. However, after considering only the infrastructure along the O-D paths, the number of crossings is reduced to 123. Each settlement within these municipalities is connected to the civil protection headquarters, which is located in the city of Massa. For the purpose of this analysis, the framework is applied to three specific zones: (i) the Avenza area in Carrara, which is connected to suburban freeways to the city of Massa, and (ii) mountain villages within Massa's municipality. The traffic composition in these areas, based on the average number of registered cars and trucks from the driving bureau, consists of approximately 90% cars and 10% trucks in the municipality of Massa, and 85% cars and 15% trucks in Carrara. In the subsequent analyses, the farthest village along each path is assumed as the destination.

7.1. Computation of DII

Between the first zone (Civil Protection Headquarters of Massa) and the second zone (Avenza), a total of seven paths are identified. However, the analysis reveals that only five of these paths involve the potential collapse of a bridge, as depicted in Figure 43. The results in terms of DII are presented in Figure 44. When Path 1 (A) is closed, Path 4 (D) emerges as the most favourable alternative, offering cost savings of 44% compared to Path 5 (E), 66% compared to Path 2 (B), and 100% compared to Path 3 (C). Conversely, when Path 4 (D) is closed, Path 1 (A) becomes the most economically viable option. Therefore, both Path 1 (A) and Path 4 (D) can be deemed as strategic infrastructure since the collapse of any infrastructure along Paths 2 (B), 3 (C), or 5 (E) can be effectively managed through these two routes.

Furthermore, Paths 3 (C) and 4 (D) are found to cause the most significant disruptions overall. Consequently, targeted interventions could be planned to mitigate the indirect costs incurred along these routes. Matrices similar to the one displayed in Figure 44 can serve as valuable tools for supporting network improvements, aimed at minimizing the adverse impacts on detoured users. Thus, following a disruptive event, the connection between the cities of Massa and Avenza can be ensured through several alternative routes, with the DII matrix serving as a practical tool for evaluating the consequences for detoured users.

In a different scenario, where only one alternative path is available for each O-D pair, the analysis focuses on the route from the Civil Protection Headquarters to the mountainous area of Massa, encompassing destinations such as Antona, Resceto, Casette, and Forno. The last three destinations share almost identical routes, resulting in the same collapse scenario. Other settlements in the area are situated along the way to these three villages. For each destination, the analysis reveals a single alternative path, as illustrated in Figure 45. The computation of the DII yields a value of 1.7 when path A is closed and 2.6 when path B is closed. To determine which path is more critical, a comparison of DIIs leads to the conclusion that closing path B would result in costs 53% higher than closing path A. While this comparison may initially seem irrelevant due to the differing destinations, it is important to note that the alternative paths are mutually exclusive, as shown in Figure 45. Consequently, since the diverted traffic volume is equal in both paths, path B is deemed more critical than path A, as it corresponds to a higher DII.

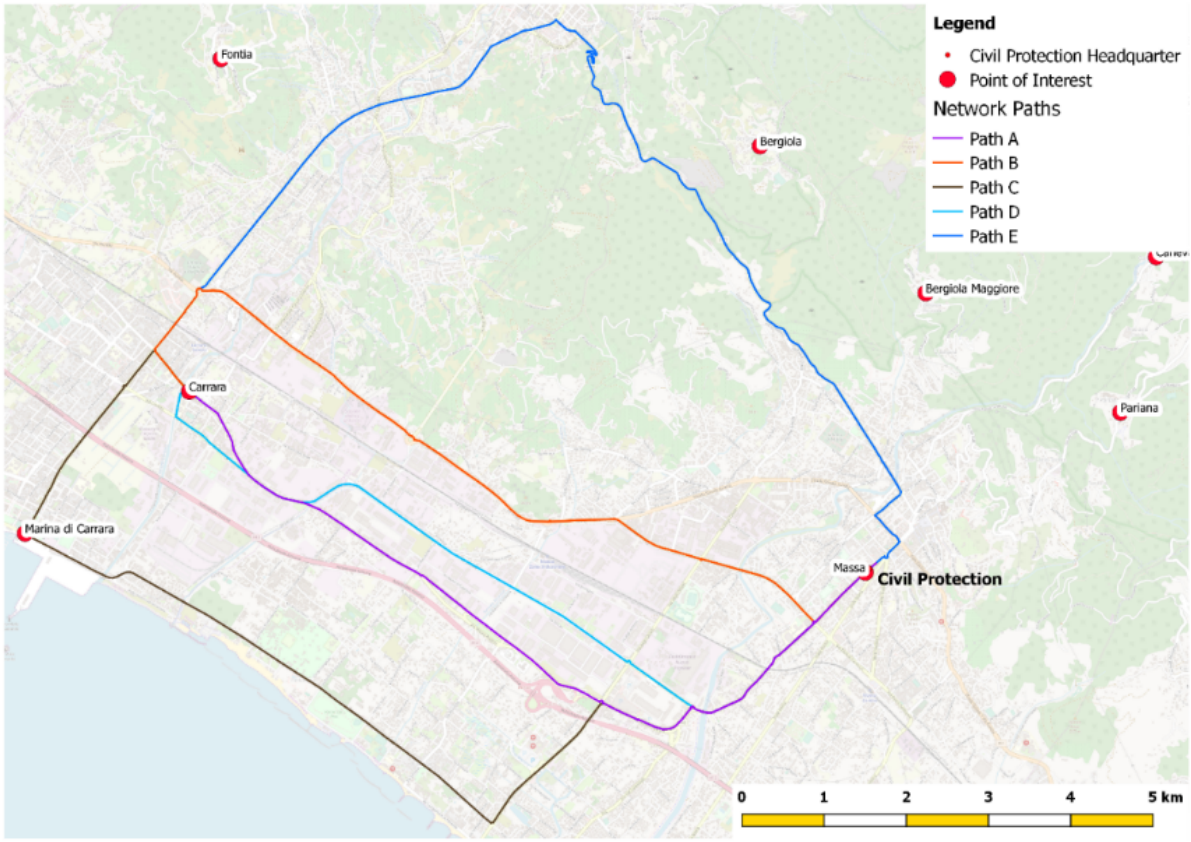


Figure 43. Identified paths between the Civil Protection Headquarter in Massa to the village of Avenza

DII		OPEN PATHS				
		Path 1	Path 2	Path 3	Path 4	Path 5
CLOSED PATHS	Path 1		5.3	6.4	3.2	4.6
	Path 2	2.5		6.3	3.1	4.1
	Path 3	1.7	3.3		1.9	2.8
	Path 4	3.2	6.3	7.4		5.2
	Path 5	2.1	4.2	5.3	2.5	

Figure 44. The DII Matrix for the paths highlighted in Figure 43

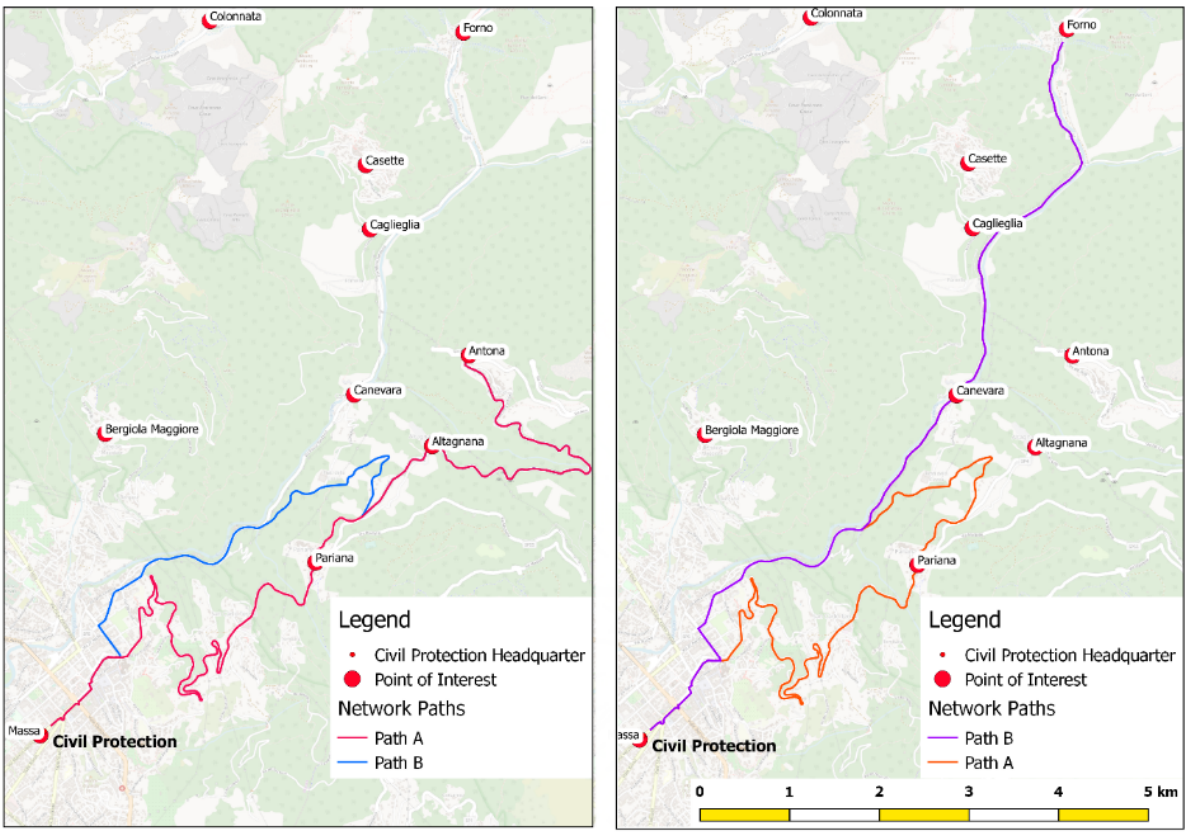


Figure 45. Identified paths between the Civil Protection Headquarter in Massa to the villages of Forno on the right and Antona on the left

7.2. Validation of the Framework

The model validation involves a comparison between the travel times obtained from the proposed procedure under normal conditions and the travel times provided by Google Maps. Both analyses utilize the same set of traffic data records. A statistical descriptive analysis of the sample reveals that the variability of errors falls within the range of 0% to 40% for the lower bound interval, and from 0% to 33% for the upper bound. To further analyse the data, the sample is divided into suburban and mountainous paths, allowing the two measurements to be treated as independent variables. In order to compare the error between the estimated time of arrival (ETA) calculated using the proposed procedure (ETAmethod) and the ETA derived from web-based maps (ETAweb), Equation (32) is employed.

$$Error = |\, ETA_{method} - ETA_{web}| \tag{32}$$

The findings presented in Table 11 demonstrate that the lowest errors, specifically 4.3% and 5.6%, are observed at different ends of the Google Maps ETA range. This suggests that the model's ability to explain the percentage of traffic varies significantly between suburban and mountainous regions. In suburban areas, the average ETA aligns more closely with the upper bound of Google Maps ETA, while the opposite trend is observed in mountainous areas. This discrepancy implies that the model tends to underestimate indirect costs in highland regions compared to suburban areas. Despite these limitations, it is noteworthy that the results are satisfactory, with low errors (below 5.7%) recorded in both areas.

Table 11. ETAs for the present framework and the ETAs based on the web maps

Statistics of errors		**Suburban**	**Mountainous**
Compared to Lower bound of Google Maps	Upper 95% confidence interval	39.4%	12.1%
	Mean error	32.1%	**5.6%**
	Lower 95% confidence interval	24.9%	0.9%
Compared to Upper bound of Google Maps	Upper 95% confidence interval	8.3%	32.0%
	Mean error	**4.3%**	27.2%
	Lower 95% confidence interval	0.3%	22.4%

8. Main Findings

This study covers specific themes of a research line aimed at assessing and prioritising interventions on bridges. This Chapter focuses on findings and elements of discussion for each topic. Paragraph 8.1 discusses the analysis of evidences in the aftermath of the 2021 flood in Germany, supporting also the need for methods to predict overlooked phenomena such as hydraulic forcing and driftwood clogging on bridge decks. Therefore, in Chapter 4 an analytic method to compute fragility curves of bridge decks subjected to hydraulic forcing and driftwood blockage is presented. Consequently, in § 8.2 the main findings of the work presented in Chapters 4 and 5 are summarised. The issue at asset level is demonstrated to also have network-wide impacts, with indirect consequences playing a key-role in the disruption to road users. This theme is discussed in Chapters 6 and 7, being the findings commented in § 8.3. The last §, 8.4, is dedicated to the analysis of interdisciplinary themes presented across this Thesis, focusing on a mathematical model to link the asset-level failure to its network-level impact.

8.1. Findings on Empirical Fragility Curves

Fragility curves constitute a pivotal component in the financial risk assessment of the existing inventory of bridges. Chapter 3 of this Thesis undertook the task of developing fragility curves grounded in empirical failure data. These data were sourced from a variety of outlets, encompassing damage reports submitted by local authorities, bridge condition inspections, and information compiled from surveys conducted following the 2021 flood in Germany. The modelling framework utilized was an adaptation of the FEMA P-58 document (ATC, 2018), tailored to address flood-related scenarios.

The selected intensity measure, denoted as h**, was chosen based on the availability of relevant data. It measures the ratio between the water stage upstream of the bridge and the elevation of the deck. The flood event itself was reconstructed with the aid of an established 2D model by Apel, Vorogushyn, and Merz (2022), specifically applied to the Ahr river in Germany. This model was fine-tuned through calibration against the hydrograph data provided by LfU (Landesamt für Umwelt Rheinland-Pfalz, 2022). The classification of damage levels was built upon the semantic descriptions outlined in DIN 1076 bridge

condition ratings (Haardt, 1999), coupled with the ranking methodology employed in empirical fragility models (Padgett, Spiller, and Arnold, 2012; Anderson *et al.*, 2017). To evaluate the goodness of fit, the Lilliefors' test was employed, and Peirce's criterion was utilized for the management of outliers. The failures were categorized based on the damage mechanism, differentiating between scour and hydraulic forcing. While the influence of debris obstruction was acknowledged, its quantification was not feasible due to data limitations. Subsequently, bridges were classified into clusters based on observed patterns linking damage mechanisms and deck materials, separating lightweight structures (LWY) from their heavier counterparts (HVY). Additionally, bridges were grouped based on their structural typology, further distinguishing between beam decks and arch bridges.

The research findings revealed a notable disparity in the susceptibility to collapse between beam bridges and arch bridges when subjected to overtopping. Furthermore, within the category of beam bridges, a further subdivision became necessary. Notably, lightweight beam decks exhibited an increased vulnerability to hydraulic forcing in contrast to their heavier counterparts. Despite this, beam bridges presented a lower incidence of damage overall compared to arch bridges, primarily due to their reduced obstruction of water flow. It is imperative to highlight that beam bridges displayed a greater likelihood of collapse, but incurred in lower mean damage levels. In contrast, the empirical evidence gathered from actual failures indicated that arch bridges were less prone to collapse when subjected to high hydraulic forcing, typically exhibiting slight to moderate damage instead. In addition, it is essential to underscore the ongoing debate within the academic community regarding the magnitude of hydraulic uplift forces acting on arch bridges, as delineated in § 3.4 of this study. When considering scour as the primary triggering mechanism for collapse, beam bridges tended to experience collapse more frequently, while arch bridges exhibited a more robust response, frequently resulting in moderate damage. Nevertheless, it is important to note that beam bridges sustained lower rates of damage attributed to scour when compared to arch bridges, thereby corroborating the earlier observed trend in their vulnerability to hydraulic forcing. Table 12 and Table 13 summarise these findings in a qualitative way.

*Table 12. Hydraulic forcing vulnerability levels in qualitative terms for lightweight (LWY), heavy (HVY) beam bridges and arch bridges. Symbols (+) to (++++) represent increasing vulnerability to hydraulic forcing. The damage levels D2 (slight), D3 (moderate), D4 (severe) are defined according to § 3.2.2 and h** according to § 3.3*

Typology	**h****	**Damage level due to hydraulic forcing**		
		D2	**D3**	**D4**
LWY Beam Bridges	< 1			
	> 1			+++
HVY Beam Bridges	< 1	++++		
	> 1	+++		+
Arch Bridges	< 1	++++	+	
	> 1	+++	+	

*Table 13. Scour vulnerability levels in qualitative terms for lightweight (LWY), heavy (HVY) beam bridges and arch bridges. Symbols (+) to (++++) represent increasing vulnerability to scour. The damage levels D2 (slight), D3 (moderate), D4 (severe) are defined according to § 3.2.2 and h** according to § 3.3*

Typology	**h****	**Damage level due to scour**		
		D2	**D3**	**D4**
LWY Beam Bridges	< 1			+
	> 1			+++
HVY Beam Bridges	< 1			++
	> 1			+++
Arch Bridges	< 1		++	++
	> 1		+++	++++

The outstanding issue, which remains open and requires further exploration, pertains to the numerous bridges in Germany and across Europe sharing similar characteristics with those that suffered damage but did not face the same IM magnitude that led to the observed damages. This analysis has shed light on the multifaceted nature of the causes behind the high incidence of bridge collapses. On one hand, the escalating impacts of climate change are amplifying both the frequency and magnitude of extreme climatic events, thereby subjecting structures to unforeseen forces. On the other hand, these failure mechanisms, such as overtopping and uplift, pose a substantial hazard to the inventory of bridges.

Presently, Eurocode 1 encompasses a specific limit state addressing horizontal water thrust on bridge decks, albeit just during the construction phase (CEN, 2005a). Indeed, in the context of the in-service bridge inventory, safety is primarily ensured by maintaining a prescribed clearance above the 100 or 200-year flood levels. However, empirical evidence has underscored the limitations of the current deterministic approach, particularly in light of the substantial uncertainties associated with peak discharges driven by climatic changes. This has reinforced the need for a move toward adopting a probabilistic or semi-probabilistic approach when computing hydraulic forcing acting on bridges.

8.2. Findings on Bridge Deck Vulnerability

Fragility curves offer insights into the probability of exceeding specific limit states across various levels of hazard magnitudes. Currently, there is a gap in flood fragility investigations that incorporate hydrodynamic effects regarding single-span decks, as scholarly attention is predominantly directed towards multi-span configurations, with a primary focus on piers. A notable lack in the present literature pertains to the fragility of bridge decks, particularly with respect to the impact of driftwood clogging. However, considering both bridge failures and post-event experimental campaigns, it is unravelled the pivotal role played by driftwood blockage on bridge decks.

This study integrated the abovementioned findings from flume experiments of Kerenyi *et al.* (2009) into a probabilistic framework, employing the developed BrHyD program presented in § 4.3. The research introduced a novel approach to obtain fragility curves specifically tailored for single-span bridges, accounting for hydrodynamic forcing and considering the likelihood of driftwood clogging. The investigation explored three critical limit states: slippage, uplift, and overturning, underlining the absence of uplift and overturning in the EN1991:2005, despite their consideration in other standards, such as the AS5100:2017.

In addition, the work emphasized the crucial role of recalibrating hydrologic models due to climate change effects. Particularly, alterations not only related to climate but also to land use modifications can lead to notable variations in safety levels. Alongside with hydrologic models, at river level the identification of the most influencing factors on the response of structures to water forcing is of paramount importance.

Specifically, the case-study presented in Chapter 5 highlighted not only the effect of a hydrologic factor, as the AMC, but also the backwater rise caused by a downstream structure in close proximity. Without the application of a hydraulic model, this effect might have been overlooked. Finally, the study

delved into the investigation of driftwood jams on bridge decks, revealing a substantial escalation in failure probability as clogging progresses.

Some shortcomings of this study are related to assumptions made about the absence of bearings and a simplified clogging process, which involves simulating an increased deck thickness. Indeed, this approach represented a worst-case scenario as it did not account for the porosity of log mats. For a more comprehensive analysis of driftwood clogging, it is recommended to utilize specialized tools (Quiniou *et al.*, 2022).

In broader terms, at asset-level the research outputs stressed the significance of considering hydrodynamic forces and driftwood in the design and management of single-span bridge decks. At network-level the method and its application are presented in Chapters 6 and 7. Then, the results are summarised in the next Paragraph.

8.3. Findings on DII Metric and Framework

Past events revealed the importance of the usability of a road network following a bridge collapse. This aspect is particularly critical for rural and suburban areas, where the failure of a seemingly insignificant infrastructure can lead to the isolation of entire communities. Moreover, rural areas often face challenges in terms of data availability, especially when it comes to traffic data. Existing approaches may be limited in their applicability due to these data constraints. Additionally, traditional road performance indicators rely on generalized cost functions for users, without explicitly considering factors such as trip purpose, traffic composition, and vehicle operational costs.

To address these issues, this work proposed a novel aggregate metric defined as DII. This performance indicator combined established impact metrics with an innovative algorithm to tackle the challenges specific to rural contexts. The method not only resolved the issue of traffic data availability through a new hybrid web-theory approach but also introduced a delay-cost function (DC) and a vehicle's operational cost (VOC). This enabled the explicit consideration of factors such as the driver's time cost function, trip purpose, and traffic composition. The proposed method represented a pioneering attempt to integrate data availability challenges, road disruptions, and the evaluation of users' specific consequences.

However, it is important to acknowledge the limitations of the method, which are addressed in the study. One of such assumptions is the use of the mean Level of Service (LOS) velocity as the traffic

speed during the conversion from qualitative to quantitative data. Despite this hypothesis, experimental results demonstrated a good agreement with predicted values, indicating the acceptability of assuming the mean speed for each LOS as the mean speed of vehicle flow. Moreover, the street class was identified as a critical parameter in this assumption, as different street categories have distinct speed ranges. These ranges, based on semi-empirical studies, are summarized in specific tables in the HCM. It is reasonable to assume that speed values on streets follow a normal distribution, with the mean value being the most frequent. This can explain the method's effectiveness in real-case scenarios.

It is important to note that this procedure did not replace more reliable traffic counters. However, it provided an initial quantitative estimate of traffic on roads where no traffic data is available. Each path was classified as more or less critical to the network based on a single-link failure. This approach may led to the underestimation of DIIs, since a multi-link disruption would resulted in higher values. In situations involving multiple disruptions, a different method, such as a probabilistic approach, should be considered to reasonably account for the worst-case scenario probability.

In conclusion, the proposed framework represented a significant step towards addressing the challenges associated with road network usability and detour impacts in rural and suburban areas. By leveraging innovative methods for data collection, incorporating specific cost functions, and considering the unique characteristics of rural contexts, this framework offered a valuable tool for assessing and mitigating the consequences of disruptions in a transportation system.

8.4. Discussion on Interdisciplinary Themes

Concerning interdisciplinary themes, main discussion topics are covered within this Paragraph. Concerning Chapter 3, it provides fragility curves that can be employed in decision-making and catastrophe modelling frameworks. Chapter 4 highlights the benefits of accounting additional Limit States (LS) in bridge design and management. Instead, the framework developed within Chapter 6 can be easily extended to other hazards such as fires, earthquakes, and human errors.

The link between the bridge network disruption and the asset-level probability of failure can be seen by analogy, schematising the network as an electric circuit, having bridges as resistances. According to Figure 46, the formulae to compute the network probability of failure accounting for the asset’s ones, are computed as follow:

$$P(F_{ser}) = P(F_1) + P(F_2) - P(F_1F_2) \tag{33}$$

$$P(F_{par}) = P(F_1F_2) \tag{34}$$

$$P(F_1F_2) = P(F_1) \cdot P(F_2) \tag{35}$$

Where F_{par}, F_{ser} are the failure events of a parallel and a series system, respectively. By analogy, F_1, F_2 are the failure events for bridge 1 and 2, which are displayed in Figure 46. Equation (35) stands if F_1 and F_2 are statistically independent events; conversely Equation (36) must be employed.

$$P(F_1F_2) = P(F_1 \mid F_2)\, P(F_2) \tag{36}$$

The independence of collapse events should be ensured by a dedicated hydraulic analysis. This is due to the morphology of the river network. As an example, if bridges 1 and 2 belong to the same river, there might be a hydraulic interaction between the bridges; i.e., through backwater or damming effects. In such cases, the collapse of a bridge influences the probability of failure of the other one: $P(F_1 \mid F_2)$. This fact can be also seen in past collapses (see Chapter 3).

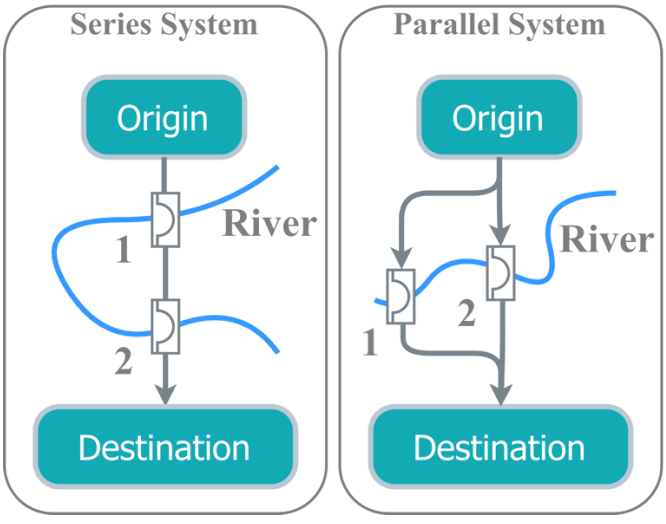


Figure 46. Bridges in series and bridges in parallel. With numbers 1 and 2 representing the bridges

8.4.1 Discussion on the Drag Coefficient Comparison

Within the literature review reported in Chapter 2, a comparative analysis of investigations carried out on flume experiments in the last two decades is presented. The differences and analogies are discussed about the drag coefficient C_D which accounts for the magnitude of the horizontal component of hydrodynamic thrust on bridge decks. Several key parameters are selected and analysed in detail: the inundation ratio h^*, proximity ratio P_R, blockage ratio B_R, deck thickness and shape. Results showed a significant effect of blockage and inundation ratio on the dragging coefficient, while a milder impact is evidenced for the deck width-to-thickness ratio. Regarding P_R, higher hydrodynamic actions are expected for low deck clearances. The relationships shown in § 2.1.2, indicate that existing literature studies can support a more robust code-based design, to fill existing gaps in current standards. By the joint comparison of several results, an influence domain is drawn with respect to the influence of B_R on C_D. Indeed, the chart of Figure 8 can be used during the preliminary design or on the assessment of existing bridges, to assess whether the bridge is exposed to violent drag force. This might represent a shift of perspective that should be included in EN1991-1-6:2005, to benefit from the large number of experimental results from existing research projects.

Considering a constant drag coefficient and neglecting C_L and C_m, as in EN1991-1-6:2005, has some drawbacks: (i) a possible higher C_D due to P_R and B_R influence; (ii) unaccounted higher normal force on bearings and foundations due to negative C_L at early submersion stages; (iii) neglected forces on bearings due to C_m, which accounted for the deck rotation mechanism; (iv) ignored uplift and overturning failure mechanisms.

Nevertheless, the literature review also evidenced that some studies had a limited comparability due to different test procedures, which in turn affected the results. In addition to this comparative approach, it is pointed out the need of further research activity on the hydrodynamic actions on bridge decks.

Although numerous experimental campaigns are investigated, only the one from Kerenyi *et al.* (2009) included CFD simulations to extend the validity of their findings to a wider range of conditions. Indeed, flume test campaigns, should be followed by CFD simulations, to accurately investigate intermediate conditions. Still, performing only CFD simulations is not enough, as the model must be calibrated on experimental results. This is the rationale behind the choice – in the present work – to base the hydrodynamic coefficient computation on the work of Kerenyi *et al.* (2009). Nevertheless, the validity of extensive campaigns such as the one carried out by Jempson (2000) has been widely recognised in

both academia and practice, as it was used to define the envelope lines presented in the Australian Bridge Design Code AS5100.

8.4.2 Discussion on Hydraulic Forcing and Driftwood Clogging

At asset-level, three failure modes for bridges at high water stages are investigated, leading to the following Limit States, namely slippage, dragging and overturning of the deck. Past works are not in agreement with the collapse mechanisms occurring for arch bridges. This concerns an issue with the uplift coefficients. Failure modes indicated in the work of Falconer *et al.* (2010), in which a positive uplift leads to arch failures is not in agreement with results of flume experiments obtained by several authors (Jempson, 2000; Kerenyi, Sofu and Guo, 2009; Oudenbroek *et al.*, 2018; Dean, 2020). Indeed, the contraction of the flow under the arch at overtopping water stages leads to a decrease in water pressure and consequently an increased velocity. This phenomenon generates negative values of hydrodynamic uplift, as demonstrated by flume experiments. A possible issue concerns higher submergence ratios, where the uplift coefficient tends to zero. However, in such cases, the overtopping water also acts with its weight on the bridge deck, stabilising the arch. Evidences to support the occurrence of this mechanism can be seen by standing arch bridges in Ahr valley, which suffered overtopping during the 2021 flood (Grates, 2023)

Concerning beam bridges, analysing the failure mechanisms of decks even without considering the effect of bearings is a valid assumption only for short-span ones where no bearings are installed. In all other cases, this assumption might lead to inaccurate results. To shed light on this point, in the present work data availability of bearings' constitutive laws was an issue, as these devices are patented technologies. However, the method succeeded to demonstrate the feasibility and implications on the bridge safety resulting from hydraulic forcing. Moreover, the study pointed out the decreased safety due to driftwood accumulation. Regarding this last point, within the surveyed bridges in Ahr valley, it was impossible to assess the amount of driftwood accumulated at decks at the time of each bridge failure, as the extreme nature of the event hampered any direct measurement; in other situations, local flooding of small creeks, allowed for direct measurements, revealing driftwood clogging up to 3 m below the water surface (Lebbe *et al.*, 2014).

The analytical method to compute fragility curves is complementary to the empirical one. However, a direct comparison among the two was not possible, as the damage data collected in the Ahr valley included an unknown amount of clogged debris. Therefore, the bridges' probability of failure

highlighted in the empirical FCs (in Chapter 3) comprised the damming effect of driftwood and other materials. Despite the analytic method cannot be yet validated by using empirical data, it is composed by validated flume test data in key-factors such as the hydrodynamic thrust magnitude and the driftwood blocking probability. In addition, it employed a validated hydrologic and hydraulic model of the case-study structure. Moreover, the use of a dedicated hydraulic model helped to perform simulations under different hazard conditions.

8.4.3 Discussion on Modelling Features

Concerning the bridge geometry, since the framework is designed to be applicable only to single-span bridges, the influence of driftwood clogging on piers is not assessed. However, HEC–RAS software already accommodates driftwood accumulation at piers, leaving the impact on decks still a gap. Therefore, in the work described in Chapter 4, the missing feature is included by adopting the idea to increase the bridge thickness to simulate the mentioned accumulation process. The HEC–RAS model employed in Chapter 5 consisted of a 1D steady flow plan. This is a limitation and an inaccurate assumption when considering rivers with high sinuosity (meanders) as in the case-study, a 2D model better represents the river hydraulic. In addition, the 1D wood log accumulation must be discussed. Indeed, the driftwood blocking probability is computed using results of experimental campaigns; in this sense, the clogging event within HEC–RAS is taken as a certain event (the girder soffit is deterministically lowered) and only afterwards the overall stochastic wood log entrapment process is accounted by using results of flume experiments as marginal probability. The same logic applies to the hydrodynamic component of the hydraulic forcing, by using results of tests on hydrodynamic coefficients. Concerning the latter, this thesis discusses the effect that an equivalent static action of a dynamic phenomenon has on the structure. This can be possible as hydrodynamic coefficients are retrieved from tests as values of sensors' readings averaged on a predefined timeframe (e.g., 50 seconds) in order to avoid effects of turbulence. On the other hand, applying a dynamic input to the structure would have required the use of SDOF and MDOF models.

8.4.4 Discussion on Road Network Disruption

Regarding the asset-level framework, the traffic-gathering algorithm used in rural roads and suburban areas is a solution to data availability, while the generation of disruption scenarios underlined the importance of such a secondary road network within the catastrophe response for emergency vehicles and isolated communities. Challenges mainly comprise: (i) the definition of streets' capacities; (ii) the calculation of free-flow speed; (iii) the definition of trip purpose. Concerning the first point, the capacities of streets in terms of vehicles/hour are retrieved through the Open Transport Map (OTM). This project comprises a database with Average Daily Traffic (ADT) measurements for the whole Europe. Nevertheless, ADT is computed only for main roads, resulting impossible to determine it on rural ones. This issue is then solved through the developed traffic gathering algorithm. On the contrary, the capacity of each road link is available on OTM and computed based on the road class. Then, using the HCM, the free-flow speed is computed. Hence, by joining the information provided by OTM and HCM, it is possible to create for each link a set of values comprising free-flow speed and capacity (veh/h).

Lastly, the users' trip purpose is included within the costs' evaluation according to the work of Gervásio and da Silva, (2013), in which business trips have a significantly higher cost than non-business ones. This is highlighted in Chapter 6, with DTC parameter. Then, the cost increment in alternative paths is normalised to the closed one during normal condition, as this allowed to assess the impact from the perspective of users who were using the closed path, prior to the bridge collapse. If the DII formula was H_i/NH_i, the perspective shifted towards the regular users of the i-th path; indeed, in this case, existing disruption metrics as the NRI (Scott *et al.*, 2006), can be used instead.

Concerning the overall costs computation, a validation is rather difficult even with costly solutions due to several variables such as the monetised value of time to be assigned for the users' delay costs and those related to the vehicles' usage, namely the VOC. Regarding the method validation, which is performed in pre-hazard conditions, it is acknowledged that it would be beneficial from a post-hazard verification. However, during the development of the framework the main concern was the reliability of qualitative web-based traffic data. Indeed, it was deemed necessary to quantify the error between the Estimated Time of Arrival (ETA) calculated using traffic data gathered using smartphone's locations, elaborated through an analytical procedure and the web-based computed ETA. Therefore, the validation mainly focused on this aspect. The robustness of the method is ensured by HCM and related equations. Nevertheless, the effectiveness of using DII to assess flood scenarios impacts remains uncertain, although the benefits related to this approach are highlighted.

9. Conclusions

Collapses due to floods still represent the main cause of bridge failures. This work developed a framework to compute asset-level failure probabilities due to water forcing and driftwood accumulation at bridges. This thesis also discussed the impact of disruptions of roads at network-level. To achieve these goals, at asset level the local hydrostatic and dynamic components of the water flow were analysed, identifying also current gaps in standards for the respective Limit States. In addition, the damming effect of wood logs on bridge deck was accounted for in the computation of fragility curves. On the network side, roads disruptions and traffic data availability were discussed to quantify the impact of a bridge closure on the transport system. At each level – asset and network– a computer program was developed to speed up calculations and to fill modelling gaps of existing software.

9.1. Main Outcomes

Chapter 3 investigated actual failures from a database comprising 250 bridges by retrieving official post-disaster inspection sheets and performing in-person surveys. The retrieved data was statistically analysed, shedding light on bridge condition ratings. Subsequently, conclusions were drawn through a fragility analysis. Specifically, heavy decks – comprising reinforced concrete and masonry structures – resulted more robust at severe damage levels facing hydraulic forcing compared to lighter ones, made of wood or steel. These lightweight decks did not exhibit slight and moderate damages, due to the lack of robustness facing hydrodynamic forcing. Conversely, heavy decks also sustained minor damages, but a distinction could be made on the triggering mechanism. Indeed, scour was more likely to produce severe damages when compared to hydraulic forcing. For example, at overtopping ($h^{**} = 1$), the probability of reaching or exceeding a moderate damage was respectively 80% in case of scour and 36% for hydrodynamic thrust for heavy beam decks (HVY), as per Figure 20.

Bridges were also clustered based on the typology: results showed that arch bridges exhibited a more robust behaviour than any other bridge type under overtop. The main issues for arches concerned scour and driftwood clogging, having more severe impacts compared to beam bridges. Evidence from the 2021 Flood in Germany showed that wood logs accumulation against decks triggered many collapses.

Driftwood clogging is often deemed a moderate concern for practitioners, while this work (through both analytic vulnerability model and evidence) demonstrated the importance and severity of this phenomenon.

The analytic model developed in Chapter 4 provided practitioners for readily available approaches to compute unaccounted Limit States in the current version of EN 1991 (CEN, 2005a). The proposed approach used a modular framework (Figure 24) able to perform analyses with increasing complexity, allowing also for probabilistic approach. Specifically, results of flume experiments were used to derive hydrodynamic coefficients and the driftwood clogging probability. That greatly improved the accuracy of the present framework, as it did not totally rely on numerical simulations. Results showed that in the early stages of deck submersion, foundations have to be checked against increased normal force due to the effect of water flow under the deck. Then, this phenomenon was mitigated by the static component of the flow at higher submersion stages.

The framework was also capable of determining whether deck dragging was the most severe Limit State, as different bridge typologies could show the relevance of uplift and overturning mechanisms. To shed light on this point, when shear keys are in place at bearings, uplift and overturning can easily become the triggering failure mechanisms. The need to account for such Limit States in future versions of Eurocode 1 was therefore stressed.

Additional issues concerned the hydrologic and hydraulic models employed. Results demonstrated the key-role of hydrologic model recalibration. Indeed, reducing peak discharge by about 6%, led to 33% decrease in deck's failure probability.

The same approach is applicable to situations in which changed climatic conditions led to increased discharge and therefore a reduction in bridge safety. Therefore, at asset level outcomes of the study demonstrated that the relationship between hydraulic forcing and bridge deck vulnerability is complex and poorly accounted in current codes, such as Eurocode 1. The findings demonstrated how to properly assess the impact of hydraulic forcing, including driftwood clogging by using software used in current engineering practice, appropriately combined with in-house developed Python scripts. Specifically, increments of driftwood accumulation at decks led to a nonlinear decrease in deck's probability of failure as a result of the interaction of static and dynamic components of water flow.

The framework comprised also a network-level assessment due to bridge failures in the aftermath of a flood event. It compared the users' additional travel time on a detoured path to the pre-event conditions. The method was tailored for rural roads, which posed additional challenges such as traffic data availability and free flow speed computation. The method tackled these issues by developing a traffic-gathering algorithm and related equations. Findings demonstrated that the metric – called DII – was able

to rank alternative paths based on single-link failures. Other key variables representative of indirect costs such as vehicles' operating costs (VOCs) and user-cost functions based on trip's purpose (i.e., business and non-business) were discussed.

Both methods, at asset and network level, after highlighting current gaps, developed possible solutions for the mentioned issues. Therefore, the findings unravelled feasible strategies to help bridge managers and practitioners in their decision-making processes.

9.2. Research Innovations

The following innovations were included in this work:

- Empirical fragility curves for riverine bridges in Europe:

  Empirical fragility curves due to water actions were computed mainly for hurricanes. This study instead, collected evidence from 250 bridges in the aftermath of the 2021 flood in Germany to perform a fragility analysis. The curves linked the normalized water elevation to the probability of exceeding several degrees of damage, which were determined based on post-hazard inspections.

- A novel framework for hydrodynamic actions and driftwood clogging against bridge decks:

  A novel framework to assess the impact of hydraulic forcing and driftwood actions was developed. In contrast to existing approaches, the bridge vulnerability was evaluated against varying discharge levels, accounting for several driftwood clogging scenarios. This allowed to demonstrate current gaps in codes, as the EN 1991:2005 (CEN, 2005).

- Network-level disruption assessment framework:

  In order to solve traffic data availability and explicitly consider users' costs in the aftermath of a flood event, an innovative method was developed. The framework provided managers with tools and algorithm to estimate the indirect costs and an aggregate metric called DII.

9.2.1. Empirical Fragility Curves for Riverine Bridges in Europe

Evidence collected from 250 bridges in the aftermath of the 2021 flood in Germany, revealed recurrent failure mechanisms, highlighting the need for a different design and management strategy of the bridge stock. Currently, the safety of bridges facing peak discharges is ensured by a clearance on top of the 100- or 200-year return period flood. However, the influence of clogged driftwood, debris and climate change scenarios was neglected. These factors significantly contributed to failures in the 2021 flood through backwater and damming effects. This led to unforeseen actions on bridge decks, causing severe damages. In addition, the presence of manmade obstacles within the riverbed, e.g., a parking lot, in Altenahr, increased the water velocity under existing bridges, causing erosion and a narrower section with an increased risk of debris damming.

The influence of bridge characteristics on the expected damage level caused by a certain water elevation, was highlighted. The analysis of collapsed structures supported the need for reconsidering hydraulic-related Limit States in current codes and standards. In addition, having diverse bridge typologies along the same river allows for improved network robustness, as diverse typologies showed different vulnerability levels for a given water elevation. Statistical analyses on the 250 collapsed bridges revealed relationships between structural characteristics and damage levels. Specifically, conclusions on robustness could be drawn by comparing damage levels among different bridge typologies, representing the first contribute of this type for riverine bridges in Europe. In the future, expanding the collapse database will allow to refine the fragility curves by updating the existing ones.

9.2.2. Hydrodynamic Actions and Driftwood Clogging at Bridge Decks

Driftwood accumulation against piers using hydraulic modelling software such as HEC–RAS can be simulated, while it is not possible to assess log accumulation at decks. In addition, the water action at bridges can be modelled using Computational Fluid Dynamics (CFD). However, a calibration of the model according to experimental results must be performed, as the interaction of structural elements with the free flow surface of water is a complex phenomenon. Therefore, it is usually more cost-effective to use a static representation of the dynamic phenomenon, by using results of flume experiments. Thus, existing bridge design codes define slippage (drag), uplift and overturning Limit States, to account for the hydraulic

forcing. However, the context is rather fragmented, given the absence the mentioned Limit States in Eurocode 1, while are accounted in the LFRD Bridge Design Specifications (USA) and Australian Standards (AS5100:2017).

In this study HEC–RAS capabilities were expanded through the inclusion of driftwood clogging against decks. In addition, automatic procedures were offered to account the overall hydraulic vulnerability of bridges. The framework is a step forward current practice by addressing unforeseen actions through a holistic assessment tool. In addition, climate change effects were included to highlight the impact of hydrologic model recalibration on the bridge deck's structural safety.

9.2.3. Network-level Disruption Assessment Framework

Transport networks are highly susceptible to disruptions caused by flood events, making flood preparedness crucial for mitigating the impacts on infrastructures. Of particular concern is the vulnerability of bridges to water-related actions, which have been identified as a primary cause of bridge collapses. In rural areas, the failure of bridges can have severe consequences, leading to the isolation of entire communities due to the lack of redundancy in the road network.

To effectively assess flood-disruption scenarios and identify critical bridges, accurate and reliable models representing the actual traffic conditions are essential. These models rely on demographic and traffic data, providing the foundation for conducting disruption simulations and evaluating the potential impacts on the road network.

However, one major challenge in rural areas is the limited availability of traffic data. To address this issue, the algorithm proposed in this study offered a solution to gather quantitative traffic data from qualitative web-based information. By leveraging insights from the HCM and street capacities provided by the OTM project, a novel method was developed. This method not only overcame the data scarcity challenge but also introduced a new disruption metric known as the DII. The DII explicitly accounted for the costs incurred by drivers and vehicles, considering factors such as travel time and operational expenses.

The tool developed in this study was implemented within a GIS environment, offering flexibility and integration with existing routing plugins. This enabled seamless incorporation of the proposed method into existing frameworks, enhancing the overall capabilities for assessing network disruptions and their impacts.

Although significant progress has been made in this study, several challenges and uncertainties still remain. Further efforts are required to reduce uncertainties, refine the method, and enhance its accuracy. This includes addressing factors such as varying traffic conditions, improving the understanding of failure mechanisms at the asset level, and gaining a deeper understanding of the impacts of network disruptions.

Overall, this work represented an important step forward in improving our understanding of the key elements related to failure mechanisms at the asset level and the impacts of network disruptions. By integrating innovative approaches, such as the algorithm for gathering traffic data from web-based information and the introduction of the DII, this study provided valuable insights into assessing and managing disruptions in transport networks, particularly in rural areas prone to flood events.

9.3. Impact of the Research

According to RiskLayer CATDAT, floods impact approximately 120 million people worldwide, making it a significant global concern. Among the various causes of major failures, bridge collapses resulting from floods are ranked at the top. With the anticipated effects of climate change, the stress on infrastructures is expected to increase, driven by the intensification of extreme weather events. The occurrence of 250 bridges damage during the 2021 flood in Germany served as evidence supporting the urgent need to revaluate hydraulic design and bridge assessment approaches. Furthermore, it emphasized the importance of considering bridges as part of a broader framework to account for cascading effects on the road network. By doing so, critical situations such as the isolation of communities could be avoided, while ensuring the provision of safe routes for emergency vehicles. This work highlighted these issues and proposed several solutions to address them effectively.

The practical tools developed in this study have the potential to significantly impact various sectors and stakeholders involved in flood resilience efforts, as described in the following subparagraph and highlighted in Figure 47.

Engineers

The asset-level analysis provided insights and additional Limit States for hydraulic forcing and driftwood clogging. The method expanded the capabilities of hydraulic modelling software such as HEC–RAS by integrating wood log accumulation at decks and offered an automatic procedure to assess the bridge hydraulic vulnerability using varying discharge levels. The analysis used results of flume

experiments to compute hydrodynamic coefficients for a given water elevation, as well as driftwood blocking probability tests to address the reduction in failure probability for a given drifting wood log.

Local authority

The study offered tools for both asset and network level issues, whose interaction can be coordinated by local authorities. Indeed, different actors can be involved, e.g., bridge owner, road network operator, state roads organisation. Therefore, outputs at different level of detail can help decision-makers in response measures. Each step was thought to be used with currently available software and open-source tools, for an easy integration in companies' practices.

Transport Modeller

Network-level issues such as traffic data availability in rural areas and users' costs functions can be used by transport modellers. However, explicitly accounting for delays' and vehicles' operational costs, it was important as they can be included as user-defined functions in current commercial software (e.g. PTV Visum).

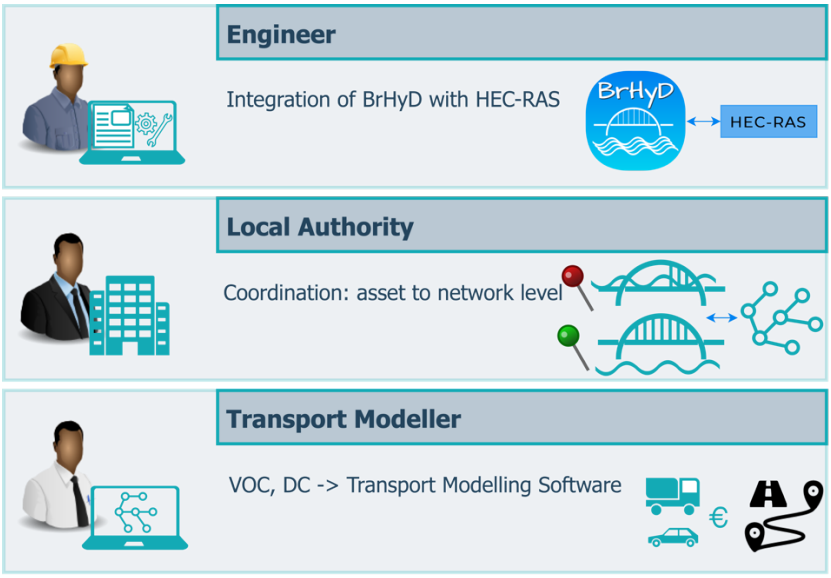


Figure 47. Impact of the research and involved actors

In conclusion, this work addressed critical challenges related to flood-induced bridge collapses and their implications for the road network. By providing practical tools and solutions, it has the potential to bring about positive changes in various sectors and among different stakeholders. Engineers can benefit from enhanced hydraulic design and assessment methods, local authorities can make more informed decisions at both asset and network levels, and transport modellers can incorporate more comprehensive cost functions into their models. The proposed approach emphasizes the importance of considering bridges within a broader framework and highlights the need for effective measures to prevent critical situations and ensure the safety and connectivity of communities in the face of flood events.

9.4. Future Research

The present Thesis covered the following knowledge areas:

i. The hazard simulation through hydrologic and hydraulic models;
ii. The driftwood accumulation at bridges;
iii. A simplified structural model of the bridge, through physical as well as statistical approaches;
iv. The traffic flow theory to gather data through a novel web-based approach;
v. A road network analysis to compute disruptions;
vi. The probability theory to account for uncertainties;
vii. Informatics by coding novel programs to manage the computational cost of the methodology.

The combination of these multidisciplinary areas will bring research themes closer to practice. However, the methodology can be further expanded by adding relevant features to meet research as well as practice needs.

Concerning the hazard modelling, the hydraulic model can be created by using DEMs from LiDAR surveys. To this end, the implementation of this feature is already available in HEC–RAS, although the remote control of the program through HECRASController has not been applied for the scope. The use of 2D analysis will also provide more accurate results of expected discharge magnitudes on inline structures (e.g. bridges) due to possible water overtopping embankments; this phenomenon is particularly relevant for hanging riverbeds.

The driftwood simulation can be refined by incorporating the recruitment phase, by budgeting the process from its origin at river's catchment. This will allow to reduce uncertainties on the logs' dimensions and density. In addition, a dedicated survey campaign can help to define exposure maps, highlighting dead wood, erosion and sliding mechanisms, as per Figure 48.



(A) (B)

Figure 48. Rupture faults at watersheds: (A) located on Steinbach creek, at Floh-Seligenthal, Thuringia (Germany) ; (B) located in a tributary creek of Eichenbach at Frohnhofen, RLP (Germany). Pictures taken by the author

Concerning the structural components, potential developments of this research could incorporate a sensitivity analysis, by integrating other bridge typologies. To this end, variations in hydrodynamic loads are also expected. In addition, the inclusion of bearings' constitutive laws will significantly improve the accuracy of the bridge behaviour facing high water stages. Laboratory tests on bearings can also shed lights on the reduced friction at the girder's interface due to water.

Another topic concerns the adaptation of the proposed approach to multi-span bridges in wide rivers. Indeed, the analysis would require considering variations in flow velocity along the bridge deck, in addition to the considered forces, as per Chapter 4.

Moving forward, there are several possibilities for further development and improvement of the proposed framework also at network level. Incorporating a capacity-reduction likelihood into the analysis would enhance the accuracy of the detour impact assessment. Additionally, expanding the application of the method to other datasets and scenarios would provide further insights into its effectiveness and applicability in different contexts. This analysis could also incorporate social impacts of road closures, by resorting to existing models and simulating land-use changes.

The proposed approach can be also extended by acting on the expansion of developed computer programs. Specifically, stakeholders and practitioners would benefit by the inclusion of a module that incorporates possible mitigation measures and results of laboratory tests to validate the analytic approach. In addition, the inclusion of real-time monitoring into the framework would greatly improve the prediction accuracy as well as the calibration of the analytic model.

References

AASTHO (2012) *Bridge design specifications*. Washington, DC: American Association of State Highway and Transportation Officials.

Ahamed, T., Duan, J.G. and Jo, H. (2021) 'Flood-fragility analysis of instream bridges – consideration of flow hydraulics, geotechnical uncertainties, and variable scour depth', *Structure and Infrastructure Engineering*, 17(11), pp. 1494–1507. Available at: https://doi.org/10.1080/15732479.2020.1815226.

Al-Hashimi, S.A.M., Al-Osmy, S.A.T. and Mulahasan, S. (2020) 'Water surface profile and flow pattern simulation over bridge deck slab', *Journal of Engineering Science and Technology*, 15(1), pp. 291–304. Available at: https://jestec.taylors.edu.my/Vol%2015%20issue%201%20February%202020/15_1_21.pdf

Alsobky, A. and Mousa, R. (2020) 'Estimating free flow speed using Google Maps API: accuracy, limitations, and applications.', *Advances in Transportation Studies*, 50, pp. 49–64.

Anderson, I. *et al.* (2017) 'Analysis of bridge and stream conditions of over 300 Vermont bridges damaged in Tropical Storm Irene', *Structure and Infrastructure Engineering*, 13(11), pp. 1437–1450. Available at: https://doi.org/10.1080/15732479.2017.1285329.

Anisha, A. *et al.* (2022) 'Fragility functions for highway RC bridge under various flood scenarios', *Engineering Structures*, 260, p. 114244. Available at: https://doi.org/10.1016/j.engstruct.2022.114244.

Apel, H., Vorogushyn, S. and Merz, B. (2022) 'Brief communication – Impact Forecasting Could Substantially Improve the Emergency Management of Deadly Floods: Case Study July 2021 floods in Germany', *NHESS*, 22, pp. 3005–3014. Available at: https://doi.org/10.5194/nhess-2022-33.

Argyroudis, S.A. *et al.* (2019) 'Fragility of transport assets exposed to multiple hazards: State-of-the-art review toward infrastructural resilience', *Reliability Engineering & System Safety*, 191, p. 106567. Available at: https://doi.org/10.1016/j.ress.2019.106567.

Argyroudis, S.A. *et al.* (2020) 'Resilience assessment framework for critical infrastructure in a multi-hazard environment: Case study on transport assets', *Science of The Total Environment*, 714, p. 136854. Available at: https://doi.org/10.1016/j.scitotenv.2020.136854.

Argyroudis, S.A. and Mitoulis, S.A. (2021) 'Vulnerability of bridges to individual and multiple hazards-floods and earthquakes', *Reliability Engineering & System Safety*, 210, p. 107564. Available at: https://doi.org/10.1016/j.ress.2021.107564.

Arneson, L.A. *et al.* (2012) *Evaluating Scour at Bridges, Fifth Edition*. FHWA-HIF-12-003. Springfield, VA: Federal Highway Administration, p. 340. Available at: https://rosap.ntl.bts.gov/view/dot/42053/dot_42053_DS1.pdf (Accessed: 1 September 2022).

Arrighi, C. *et al.* (2019) 'Preparedness against mobility disruption by floods', *Science of The Total Environment*, 654, pp. 1010–1022. Available at: https://doi.org/10.1016/j.scitotenv.2018.11.191.

Arrighi, C., Ballio, F. and Simonelli, T. (2023) 'A GIS-based flood damage index for cultural heritage', *International Journal of Disaster Risk Reduction*, 90, p. 103654. Available at: https://doi.org/10.1016/j.ijdrr.2023.103654.

ATC (2018) *Seismic Performance Assessment of Buildings, Volume 1 – Methodology, Second Edition*. Washington, D.C.: FEMA, p. 340.

Bagloee, S.A. *et al.* (2017) 'Identifying critical disruption scenarios and a global robustness index tailored to real life road networks', *Transportation Research Part E: Logistics and Transportation Review*, 98, pp. 60–81. Available at: https://doi.org/10.1016/j.tre.2016.12.003.

Baker, J.W. (2015) 'Efficient Analytical Fragility Function Fitting Using Dynamic Structural Analysis', *Earthquake Spectra*, 31(1), pp. 579–599. Available at: https://doi.org/10.1193/021113EQS025M.

Balomenos, G.P., Kameshwar, S. and Padgett, J.E. (2020) 'Parameterized fragility models for multi-bridge classes subjected to hurricane loads', *Engineering Structures*, 208, p. 110213. Available at: https://doi.org/10.1016/j.engstruct.2020.110213.

Banerjee, S. and Ganesh Prasad, G. (2013) 'Seismic risk assessment of reinforced concrete bridges in flood-prone regions', *Structure and Infrastructure Engineering*, 9(9), pp. 952–968. Available at: https://doi.org/10.1080/15732479.2011.649292.

Basile, R. *et al.* (2019) 'Advanced Computer Technologies for Fluid-Structure Interaction Modeling: a Review for Civil Engineering Applications', in *3rd International Conference on Recent Advances in Nonlinear Design, Resilience and Rehabilitation of Structures*. *CoRASS 2019*, Coimbra (ECCOMAS), pp. 64–73.

Bazzucchi, F., Restuccia, L. and Ferro, G.A. (2018) 'Considerations over the Italian road bridge infrastructure safety after the Polcevera viaduct collapse: past errors and future perspectives.', *Frattura e Integrita Strutturale*, 12(46), pp. 400–421. Available at: https://doi.org/10.3221/IGF-ESIS.46.37.

Benedict, S.T. and Knight, T.P. (2021) 'Benefits of Compiling and Analyzing Hydraulic-Design Data for Bridges', *Transportation Research Record*, 2675(11), pp. 1073–1081. Available at: https://doi.org/10.1177/03611981211023757.

BfG (2022) 'Waterbody-DE'. Bundesanstalt für Gewässerkunde (license: dl-de/by-2-0). Available at: https://geoportal.bafg.de/inspire/download/HY/servicefeed.xml (Accessed: 3 November 2022).

Bini, C. *et al.* (2012) *Cosa insegna il fiume.* Florence, IT: Regione Toscana, p. 201. Available at: www.toscana-notizie.it (Accessed: 10 November 2021).

Bizhanimanzar, M., Leconte, R. and Nuth, M. (2020) 'Catchment-Scale Integrated Surface Water-Groundwater Hydrologic Modelling Using Conceptual and Physically Based Models: A Model Comparison Study', *Water*, 12(2), p. 363. Available at: https://doi.org/10.3390/w12020363.

BKG (2022a) 'Digitales Geländemodell Gitterweite 5 m (DGM5)'. Bundesamt für Kartographie und Geodäsie (license: dl-de/by-2-0). Available at:

https://gdz.bkg.bund.de/index.php/default/digitales-gelandemodell-gitterweite-5-m-dgm5.html (Accessed: 15 August 2022).

BKG (2022b) 'NUTS250'. Bundesamt für Kartographie und Geodäsie (license: dl-de/by-2-0). Available at: https://daten.gdz.bkg.bund.de/produkte/vg/nuts250_1231/aktuell/nuts250_12-31.utm32s.shape.zip (Accessed: 3 November 2022).

Blöschl, G. *et al.* (2019) 'Changing climate both increases and decreases European river floods', *Nature*, 573(7772), pp. 108–111. Available at: https://doi.org/10.1038/s41586-019-1495-6.

Bonferroni, C. (1936) 'Teoria statistica delle classi e calcolo delle probabilità', *Pubblicazioni del R Istituto Superiore di Scienze Economiche e Commericiali di Firenze*, 8, pp. 3–62.

Brown, M.B. and Forsythe, A.B. (1974) 'Robust Tests for the Equality of Variances', *Journal of the American Statistical Association*, 69(346), pp. 364–367. Available at: https://doi.org/10.1080/01621459.1974.10482955.

Bruijn, J.A. de *et al.* (2022) 'Using rapid damage observations for Bayesian updating of hurricane vulnerability functions: A case study of Hurricane Dorian using social media', *International Journal of Disaster Risk Reduction*, 72, p. 102839. Available at: https://doi.org/10.1016/j.ijdrr.2022.102839.

Brunner, G.W. (2016) *HEC-RAS, River Analysis System Hydraulic Reference Manual*. CPD-69. Davis, CA: USACE, p. 547. Available at: https://www.hec.usace.army.mil/software/hec-ras/documentation/HEC-RAS%205.0%20Reference%20Manual.pdf (Accessed: 2 May 2022).

Capacci, L., Biondini, F. and Titi, A. (2020) 'Lifetime seismic resilience of aging bridges and road networks', *Structure and Infrastructure Engineering*, 16(2), pp. 266–286. Available at: https://doi.org/10.1080/15732479.2019.1653937.

Castelli, F. *et al.* (2014) *Implementazione modello distribuito per la Toscana MOBIDIC*. B2. Florence, IT, p. 29. Available at: https://www.regione.toscana.it/documents/10180/12745809/B2_Finale.pdf/f5a1b35e-bba1-45ef-9843-9a3b268aabd6 (Accessed: 2 May 2022).

Castelli, F. (2018) *Ricalibrazione modello idrologico MOBIDIC*. Florence, IT: University of Florence, p. 25. Available at:

https://www.regione.toscana.it/bancadati/atti/Contenuto.xml?id=5190314&nomeFile=Delibera_n.902_del_06-08-2018-Allegato-D (Accessed: 2 May 2022).

CEN (2005a) *EN 1991-1-6:2005*. Brussels: Euopean Committee for Standardization, p. 31. Available at: https://eurocodes.jrc.ec.europa.eu/.

CEN (2005b) *EN 1997:2005*. Brussels: Euopean Committee for Standardization, p. 200. Available at: https://eurocodes.jrc.ec.europa.eu/.

Chen, W.-B. and Liu, W.-C. (2017) 'Modeling the Influence of River Cross-Section Data on a River Stage Using a Two-Dimensional/Three-Dimensional Hydrodynamic Model', *Water*, 9(3). Available at: https://doi.org/10.3390/w9030203.

Chen, X.-Z. *et al.* (2015) 'Analysis of Transportation Network Vulnerability under Flooding Disasters', *Transportation Research Record*, 2532(1), pp. 37–44. Available at: https://doi.org/10.3141/2532-05.

Cheng, L. and Ming-Jer, K. (2014) 'Flow Types Around And Vortex Structure Beneath Inundated Bridge Deck', *Journal of Engineering, National Chung Hsing University*, 25(3), pp. 65–84. Available at: https://doi.org/10.6287/JENCHU.2014.2503.01.

Choudhury, J.R. and Hasnat, A. (2015) 'Bridge collapses around the world: Causes and mechanisms', in. *IABSE-JSCE Joint Conference on Advances in Bridge Engineering-III*, Dhaka, Bangladesh: Amin, Okui, Bhuiyan, Ueda, pp. 26–34. Available at: http://www.iabse-bd.org/session/k2.pdf (Accessed: 10 February 2023).

Chu, C.-R. *et al.* (2016) 'Numerical Analysis of Free Surface Flow over a Submerged Rectangular Bridge Deck', *Journal of Hydraulic Engineering*, 142(12), p. 04016060. Available at: https://doi.org/10.1061/(ASCE)HY.1943-7900.0001177.

Ciullo, A. *et al.* (2017) 'Socio-hydrological modelling of flood-risk dynamics: comparing the resilience of green and technological systems', *Hydrological Sciences Journal*, 62(6), pp. 880–891. Available at: https://doi.org/10.1080/02626667.2016.1273527.

Committee BD-090 (2017) *AS 5100.2:2017*. Bridge Design Design Loads. Sydney: Standards Australia, p. 137. Available at: www.standards.org.au.

Cook, W. and Barr, P.J. (2017) 'Observations and Trends among Collapsed Bridges in New York State', *Journal of Performance of Constructed Facilities*, 31(4), p. 04017011. Available at: https://doi.org/10.1061/(ASCE)CF.1943-5509.0000996.

D'Angelo, M. *et al.* (2022) 'Hydraulic Safety Evaluation and Dynamic Investigations of Baghetto Bridge in Italy', *Infrastructures*, 7(4), p. 53. Available at: https://doi.org/10.3390/infrastructures7040053.

De Cicco, P.N. *et al.* (2018) 'In-channel wood-related hazards at bridges: A review', *River Research and Applications*, 34(7), pp. 617–628. Available at: https://doi.org/10.1002/rra.3300.

De Cicco, P.N. *et al.* (2020) 'Bridge pier shape influence on wood accumulation: Outcomes from flume experiments and numerical modelling', *Journal of Flood Risk Management*, 13(2). Available at: https://doi.org/10.1111/jfr3.12599.

Dean, M.T. (2020) *Laboratory Study of Hydrodynamics of Submerged Bridges*. MSc Thesis. University of Texas at Arlington.

Dekelbab, W., Al-Wazeer, A. and Harris, B. (2008) 'History Lessons From the National Bridge Inventory', *FHWA-HRT-08-004*. Available at: https://highways.dot.gov/public-roads/mayjun-2008/history-lessons-national-bridge-inventory.

Dolce, M., Bramerini, F. and Castenetto, S. (2016) *Condizione limite per l'emergenza*. Rome: Commissione Tecnica per la Microzonazione Sismica, p. 281. Available at: https://www.webms.it/sites/default/files/2018-06/CLEWeb_2_Edizione.pdf (Accessed: 10 January 2020).

Dong, Y. and Frangopol, D.M. (2016) 'Probabilistic Time-Dependent Multihazard Life-Cycle Assessment and Resilience of Bridges Considering Climate Change', *Journal of Performance of Constructed Facilities*, 30(5), p. 04016034. Available at: https://doi.org/10.1061/(ASCE)CF.1943-5509.0000883.

Douben, K.-J. (2006) 'Characteristics of river floods and flooding: a global overview, 1985–2003', *Irrigation and Drainage*, 55(S1), pp. S9–S21. Available at: https://doi.org/10.1002/ird.239.

Dráb, A. *et al.* (2019) 'Determination of the Hydrodynamic Load on an Inundated Bridge Deck by Measurements Performed on a Physical Model', *International Journal of Civil Engineering*, 17(10), pp. 1491–1502. Available at: https://doi.org/doi.org/10.1007/s40999-019-00411-8.

Duan, Y. *et al.* (2022) 'Assessment and spatiotemporal analysis of global flood vulnerability in 2005–2020', *International Journal of Disaster Risk Reduction*, 80, p. 103201. Available at: https://doi.org/10.1016/j.ijdrr.2022.103201.

Dysarz, T. (2018) 'Application of Python Scripting Techniques for Control and Automation of HEC-RAS Simulations', *Water*, 10, p. 1382. Available at: https://doi.org/10.3390/w10101382.

EC, EEA (2022) *Economic losses from climate-related extremes in Europe*. European Commission and European Environment Agency. Available at: https://www.eea.europa.eu/ims/economic-losses-from-climate-related (Accessed: 10 February 2023).

Elmer, F. *et al.* (2010) 'A Delphi Method Expert Survey to Derive Standards for Flood Damage Data Collection', *Risk Analysis*, 30(1), pp. 107–124. Available at: https://doi.org/10.1111/j.1539-6924.2009.01325.x.

Ercolani, G. and Castelli, F. (2017) 'Variational assimilation of streamflow data in distributed flood forecasting', *Water Resources Research*, 53(1), pp. 158–183. Available at: https://doi.org/10.1002/2016WR019208.

European Court of Auditors (2018) *Floods Directive: progress in assessing risks, while planning and implementation need to improve*. Special Report 25. Brussels: European Union, p. 63. Available at: https://www.eca.europa.eu/en/publications?did=47211 (Accessed: 14 July 2020).

Falconer, R. *et al.* (2010) 'Strenghtening of masonry bridges against traffic and flooding.', in. *Structural Faults and Repair Conference 2010 13th International Congress and Exhibition*, Edinburgh, UK. pp. 1–10.

Gehl, P. and D'Ayala, D. (2018) 'System loss assessment of bridge networks accounting for multi-hazard interactions', 14(10), pp. 1355–1371. Available at: https://doi.org/10.1080/15732479.2018.1434671.

George, J. and Menon, A. (2021) 'A mechanism-based assessment framework for masonry arch bridges under scour-induced support rotation', *Advances in Structural Engineering*, 24(12), pp. 2637–2651. Available at: https://doi.org/10.1177/13694332211009325.

Gervásio, H. and da Silva, L.S. (2013) 'Life-cycle social analysis of motorway bridges', *Structure and Infrastructure Engineering*, 9(10), pp. 1019–1039. Available at: https://doi.org/10.1080/15732479.2011.654124.

Ghosn M. *et al.* (2016) 'Performance Indicators for Structural Systems and Infrastructure Networks', *Journal of Structural Engineering*, 142(9), p. F4016003. Available at: https://doi.org/10.1061/(ASCE)ST.1943-541X.0001542.

Giresini, L., Puppio, M.L. and Sassu, M. (2016) 'Collapse of corrugated metal culvert in Northern Sardinia: analysis and numerical simulations', *International Journal of Forensic Engineering*, 3(1–2), pp. 69–85. Available at: https://doi.org/10.1504/IJFE.2016.075991.

Gleason, C.J. and Durand, M.T. (2020) 'Remote Sensing of River Discharge: A Review and a Framing for the Discipline', *Remote Sensing*, 12(7). Available at: https://doi.org/10.3390/rs12071107.

Goodell, C.R. (2014) *Breaking the HEC-RAS Code: A User's Guide to Automating HEC-RAS* (1 vol). 1st edn. Portland, OR: h2ls.

Google LLC (2020) 'Google Maps Platform FAQs'. Available at: https://developers.google.com/maps/faq?hl=en (Accessed: 10 November 2020).

Govindasamy, A.V. *et al.* (2012) 'Observational Method for Estimating Future Scour Depth at Existing Bridges', in *Scour and Erosion*. American Society of Civil Engineers, pp. 41–65. Available at: https://doi.org/10.1061/41147(392)4.

Grates, H. (2023) 'Domhof-Brücke Schuld'. Available at: https://www.aw-wiki.de/w/images/1/16/Schuld_-_Heinz_Grates_%28337%29.jpg (Accessed: 20 February 2023).

Green, D. *et al.* (2017) 'City-scale accessibility of emergency responders operating \hack\newline during flood events', *Natural Hazards and Earth System Sciences*, 17(1), pp. 1–16. Available at: https://doi.org/10.5194/nhess-17-1-2017.

Gschnitzer, T. *et al.* (2017) 'Towards a robust assessment of bridge clogging processes in flood risk management', *Geomorphology*, 279, pp. 128–140. Available at: https://doi.org/10.1016/j.geomorph.2016.11.002.

Guimarães, L.F. *et al.* (2021) 'The challenges of urban river restoration and the proposition of a framework towards river restoration goals', *Journal of Cleaner Production*, 316, p. 128330. Available at: https://doi.org/10.1016/j.jclepro.2021.128330.

Guo, X., Badroddin, M. and Chen, Z. (2019) 'Scour-dependent empirical fragility modelling of bridge structures under earthquakes', *Advances in Structural Engineering*, 22(6), pp. 1384–1398. Available at: https://doi.org/10.1177/1369433218815433.

Gusev, M. (2015) 'GNM plugin for QGIS'. Available at: https://github.com/nextgis/gnm_qgis (Accessed: 11 November 2020).

Haardt, P. (1999) 'Algorithmen zur Zustandsbewertung von Ingenieurbauwerken', *Bundesanstalt für Straßenwesen*, Bergisch Gladbach, Germany. p. 41.

Hamill, L. (1998) *Bridge hydraulics*. First Edition. Abingdon: CRC Press.

Han, X. and Frangopol, D.M. (2022) 'Life-cycle connectivity-based maintenance strategy for bridge networks subjected to corrosion considering correlation of bridge resistances', *Structure and Infrastructure Engineering*, pp. 1–24. Available at: https://doi.org/10.1080/15732479.2021.2023590.

Herschy, R.W. (2019) *Streamflow Measurement*. 3rd edn. New York, USA: Taylor & Francis.

Hodgkins, G.A. *et al.* (2017) 'Climate-driven variability in the occurrence of major floods across North America and Europe', *Journal of Hydrology*, 552, pp. 704–717. Available at: https://doi.org/10.1016/j.jhydrol.2017.07.027.

Holnbeck, S.R. and Parrett, C. (1997) *Method for rapid estimation of scour at highway bridges based on limited site data*. US Department of the Interior, US Geological Survey (4310). Available at: https://pubs.usgs.gov/wri/1996/4310/report.pdf (Accessed: 14 July 2023).

Huffman, G.J. *et al.* (2019) 'GPM IMERG Final Precipitation L3 1 day 0.1 degree x 0.1 degree V06'. Andrey Savtchenko, Greenbelt, MD, Goddard Earth Sciences Data and Information Services Center (GES DISC), NASA: Washington DC, USA.

Inkoom, S. and Sobanjo, J.O. (2019) 'Reliability Importance as a Measure of Bridge Element Condition Index for Deteriorating Bridges', *Transportation Research Record*, 2673(12), pp. 327–338. Available at: https://doi.org/10.1177/0361198119862627.

Jacobs, M. and Ryan, C. (2021) 'Application of HEC-HMS in Australia including injection of ARR2019 Temporal Patterns, establishment of calibrated parameters and comparison with other Australian hydrological models', in *HWRS 2021: Digital Water: Hydrology and Water Resources Symposium 2021*. Engineers Australia, pp. 275–286.

Jedlička, K. *et al.* (2016) 'Open Transport Map—Routable OpenStreetMap', in *2016 IST-Africa Week Conference*. Durban, South Africa: IEEE, pp. 1–11. Available at: https://doi.org/10.1109/ISTAFRICA.2016.7530657.

Jempson, M. (2000) *Flood and debris loads on bridges*. PhD Thesis. University of Queensland.

Jiang, Y. *et al.* (2021) 'Probabilistic assessment of transport network vulnerability with equilibrium flows', *International Journal of Sustainable Transportation*, 15(7), pp. 512–523. Available at: https://doi.org/10.1080/15568318.2020.1770904.

Kalendher, F. *et al.* (2018) 'Fragility Curves for concrete girder bridges under flood hazard.', in N. Powers et al. (eds) *Maintenance, Safety, Risk, Management and Life-Cycle Performance of Bridges*. CRC Press, pp. 2393–2399. Available at: https://doi.org/10.1201/9781315189390-324.

Kellagher, R. (2013) *Rainfall runoff management for developments*. SC030219. Bristol: Environment Agency, p. 146. Available at: http://www.environment-agency.gov.uk/ (Accessed: 14 July 2023).

Kerenyi, K., Sofu, T. and Guo, J. (2009) *Hydrodynamic forces on inundated bridge decks*. FHWA-HRT-09-028. McLean, VA: U.S. DOT, pp. 1–48.

Kermanshah, A. and Derrible, S. (2017) 'Robustness of road systems to extreme flooding: using elements of GIS, travel demand, and network science', *Natural Hazards*, 86(1), pp. 151–164. Available at: https://doi.org/10.1007/s11069-016-2678-1.

Khan, S.M. *et al.* (2018) 'Development of Statewide Annual Average Daily Traffic Estimation Model from Short-Term Counts: A Comparative Study for South Carolina', *Transportation Research Record*, 2672(43), pp. 55–64. Available at: https://doi.org/10.1177/0361198118798979.

Khandel, O. and Soliman, M. (2021) 'Integrated Framework for Assessment of Time-Variant Flood Fragility of Bridges Using Deep Learning Neural Networks', *Journal of Infrastructure Systems*, 27(1), p. 04020045. Available at: https://doi.org/10.1061/(ASCE)IS.1943-555X.0000587.

Kim, H. *et al.* (2017) 'Flood fragility analysis for bridges with multiple failure modes', *Advances in Mechanical Engineering*, 9(3), p. 168781401769641. Available at: https://doi.org/10.1177/1687814017696415.

Kimura, I., Kang, T. and Kato, K. (2021) '3D–3D Computations on Submerged-Driftwood Motions in Water Flows with Large Wood Density around Driftwood Capture Facility', *Water*, 13(10). Available at: https://doi.org/10.3390/w13101406.

Kirby, A. *et al.* (2015) *Manual on scour at bridges and other hydraulic structures*. CIRIA.

Kjeldsen, T.R., Jones, D.A. and Morris, D.G. (2014) 'Using multiple donor sites for enhanced flood estimation in ungauged catchments', *Water Resources Research*, 50(8), pp. 6646–6657. Available at: https://doi.org/10.1002/2013WR015203.

Kreienkamp, F. *et al.* (2021) *Rapid attribution of heavy rainfall events leading to the severe flooding in Western Europe during July 2021*. World Weather Attribution: Oxford, UK, p. 54. Available at: https://www.worldweatherattribution.org/wp-content/uploads/Scientific-report-Western-Europe-floods-2021-attribution.pdf (Accessed: 13 February 2023).

Lam, J.C. *et al.* (2018) 'Stress tests for a road network using fragility functions and functional capacity loss functions', *Reliability Engineering & System Safety*, 173, pp. 78–93. Available at: https://doi.org/10.1016/j.ress.2018.01.015.

Lamb, R. *et al.* (2019) 'A Probabilistic Model of the Economic Risk to Britain's Railway Network from Bridge Scour During Floods', *Risk Analysis*, 39(11), pp. 2457–2478. Available at: https://doi.org/10.1111/risa.13370.

Landesamt für Umwelt Rheinland-Pfalz (2022) *Hochwassermeldedienst*. LfU. Available at: https://www.hochwasser-rlp.de.

Leal, M. *et al.* (2019) 'How much does an extreme rainfall event cost? Material damage and relationships between insurance, rainfall, land cover and urban flooding', *Hydrological Sciences Journal*, 64(6), pp. 673–689. Available at: https://doi.org/10.1080/02626667.2019.1595625.

Lebbe, M.F.K. *et al.* (2014) 'Failure mechanisms of bridge infrastructure in an extreme flood event', in *Proceedings of the 1st International Conference on Infrastructure Failures and Consequences (ICFC 2014)*. Melbourne: RMIT Publishing, pp. 124–132.

Li, S.-Q. and Chen, Y.-S. (2023) 'Vulnerability and economic loss evaluation model of a typical group structure considering empirical field inspection data', *International Journal of Disaster Risk Reduction*, 88, p. 103617. Available at: https://doi.org/10.1016/j.ijdrr.2023.103617.

Li, Y. *et al.* (2020) 'Long-term resilience and loss assessment of highway bridges under multiple natural hazards', *Structure and Infrastructure Engineering*, 16(4), pp. 626–641. Available at: https://doi.org/10.1080/15732479.2019.1699936.

Lilliefors, H.W. (1967) 'On the Kolmogorov-Smirnov Test for Normality with Mean and Variance Unknown', 62(318), pp. 399–402.

Lin, C. *et al.* (2012) 'On the Flow Structures Under a Partially Inundated Bridge Deck', *Journal of Mechanics*, 28(1), pp. 191–207. Available at: https://doi.org/10.1017/jmech.2012.20.

Loli, M. *et al.* (2022) 'Flood characterization based on forensic analysis of bridge collapse using UAV reconnaissance and CFD simulations', *Science of The Total Environment*, 822, p. 153661. Available at: https://doi.org/10.1016/j.scitotenv.2022.153661.

Ludwig, P. *et al.* (2022) 'A multi-disciplinary analysis of the exceptional flood event of July 2021 in central Europe. Part 2: Historical context and relation to climate change', *Natural Hazards and Earth System Sciences Discussions*, 23, pp. 1287-1311. Available at: https://doi.org/10.5194/nhess-2022-225.

LVermGeo (2022) 'Digitales Geländemodell Gitterweite 1 m (DGM1)'. Landesamt für Vermessung und Geobasisinformation Rheinland-Pfalz. Available at: https://lvermgeo.rlp.de/fileadmin/lvermgeo/pdf/produktblaetter/ProduktbeschreibungRP_DGM.pdf (Accessed: 15 August 2022).

Mackie, K.R. and Stojadinović, B. (2006) 'Post-earthquake functionality of highway overpass bridges', *Earthquake Engineering & Structural Dynamics*, 35(1), pp. 77–93. Available at: https://doi.org/10.1002/eqe.534.

Maiwald, H. *et al.* (2022) 'Das Hochwasser 2021: Ingenieuranalyse der Bauwerksschäden', *Bautechnik*, 99(12), pp. 878–890. Available at: https://doi.org/10.1002/bate.202200062.

Majtan, E., Cunningham, L.S. and Rogers, B.D. (2022) 'Experimental and Numerical Investigation of Floating Large Woody Debris Impact on a Masonry Arch Bridge', *Journal of Marine Science and Engineering*, 10(7), p. 911. Available at: https://doi.org/10.3390/jmse10070911.

Majtan, E., Cunningham, L.S. and Rogers, B.D. (2023) 'Numerical study on the structural response of a masonry arch bridge subject to flood flow and debris impact', *Structures*, 48, pp. 782–797. Available at: https://doi.org/10.1016/j.istruc.2022.12.100.

Malavasi, S. and Guadagnini, A. (2003) 'Hydrodynamic loading on river bridges', *Journal of Hydraulic Engineering*, 129(11), pp. 854–861. Available at: https://doi.org/10.1061/(ASCE)0733-9429(2003)129:11(854).

Malavasi, S. and Guadagnini, A. (2005) 'Closure to "hydrodynamic loading on river bridges" by Stefano Malavasi and Alberto Guadagnini', *Journal of Hydraulic Engineering*, 131(7), pp. 854–861. Available at: https://doi.org/10.1061/(ASCE)0733-9429(2005)131:7(622).

Malavasi, S. and Guadagnini, A. (2007) 'Interactions between a rectangular cylinder and a free-surface flow', *Journal of Fluids and Structures*, 23(8), pp. 1137–1148. Available at: https://doi.org/10.1016/j.jfluidstructs.2007.04.002.

Mattsson, L.-G. and Jenelius, E. (2015) 'Vulnerability and resilience of transport systems – A discussion of recent research', *Resilience of Networks*, 81, pp. 16–34. Available at: https://doi.org/10.1016/j.tra.2015.06.002.

Mazzorana, B. *et al.* (2018) 'Assessing and mitigating large wood-related hazards in mountain streams: recent approaches.', *Journal of Flood Risk Management*, 11(2), pp. 207–222. Available at: https://doi.org/10.1111/jfr3.12316.

Merz, B. *et al.* (2010) 'Review article "Assessment of economic flood damage"', *Natural Hazards and Earth System Sciences*, 10(8), pp. 1697–1724. Available at: https://doi.org/10.5194/nhess-10-1697-2010.

Merz, B. *et al.* (2021) 'Causes, impacts and patterns of disastrous river floods', *Nature Reviews Earth & Environment*, 2(9), pp. 592–609. Available at: https://doi.org/10.1038/s43017-021-00195-3.

Merz, B. *et al.* (2022) 'Disastrous flooding in July 2021 in Germany – Event analysis and consequences for risk assessment approaches', in. *IAHS-AISH Scientific Assembly 2022*, Montpellier, France, pp. IAHS2022-183. Available at: https://doi.org/10.5194/iahs2022-183.

Merz, Bruno *et al.* (2022) 'Understanding Heavy Tails of Flood Peak Distributions', *Water Resources Research*, 58(6), p. e2021WR030506. Available at: https://doi.org/10.1029/2021WR030506.

Miao, Q. (2019) 'Are We Adapting to Floods? Evidence from Global Flooding Fatalities', *Risk Analysis*, 39(6), pp. 1298–1313. Available at: https://doi.org/10.1111/risa.13245.

Ministero Infrastrutture e Trasporti (2018) *L. 16 novembre 2018, n. 130*. Available at: https://www.gazzettaufficiale.it/eli/id/2018/11/19/18G00157/sg (Accessed: 15 February 2020).

Mohr, S. *et al.* (2022) 'A multi-disciplinary analysis of the exceptional flood event of July 2021 in central Europe. Part 1: Event description and analysis', *Hydrological Hazards*, 23, pp. 525-551. Available at: https://doi.org/10.5194/nhess-2022-137.

Mondoro, A. and Frangopol, D.M. (2018) 'Risk-based cost-benefit analysis for the retrofit of bridges exposed to extreme hydrologic events considering multiple failure modes', *Engineering Structures*, 159, pp. 310–319. Available at: https://doi.org/10.1016/j.engstruct.2017.12.029.

Montalvo, C., Cook, W. and Keeney, T. (2020) 'Retrospective Analysis of Hydraulic Bridge Collapse', *Journal of Performance of Constructed Facilities*, 34(1), p. 04019111. Available at: https://doi.org/10.1061/(ASCE)CF.1943-5509.0001378.

N. Petrovska and A. Stevanovic (2015) 'Traffic Congestion Analysis Visualisation Tool', in *2015 IEEE 18th International Conference on Intelligent Transportation Systems*. *2015 IEEE 18th International Conference on Intelligent Transportation Systems*, pp. 1489–1494. Available at: https://doi.org/10.1109/ITSC.2015.243.

Nagurney, A. and Qiang, Q. (2007) 'A network efficiency measure for congested networks', *Europhysics Letters*, 79(3), p. 38005. Available at: https://doi.org/10.1209/0295-5075/79/38005.

Naumann, J. and Holst, R. (2005) 'Bauwerkspruefung nach DIN 1076-Eine verantwortungsvolle Aufgabe fuer die Sicherheit/Bridge Inspection according to DIN 1076-A responsible Task for Safety', *Straße und Autobahn*, 56(6), pp. 319–26.

Oudenbroek, K. *et al.* (2018) 'Hydrodynamic and debris-damming failure of bridge decks and piers in steady flow', *Geosciences (Switzerland)*, 8(11). Available at: https://doi.org/10.3390/geosciences8110409.

Padgett, J.E., Spiller, A. and Arnold, C. (2012) 'Statistical analysis of coastal bridge vulnerability based on empirical evidence from Hurricane Katrina', *Structure and Infrastructure Engineering*, 8(6), pp. 595–605. Available at: https://doi.org/10.1080/15732470902855343.

Palin, E.J. *et al.* (2021) 'Implications of climate change for railway infrastructure', *WIREs Climate Change*, 12(5), p. e728. Available at: https://doi.org/10.1002/wcc.728.

Pang, Y. *et al.* (2014) 'Seismic fragility analysis of multi-span deep water bridges', in *Bridge Maintenance, Safety, Management and Life Extension*. CRC Press, pp. 800–806. Available at: https://doi.org/10.1201/b17063-116.

Panici, D. and de Almeida, G.A.M. (2018) 'Formation, Growth, and Failure of Debris Jams at Bridge Piers', *Water Resources Research*, 54(9), pp. 6226–6241. Available at: https://doi.org/10.1029/2017WR022177.

Panici, D. and Kripakaran, P. (2023) 'Assessing and mitigating risks to bridges from large wood using satellite imagery', *Proceedings of the Institution of Civil Engineers - Bridge Engineering*, 176(2), pp. 118–128. Available at: https://doi.org/10.1680/jbren.21.00059.

Parola, A.C., Apelt, C.J. and Jempson, M. (2000) *Debris Forces on Highway Bridges*. NCHRP 445. Washington, D.C.: Transportation Research Board, p. 90. Available at: https://onlinepubs.trb.org/onlinepubs/nchrp/nchrp_rpt_445.pdf (Accessed: 2 May 2022).

Pearson, D.R., Jones, J.S. and Stein, S.M. (2000) 'Risk-Based Design of Bridge Scour Countermeasures', *Transportation Research Record*, 1696(1), pp. 229–235. Available at: https://doi.org/10.3141/1696-68.

Pella, H. and Ose, K. (2018) 'Network Analysis and Routing with QGIS', in *QGIS and Applications in Water and Risks*, pp. 105–144. Available at: https://doi.org/10.1002/9781119476726.ch4.

Petrangeli, M.P. (1996) *Progettazione e Costruzione di Ponti*. IV. Milan, IT: CEA.

Picek, T. *et al.* (2007) 'Hydraulic calculation of bridges at high water stages', *Journal of Hydraulic Research*, 45(3), pp. 400–406. Available at: https://doi.org/10.1080/00221686.2007.9521773.

Porta, S., Crucitti, P. and Latora, V. (2006) 'The Network Analysis of Urban Streets: A Primal Approach', *Environment and Planning B: Planning and Design*, 33(5), pp. 705–725. Available at: https://doi.org/10.1068/b32045.

Proske, D. (2018) *Bridge collapse frequencies versus failure probabilities*. Cham: Springer (Risk Engineering).

Pucci, A. *et al.* (2019) 'Method for sustainable large-scale bridges survey', in *Towards a Resilient Built Environment Risk and Asset Management - Report*. *IABSE Symposium, Guimaraes 2019*, Guimarães, Portugal: International Association for Bridge and Structural Engineering (IABSE), pp. 1034–1041.

Pucci, A., Sousa, H.S.; Giresini, L.; Matos, J.C.; Castelli, F. (2023a) 'Fragility of Bridge Decks exposed to Hydraulic and Driftwood Actions', *Structure and Infrastructure Engineering, (Accepted for publication)* [Preprint].

Pucci, A. et al. (2023b) 'Fragility Analysis Based on Damaged Bridges during the 2021 Flood in Germany', Applied Sciences, 13(18), p. 10454. doi:10.3390/app131810454.

Pulugurtha, S., Penmetsa, P. and Duddu, V. (2019) 'Travel time, reliability, additional trip time, willingness to pay and their values by socio-economic factors.', *Advances in Transportation Studies*, 49, pp. 31–46.

Puppio, M.L. (2018) *Safety Assessment and Strenghtening of Short Span Bridges in Case of Extreme Rainstorms*. PhD Thesis. University of Pisa. Available at: https://etd.adm.unipi.it/t/etd-05022018-145153/ (Accessed: 10 November 2021).

Puppio, M.L., Novelli, S. and Sassu, M. (2018) 'Failure evidences of reduced span bridges in case of extreme rainfalls The case of Livorno', *Frattura ed Integrità Strutturale*, 12(46), pp. 190–202. Available at: https://doi.org/10.3221/IGF-ESIS.46.18.

Qi, L. *et al.* (2022) 'On the capacity of Sentinel-1 synthetic aperture radar in detecting floating macroalgae and other floating matters', *Remote Sensing of Environment*, 280, p. 113188. Available at: https://doi.org/10.1016/j.rse.2022.113188.

Quiniou, M. *et al.* (2022) 'Large Wood Transport-Related Flood Risks Analysis of Lourdes City Using Iber-Wood Model', in P. Gourbesville and G. Caignaert (eds) *Advances in Hydroinformatics*. Singapore: Springer Nature Singapore, pp. 481–498.

Rania, N. *et al.* (2019) 'The Collapse of the Morandi Bridge in Genoa on 14 August 2018: A Collective Traumatic Event and Its Emotional Impact Linked to the Place and Loss of a Symbol', *Sustainability*, 11(23). Available at: https://doi.org/10.3390/su11236822.

Rasband, WS. (2009) 'Imagej', US National Institutes of Health, Bethesda, Maryland, USA, Available at: *http://rsb. info. nih. gov/ij/*.

Ries III, K.G. *et al.* (2007) 'The national streamflow statistics program: A computer program for estimating streamflow statistics for ungaged sites'. Reston: USGS. Available at: http://water.usgs.gov/software/ (Accessed: 26 May 2020).

Robertson, I.N. *et al.* (2007) 'Lessons from Hurricane Katrina Storm Surge on Bridges and Buildings', *Journal of Waterway, Port, Coastal, and Ocean Engineering*, 133(6), pp. 463–483. Available at: https://doi.org/10.1061/(ASCE)0733-950X(2007)133:6(463).

Roggenkamp, T. and Herget, J. (2014) 'Reconstructing peak discharges of historic floods of the river Ahr, Germany', 68(1), pp. 49–59. Available at: https://doi.org/10.3112/erdkunde.2014.01.05.

Roggenkamp, T. and Herget, J. (2022) 'Hochwasser der Ahr im Juli 2021–Abflussabschätzung und Einordnung', 66, pp. 40–49.

Ross, S.M. (2003) 'Peirce's criterion for the elimination of suspect experimental data', 20(2), pp. 38–41.

Ruiz-Villanueva, V. *et al.* (2013) 'Reconstruction of a flash flood with large wood transport and its influence on hazard patterns in an ungauged mountain basin: woody debris in flood hazard analysis',

Hydrological Processes, 27(24), pp. 3424–3437. Available at: https://doi.org/10.1002/hyp.9433.

Ruiz-Villanueva, V. *et al.* (2014) 'Two-dimensional numerical modeling of wood transport', *Journal of Hydroinformatics*, 16(5), pp. 1077–1096. Available at: https://doi.org/10.2166/hydro.2014.026.

Ruiz-Villanueva, V. *et al.* (2016) 'Wood density and moisture sorption and its influence on large wood mobility in rivers', *CATENA*, 140, pp. 182–194. Available at: https://doi.org/10.1016/j.catena.2016.02.001.

Ruiz-Villanueva, V. *et al.* (2017) 'Large wood clogging during floods in a gravel-bed river: the Długopole bridge in the Czarny Dunajec River, Poland: Large wood clogging during floods', *Earth Surface Processes and Landforms*, 42(3), pp. 516–530. Available at: https://doi.org/10.1002/esp.4091.

Rupi, F. *et al.* (2015) 'The Evaluation of Road Network Vulnerability in Mountainous Areas: A Case Study', *Networks and Spatial Economics*, 15(2), pp. 397–411. Available at: https://doi.org/10.1007/s11067-014-9260-8.

Sarvepalli, A. and Davis, B. (2020) 'Multiple Uses of Big Data for Model Validation and Express Lanes Traffic Forecasts', *Transportation Research Record*, 2674(11), pp. 87–100. Available at: https://doi.org/10.1177/0361198120942222.

Sassu, M., Giresini, L. and Puppio, M.L. (2017) 'Failure scenarios of small bridges in case of extreme rainstorms', *Sustainable and Resilient Infrastructure*, 2(3), pp. 108–116. Available at: https://doi.org/10.1080/23789689.2017.1301696.

Schalko, I. *et al.* (2017) 'Schwemmholz: Gefahrenbeurteilung und Massnahmenplanung am Fallbeispiel Renggbach, Kanton Luzern', *Wasser Energie Luft*, 109(4), pp. 271–278.

Schalko, I. *et al.* (2018) 'Backwater Rise due to Large Wood Accumulations', *Journal of Hydraulic Engineering*, 144(9), p. 04018056. Available at: https://doi.org/10.1061/(ASCE)HY.1943-7900.0001501.

Schalko, I. *et al.* (2019) 'Laboratory Flume Experiments on the Formation of Spanwise Large Wood Accumulations: I. Effect on Backwater Rise', *Water Resources Research*, 55(6), pp. 4854–4870. Available at: https://doi.org/10.1029/2018WR024649.

Schalko, I. *et al.* (2020) 'Risk reduction measures of large wood accumulations at bridges', *Environmental Fluid Mechanics*, 20(3), pp. 485–502. Available at: https://doi.org/10.1007/s10652-019-09719-4.

Schalko, I. and Weitbrecht, V. (2022) 'Impact of Large Wood on River Ecosystems', *Water*, 14(5). Available at: https://doi.org/10.3390/w14050784.

Schmocker, L. and Hager, W.H. (2011) 'Probability of Drift Blockage at Bridge Decks', *Journal of Hydraulic Engineering*, 137(4), pp. 470–479. Available at: https://doi.org/10.1061/(ASCE)HY.1943-7900.0000319.

Schmocker, L. and Weitbrecht, V. (2013) 'Driftwood: Risk Analysis and Engineering Measures', *Journal of Hydraulic Engineering*, 139(7), pp. 683–695. Available at: https://doi.org/10.1061/(ASCE)HY.1943-7900.0000728.

Schneck, A. and Nökel, K. (2020) 'Accelerating Traffic Assignment with Customizable Contraction Hierarchies', *Transportation Research Record*, 2674(1), pp. 188–196. Available at: https://doi.org/10.1177/0361198119898455.

Schüttrumpf, H. *et al.* (2022) 'Herausforderungen an den Wiederaufbau nach dem Katastrophenhochwasser 2021 in der Eifel', in. *45. Dresdner Wasserbaukolloquium 2022 „Nachhaltigkeit im Wasserbau – Umwelt, Transport, Energie"*, Dresden, Germany: Technische Universität Dresden, Institut für Wasserbau und technische Hydromechanik, pp. 5–16. Available at: https://hdl.handle.net/20.500.11970/108907 (Accessed: 14 February 2023).

Scott, D.M. *et al.* (2006) 'Network Robustness Index: A new method for identifying critical links and evaluating the performance of transportation networks', *Journal of Transport Geography*, 14(3), pp. 215–227. Available at: https://doi.org/10.1016/j.jtrangeo.2005.10.003.

Seeger, M. (2023) 'Agricultural Soil Degradation in Germany', in. Berlin, Heidelberg: Springer Berlin Heidelberg, pp. 1–17. Available at: https://doi.org/10.1007/698_2022_948.

Selby, B. and Kockelman, K.M. (2013) 'Spatial prediction of traffic levels in unmeasured locations: applications of universal kriging and geographically weighted regression', *Journal of Transport Geography*, 29, pp. 24–32. Available at: https://doi.org/10.1016/j.jtrangeo.2012.12.009.

Sfahani, M.G., Guan, H. and Loo, Y.-C. (2015) 'Seismic Reliability and Risk Assessment of Structures Based on Fragility Analysis – A Review', *Advances in Structural Engineering*, 18(10), pp. 1653–1669. Available at: https://doi.org/10.1260/1369-4332.18.10.1653.

Spyrou, C. *et al.* (2020) 'Implementation of a Nowcasting Hydrometeorological System for Studying Flash Flood Events: The Case of Mandra, Greece', *Remote Sensing*, 12(17), p. 2784. Available at: https://doi.org/10.3390/rs12172784.

Steeb, N. *et al.* (2017) 'Large wood recruitment processes and transported volumes in Swiss mountain streams during the extreme flood of August 2005', *Geomorphology*, 279, pp. 112–127. Available at: https://doi.org/10.1016/j.geomorph.2016.10.011.

Stochino, F., Fadda, M.L. and Mistretta, F. (2018a) 'Assessment of RC Bridges integrity by means of low-cost investigations', *Frattura ed Integrità Strutturale*, 12(46), pp. 216–225. Available at: https://doi.org/10.3221/IGF-ESIS.46.20.

Stochino, F., Fadda, M.L. and Mistretta, F. (2018b) 'Low cost condition assessment method for existing RC bridges', *Engineering Failure Analysis*, 86, pp. 56–71. Available at: https://doi.org/10.1016/j.engfailanal.2017.12.021.

Sullivan, J.L. *et al.* (2010) 'Identifying critical road segments and measuring system-wide robustness in transportation networks with isolating links: A link-based capacity-reduction approach', *Transportation Research Part A: Policy and Practice*, 44(5), pp. 323–336. Available at: https://doi.org/10.1016/j.tra.2010.02.003.

Szymczak, S. *et al.* (2022) 'Impacts of Heavy and Persistent Precipitation on Railroad Infrastructure in July 2021: A Case Study from the Ahr Valley, Rhineland-Palatinate, Germany', *Atmosphere*, 13(7), p. 1118. Available at: https://doi.org/10.3390/atmos13071118.

Tanasić, N. and Hajdin, R. (2018) 'Management of bridges with shallow foundations exposed to local scour', *Structure and Infrastructure Engineering*, 14(4), pp. 468–476. Available at: https://doi.org/10.1080/15732479.2017.1406960.

Togia, H. *et al.* (2019) 'Segment-Based Approach for Assessing Hazard Risk of Coastal Highways in Hawai'i', *Transportation Research Record*, 2673(1), pp. 83–91. Available at: https://doi.org/10.1177/0361198118821679.

Transportation Research Board (2010) *Highway Capacity Manual*. Washington, D.C.: Transportation Research Board.

Troin, M. *et al.* (2021) 'Generating Ensemble Streamflow Forecasts: A Review of Methods and Approaches Over the Past 40 Years', *Water Resources Research*, 57(7), p. e2020WR028392. Available at: https://doi.org/10.1029/2020WR028392.

Truedinger, A.J. *et al.* (2023) 'Adaptation after Extreme Flooding Events: Moving or Staying? The Case of the Ahr Valley in Germany', *Sustainability*, 15(2), p. 1407. Available at: https://doi.org/10.3390/su15021407.

Tubaldi, E. *et al.* (2017) 'A framework for probabilistic assessment of clear-water scour around bridge piers', *Structural Safety*, 69, pp. 11–22. Available at: https://doi.org/10.1016/j.strusafe.2017.07.001.

Tubaldi, E. *et al.* (2022) 'Invited perspectives: Challenges and future directions in improving bridge flood resilience', *Natural Hazards and Earth System Sciences*, 22(3), pp. 795–812. Available at: https://doi.org/10.5194/nhess-22-795-2022.

Tubaldi, E., Macorini, L. and Izzuddin, B. (2017) 'Flood Risk Assessment of Masonry Arch Bridges', in *Proceedings of the 2nd International Conference on Uncertainty Quantification in Computational Sciences and Engineering (UNCECOMP 2017)*. *1st International Conference on Uncertainty Quantification in Computational Sciences and Engineering*, Rhodes Island, Greece: Institute of Structural Analysis and Antiseismic Research School of Civil Engineering National Technical University of Athens (NTUA) Greece, pp. 140–153. Available at: https://doi.org/10.7712/120217.5358.16942.

Van Campenhout, J. *et al.* (2020) 'Return Period of Characteristic Discharges from the Comparison between Partial Duration and Annual Series, Application to the Walloon Rivers (Belgium)', *Water*, 12(3), p. 792. Available at: https://doi.org/10.3390/w12030792.

Vorogushyn, S. *et al.* (2022) 'Statistical and hydraulic analysis of flood hazard in the Ahr valley, Germany considering historical floods.', in. *IAHS-AISH Scientific Assembly 2022*, Montpellier, France, pp. IAHS2022-660. Available at: https://doi.org/10.5194/iahs2022-660.

Wang, C., Yu, X. and Liang, F. (2017) 'A review of bridge scour: mechanism, estimation, monitoring and countermeasures', *Natural Hazards*, 87(3), pp. 1881–1906. Available at: https://doi.org/10.1007/s11069-017-2842-2.

Wang, H. *et al.* (2014) 'Forensic Diagnosis on Flood-Induced Bridge Failure. I: Determination of the Possible Causes of Failure', *Journal of Performance of Constructed Facilities*, 28(1), pp. 76–84. Available at: https://doi.org/10.1061/(ASCE)CF.1943-5509.0000419.

Wang, W. *et al.* (2019) 'Local floods induce large-scale abrupt failures of road networks', *Nature Communications*, 10(1), p. 2114. Available at: https://doi.org/10.1038/s41467-019-10063-w.

Wardhana, K. and Hadipriono, F.C. (2003) 'Analysis of Recent Bridge Failures in the United States', *Journal of Performance of Constructed Facilities*, 17(3), pp. 144–150. Available at: https://doi.org/10.1061/(ASCE)0887-3828(2003)17:3(144).

Washington DOT (2020) *Tacoma Narrow Bridge - More Than a Bridge.*, Washington, USA. Available at: https://www.wsdot.wa.gov/TNBhistory/ (Accessed: 26 May 2020).

Wasko, C. *et al.* (2021) 'Evidence of shorter more extreme rainfalls and increased flood variability under climate change', *Journal of Hydrology*, 603, p. 126994. Available at: https://doi.org/10.1016/j.jhydrol.2021.126994.

Webb, B.M. and Cleary, J.C. (2019) 'Drag-Induced Displacement of a Simply Supported Bridge Span during Hurricane Katrina', *Journal of Performance of Constructed Facilities*, 33(4), p. 04019040. Available at: https://doi.org/10.1061/(ASCE)CF.1943-5509.0001305.

Wing, O.E.J. *et al.* (2020) 'New insights into US flood vulnerability revealed from flood insurance big data', *Nature Communications*, 11(1), p. 1444. Available at: https://doi.org/10.1038/s41467-020-15264-2.

Wisetjindawat, W., Derrible, S. and Kermanshah, A. (2018) 'Modeling the Effectiveness of Infrastructure and Travel Demand Management Measures to Improve Traffic Congestion during Typhoons',

Transportation Research Record, 2672(1), pp. 43–53. Available at: https://doi.org/10.1177/0361198118791909.

Wyss, A., Schalko, I. and Weitbrecht, V. (2021) 'Field Study on Wood Accumulation at a Bridge Pier', *Water*, 13(18). Available at: https://doi.org/10.3390/w13182475.

Xie, F. and Levinson, D. (2011) 'Evaluating the effects of the I-35W bridge collapse on road-users in the twin cities metropolitan region', *Transportation Planning and Technology*, 34(7), pp. 691–703. Available at: https://doi.org/10.1080/03081060.2011.602850.

Xiong, W. *et al.* (2023) 'Review of Hydraulic Bridge Failures: Historical Statistic Analysis, Failure Modes, and Prediction Methods', *Journal of Bridge Engineering*, 28(4), p. 03123001. Available at: https://doi.org/10.1061/JBENF2.BEENG-5763.

Xu, X. (Alex) *et al.* (2017) 'Estimating Path Travel Costs for Heterogeneous Users on Large-Scale Networks: Heuristic Approach to Integrated Activity-Based Model–Dynamic Traffic Assignment Models', *Transportation Research Record*, 2667(1), pp. 119–130. Available at: https://doi.org/10.3141/2667-12.

Yang, J., Castelli, F. and Chen, Y. (2014) 'Multiobjective sensitivity analysis and optimization of distributed hydrologic model MOBIDIC', *Hydrology and Earth System Sciences*, 18(10), pp. 4101–4112. Available at: https://doi.org/10.5194/hess-18-4101-2014.

Yilmaz, T., Banerjee, S. and Johnson, P.A. (2016) 'Performance of Two Real-Life California Bridges under Regional Natural Hazards', *Journal of Bridge Engineering*, 21(3), p. 04015063. Available at: https://doi.org/10.1061/(ASCE)BE.1943-5592.0000827.

Yilmaz, T., Banerjee, S. and Johnson, P.A. (2018) 'Uncertainty in risk of highway bridges assessed for integrated seismic and flood hazards', *Structure and Infrastructure Engineering*, 14(9), pp. 1182–1196. Available at: https://doi.org/10.1080/15732479.2017.1402065.

Yoon, H.N., Marshall, L. and Sharma, A. (2023) 'Beyond river discharge gauging: hydrologic predictions using remote sensing alone', *Environmental Research Letters*, 18(3), p. 034015. Available at: https://doi.org/10.1088/1748-9326/acb8cb.

Zhang, G. *et al.* (2022) 'Causes and statistical characteristics of bridge failures: A review', *Journal of Traffic and Transportation Engineering (English Edition)*, 9(3), pp. 388–406. Available at: https://doi.org/10.1016/j.jtte.2021.12.003.

Zhang, N. and Alipour, A. (2020) 'Two-Stage Model for Optimized Mitigation and Recovery of Bridge Network with Final Goal of Resilience', *Transportation Research Record*, 2674(10), pp. 114–123. Available at: https://doi.org/10.1177/0361198120935450.

Zounemat-Kermani, M. *et al.* (2021) 'Ensemble machine learning paradigms in hydrology: A review', *Journal of Hydrology*, 598, p. 126266. Available at: https://doi.org/10.1016/j.jhydrol.2021.126266.